Hovedoppgave

NTNU
Norges teknisk-naturvitenskapelige universitet
Fakultet for ingeniørvitenskap
Institutt for marin teknikk

Torstein Sæter

Ringing Loads on Offshore Wind Turbine Monopiles

Hovedoppgave i MTMART
Veileder: Trygve Kristiansen
Juni 2019

NTNU
Norwegian University of
Science and Technology

Abstract

Kristiansen and Faltinsen (2017) confirmed that the inviscid FNV-theory, compared to experiments, over-estimated the third harmonic wave load amplitudes on a bottom mounted vertical cylinder for longer and steeper waves. The local KC number along the vertical axis of the cylinder, indicated that the flow separates under the wave conditions where discrepancies in the third harmonic loads are present. Hence, the consequence of involving viscous effects in the analyses was investigated in the present work. A combined CFD-FNV load model was derived by replacing the force term proportional to $\frac{\partial u}{\partial t}$ in the FNV-theory, with an integrated CFD-force. However, compared with the inviscid fifth order FNV-theory, the load estimations from the CFD-FNV load model did not comply better with the experimental results. In fact, using the combined load-model, the third harmonic amplitudes were over-estimated slightly more for the steeper waves. Furthermore, several approaches of modelling the boundary layer, and the corresponding effects on the results, were investigated. Although the use of different viscous models affected the vorticity field around the cylinder, the load harmonic amplitudes remained by almost the same magnitudes. Thus, the involvement of 2-D viscous effects in the analysis during the present work, was not able to explain the observed discrepancies in the third harmonic loads.

An experiment was performed, in order to get deeper insight into 3-D effects that potentially could explain the discrepancies between the so-far tested load models and experiments. Several authors have observed and commented on a local rear run-up during experiments of regular waves on a slender bottom mounted vertical cylinder. The run-up is believed to be caused by a high pressure zone due to vortex shedding at the rear of the cylinder. The upwelling of the free surface was also observed during the experiment in the present work. Higher harmonic load contributions from the run-up may explain the discrepancies in the third harmonic loads. A 3-D CFD analysis would be necessary in order to account for this effect.

Preface

I would like to express my greatest gratitude to the people that have helped me with my work related to the Master Thesis, during this final year at NTNU Trondheim. It has been a pleasure to work with my supervisor Trygve Kristiansen, who generously has shared his great knowledge about the relevant topic and marine hydrodynamics in general. I would also thank my co-supervisor Ken-Robert Jakobsen from EDRMedeso, who has been very instructive and helpful regarding the work with the commercial software package ANSYS Fluent. I would also like to express my gratitude for the permission to employ the IDUN-cluster at NTNU Gløshaugen. The thesis could not have been completed the way it was, without the computational resources available. At last, I would like to thank lab-technician Terje Rosten, who helped me with the setup and performance of the model experiment, completed in the beginning of March. The experiment could be carried out very efficiently because of him.

Table of Contents

Summary i

Preface ii

Table of Contents v

List of Tables vii

List of Figures xii

1 Introduction 1

1.1 Motivation 1

1.2 Background and Scope 2

1.3 Report structure 3

2 Theory 5

2.1 Basic equations and assumptions in fluid mechanics 5

2.1.1 Potential theory 5

2.1.2 Conservation of mass 6

2.1.3 Conservation of momentum 7

2.1.4 Boundary layer theory 8

2.2 The boundary value problem 10

2.2.1 Boundary conditions 10

2.2.2 Stokes perturbation approach 11

2.2.3 Linearization 12

2.2.4 Wave theory . . . 13
2.2.5 Stokes fifth order waves . . . 13
2.3 Wave forces on vertical circular cylinders . . . 18
2.3.1 Potential flow . . . 18
2.3.2 Morison equation . . . 20
2.3.3 The generalized FNV-theory . . . 23
2.3.4 Studies of forces on cylinders in oscillating flows . . . 26
2.4 Numerical modelling of turbulent flows and boundary layers . . . 32
2.4.1 Reynolds-Averaged Navier-Stokes equations . . . 32
2.4.2 Turbulence models . . . 33
2.4.3 The Courant number . . . 34
2.4.4 Near-wall treatment . . . 35
2.4.5 Software and hardware . . . 36

3 Experiment **39**
3.1 Experimental setup . . . 40
3.2 Test program . . . 42
3.3 Comments on the experiment . . . 43
3.4 Visual observations . . . 44

4 Numerical Model **45**
4.1 Set up and validation of the two dimensional model . . . 46
4.1.1 Grid structure . . . 46
4.1.2 Boundary conditions . . . 46
4.1.3 Turbulence model . . . 48
4.1.4 Numerical scheme . . . 49
4.2 Convergence studies . . . 50
4.2.1 Grid studies . . . 50
4.2.2 Time step study . . . 52
4.2.3 Domain size study . . . 53
4.3 Validation of the numerical model . . . 55
4.3.1 C_M and C_D as functions of KC . . . 57
4.3.2 Reynolds number dependency of C_A and C_D . . . 59
4.4 CFD-FNV model . . . 61
4.4.1 Discretization of the cylinder . . . 61
4.4.2 Implementation of Stokes fifth order waves . . . 63

4.4.3 The load terms 65

5 Results **67**

5.1 Comparison between CFD-FNV, inviscid FNV and experiments 67

5.2 Effect of viscous model 73

5.2.1 Vorticity field 75

5.2.2 Pressure distribution on the cylinder 76

5.2.3 Comparison of load harmonics 77

6 Conclusion and further work **79**

Bibliography **81**

Appendix **87**

List of Tables

2.1 Definition of the coefficients D_n and E_n 14

3.1 Information of wave kinematics and flow conditions for the three tested wave periods given in model scale, for steepness $H_1/\lambda = 1/20$ and $H_1/\lambda = 1/30$.The values of the Ursell number indicates that applying Stokes fifth order wave theory is valid for all wave conditions. 42

List of Figures

1.1 Cumulative and annual offshore wind installations (Remy and Mbistrova (2018)) 1

2.1 Drag coefficient of rough circular cylinders in steady incident flow for different surface roughness values $\frac{k}{D}$(Achenbach (1971)). 9
2.2 The domain defining the problem for the potential ϕ. Two conditions are needed at the free surface, while both ζ and ϕ are unknown. 10
2.3 Approximate regions for application of analytical wave theories (Hedges (1995)). 17
2.4 Illustration of the defined Cartesian coordinates, the cross section with radius a and angle θ, the load convention and the water depth h. 20
2.5 Classification of dominating wave forces depending on H, λ and D(Faltinsen (1990)). 21
2.6 Experimental results obtained by Sarpkaya (1976b) for the drag and the mass coefficient as function of the KC-number for different Reynolds numbers and β. Note that the dependence of the coefficients on the parameter β diminishes for higher values of β, implying that the coefficients become more independent of Re. 27
2.7 Experimental results of C_A and C_D for smooth and rough cylinders as obtained by Garrison et al. (1977). $KC = 5\pi$, Reynolds number varied along the horizontal axis. 29
2.8 The relation between u^+ and y^+, in the different sub-layers of the boundary layer (ANSYS (2009)). 36

3.1 Bird eye and side view of the experimental setup that was used in the model experiment. The focus was on flow visualization, thus an underwater camera was recording upwards along the rear of the cylinder. 41

3.2 Amplitudes of the three first harmonics; ζ_{a1}, ζ_{a2} and ζ_{a3}, according to Stokes fifth order waves(dashed lines), compared to corresponding amplitudes of extracted wave harmonics from the experiment(markers). ■, $H_1/\lambda = 1/40$; ◆, $H_1/\lambda = 1/30$; ▼, $H_1/\lambda = 1/20$. Wave periods are given in model scale. 43

3.3 The formation of the local rear run-up, visualized in terms of a snapshot from video recorded during experiments. Wave conditions model scale; $T = 2.02s$ and $H_1/\lambda = 1/20$. Incident waves incoming from right towards left. 44

4.1 Left: The division of the computational domain into several subdomains with description of the geometrical lengths where D represents the diameter of the cylinder, and $10 \leq a \leq 30$. Right: Visualization of the mesh with specified boundary conditions. 46

4.2 Left: Contour representation of linear pressure distribution. Right: Line plot representation of linear pressure distribution, plotted along the in-line direction in the middle of the domain. 47

4.3 The drag coefficient, C_D, and the inertia coefficient, C_M, as functions of the KC-number for varying number of elements along the cylinder surface. Simulations performed with 4000 time-steps per flow period, $N_\theta = 240$ and $a = 30D$. 51

4.4 The drag coefficient, C_D, and the inertia coefficient , C_M, as functions of the KC-number for varying number of elements along the cylinder surface. Simulations performed with 4000 time-steps per flow period, and a domain size of $a = 30D$. $Nr = 200$ 52

4.5 The drag coefficient, C_D, and the inertia coefficient , C_M, as functions of the KC-number for varying number of time steps per flow-period. Simulations performed with $N_\theta = 240$, $N_r = 200$ and $a = 30D$. 53

4.6 C_D and C_M as functions of the KC-number for different domain sizes defined by the variable a. Simulations performed with $N_\theta = 240$, $N_r = 200$ and 4000 time-steps per flow period. 54

4.7 The vorticity field around the cylinder using the two respective meshes are illustrated, for $KC = 6$. The $k-\omega$ SST turbulence model is applied. The symmetry of the vortices using Mesh 1 indicates that it is too coarse for the CFD-software to calculate the vortices accurately. 56

4.8 Development of C_D and C_M coefficients as functions of KC, compared to experiments by Sarpkaya (1987) and Bearman et al. (1985). $\beta = 11525$ in the numerical simulations and in the experiments performed by Sarpkaya (1987) .β between 2×10^4 and 5.49×10^4 in the experiments by Bearman et al. (1985). Note that the latter experiment considered waves, and not mono-harmonic flow. ○, Sarpkaya (1987)(mono-harmonic oscillating flow); ◇, Bearman et al. (1985)(waves); ——— , $k-\omega$ SST model; - - - - - , Laminar model; ·-·-·-· , IDDES model. 58

4.9 Results of C_A and C_D from the numerical model, using the $k-\omega$ SST turbulence model, compared to the experimental values obtained by Garrison et al. (1977). Mesh 1 applied for $KC = \pi$, Mesh 2 for the others. 60

4.10 Left: The horizontal force, $\bar{F}_i$, at strip i, is calculated by interpolation between CFD force-outputs at upper and lower cuts of the strip, F_i^{CFD} and F_{i+1}^{CFD}. Boundary conditions u and p evaluated according to Stokes fifth order wave theory at the horizontal cuts. Right: The strips are contracting and expanding according to $\zeta(t)$. Note that in the following, $cuts$ will refer to the lines dividing the cylinder, while $strips$ are referring to the divided elements with thicknesses Δz_i. N is denoting the number of strips. The water depth $h = 0.5625$cm is considered. 61

4.11 Left: The horizontal velocity u calculated according to fifth order stokes theory for $ka = 0.127$. Right: $ka = 0.105$. In both plots, $H/\lambda = 1/20$, N = 19 and time intervals of T/80 is used. 64

4.12 The maximum value of KC_5 during one wave period for each section of the cylinder(horizontal axis), plotted against corresponding vertical position of the sections(vertical axis). In total 20 cuts are applied, including the top and bottom, along the cylinder-axis according to the stretched mesh discretization of the cylinder. Note the significant increase in KC_5 for higher wave periods and steepness. ◆, $H_1/\lambda = 1/40$; ●, $H_1/\lambda = 1/30$; ▲, $H_1/\lambda = 1/25$; ■, $H_1/\lambda = 1/20$. 65

5.1 The three first load harmonics as calculated by the CFD-FNV model, and the measured time-series from the experiment, respectively. Note that the first order harmonics comply the most, while there are visible discrepancies between the third harmonics, both in terms of phase and magnitude. 68

5.2 Non-dimensional amplitudes of the three first load harmonics versus non dimensional wave-number ka. ○, Experiments Kristiansen and Faltinsen (2017); △, Experiments present work; ——— , FNV; - - - - - , CFD-FNV. 70

5.3 Comparison between the three first load harmonics of the inviscid force-term F_1, and the force compute by the CFD-software. - - - - - , F_1; ——— , F^{CFD}. Wave condition: $ka = 0.127$ and $H_1/\lambda = 1/20$. 72

5.4 Non-dimensional amplitudes of the three first load harmonics versus non dimensional wave-number ka. ○, Experiments Kristiansen and Faltinsen (2017); ◆, CFD-FNV($k-\omega$ SST); ■, CFD-FNV(IDDES); ▲, CFD-FNV(laminar); ——— , FNV. 74

5.5 Visualization of the vorticity field around the cylinder at three time instants using the $k-\omega$ SST model(top), the IDDES model(middle), and the laminar model(bottom). The cut at the top of the submerged cylinder is considered. The respective time instants are taken within the seventh oscillation of in total eight oscillations. 75

5.6 Pressure distribution on cylinder at five different time-instans, applying the $k-\omega$SST, IDDES, and laminar model. The top cut of the cylinder is considered, under wave conditions $ka = 0.127$ and wave steepness $H_1/\lambda = 1/20$. The respective time instants are taken within the seventh oscillation of in total eight oscillations. 76

5.7 Comparison between the three first load harmonics of the force as evaluated by the combined CFD-FNV model, using: ——— , $k-\omega$ SST. - - - - - , IDDES; - - - - - , Laminar. 78

Chapter 1

Introduction

1.1 Motivation

As the world's demand for energy increases and the climate changes suddenly are all around us, new solutions and technology are necessary to handle the challenges. Offshore wind energy is a field of significant potential, and has experienced a fast technological development the recent years due to international cooperation between research facilities, universities and companies to make a competitive alternative to fossil fuels. The European marked invests a lot in offshore wind farms (Remy and Mbistrova (2018)), referring to the data from Wind Europe in the figure below, in which the annual installed capacity (MW) follows an exponential development from the beginning in the early 90's to 2017.

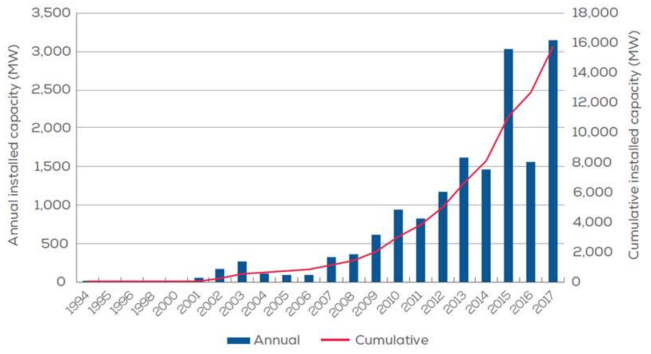

Figure 1.1: Cumulative and annual offshore wind installations (Remy and Mbistrova (2018))

Several challenges still needed to be solved in order to reach a more cost efficient design

of Offshore Wind Turbines (OWT) monopiles. One of the most important ones related to OWTs is associated with the excitation of the natural period, typically laying around 4 seconds. That means 3ω and 4ω components of incoming waves with periods of 12-15 seconds are of main interest with respect to resonance response to higher order wave loads. Estimating these loads also with respect to viscous theory could lead to a more efficient and precise analysis of the forces. Considering an offshore wind park consisting of hundreds of wind turbines, this type of improvement in the design process can potentially reduce the necessary material usage and the costs of development of new OWT fields. This would make bottom-mounted OWTs even more competitive in the European and Global energy market of today and in future.

1.2 Background and Scope

Ringing is defined as transient elastic oscillations in extreme waves, caused by higher harmonic loads exciting resonant response of global structural modes. The investigations so far show that theories based on potential theory, such as the theory by Faltinsen et al. (1995), from now on referred to as the FNV-theory, over-estimate the third harmonic wave forces compared to experiments (Kristiansen and Faltinsen (2017)). The FNV-theory neglects important aspects of the flow such as flow separation. Kristiansen and Faltinsen (2017) addresses the need for deeper investigation of ringing loads on a bottom-mounted surface-piercing slender cylinder by application of Navier-Stoke solvers (computational fluid dynamics; CFD). The present work deals with 2D-CFD simulations. The application of 2D-CFD is based on the assumption that the cross-flow principle is valid, i.e. the gradient of the flow velocity in the vertical direction is negligible compared to the horizontal gradients. The numerical analysis seeks to provide deeper insight in the eventual effect of turbulence in the boundary layer, a topic which today has many uncertainties. Knowledge about the physics related to the transition from laminar to turbulent flows is limited, despite several years with research on the topic. The problem gets even more complex when oscillating flows are studied, e.g. oscillating uniform flow around a cylinder where the flow separates from the body. The flow will here encounter a reversed flow due to the wake of the former flow half-cycle, provoking intense disturbances to the flow. The critical Reynolds numbers, i.e. the Reynolds number of the laminar-turbulence transition, is consequently expected to be considerably lower than for cylinders in uniform steady flow (Bearman et al. (1985), Sarpkaya (1986)). Hence, different approaches to model the boundary layer, with or without turbulence, and its potential impact on the numeri-

cal results were studied. An appropriate model, consisting of a viscous term integrating sectional 2D-CFD forces together, in conjunction with terms from the FNV-theory not accounted for by the CFD-force, was obtained for a wave-cylinder interaction. The capability of the combined CFD-FNV model to estimate the wave-forces on bottom-mounted OWTs was to be evaluated. Especially the accuracy on prediction of the third harmonic loads, which are shown to be over-estimated by pure FNV-theory, was focused on.

1.3 Report structure

The report consists of a few main parts. Firstly, the theory considered most relevant for the present work is introduced, some topics more comprehensively than others. Next, the model experiment that were carried out in the small wave tank at the centre of marine technology, NTNU Trondheim, is described and commented on.

Thereafter, the numerical model that was created in order to simulate the cross section of the monopile model in oscillating flow, is presented. The modelling approach in terms of grid, turbulence, and numerical scheme are explained. In addition are convergence tests that verified the result's independence of the simulation parameters discussed. The numerical model was also compared to related experimental results, in order to validate the model. At last, the derivation of the combined CFD-FNV model is presented.

Subsequently, the results and a comprehensive discussion around them are provided. The main focus was on the comparison between estimations of the third harmonic load by the combined CFD-FNV model with the experimental results by Kristiansen and Faltinsen (2017). Finally, a conclusion summarizing the main findings and proposals for further work are given.

Chapter 2

Theory

2.1 Basic equations and assumptions in fluid mechanics

2.1.1 Potential theory

The assumptions required for a potential flow are:

- Inviscid fluid
- Incompressible fluid
- Irrotational flow

Although the incompressible assumption is rather descriptive considering the properties of water, the assumptions of an irrotational flow and inviscid fluid depend on the situation. Free and external flows around bodies can be considered frictionless and irrotational since the inviscid effects are reserved a very thin layer around the body, called the boundary layer. However, when potential theory applies, a potential scalar function, ϕ, describing the velocity field of the fluid as the gradient of itself, must exist. This can accordingly be proven through a simple derivation. For any scalar ϕ, applies,

$$\nabla \times \nabla \phi = 0 \tag{2.1}$$

The assumption of irrotational flow supplies,

$$\nabla \times \vec{u} = 0 \tag{2.2}$$

Comparing equation (2.28) with (2.2), it follows that,

$$\vec{u} = \nabla\phi \tag{2.3}$$

The potential function describes the velocity field of the flow in the following terms

$$u = \frac{\partial\phi}{\partial x} \quad , \quad v = \frac{\partial\phi}{\partial x} \quad , \quad w = \frac{\partial\phi}{\partial x} \tag{2.4}$$

where u, v and w are the magnitudes of the velocity vector $\vec{u}$ in x, y and z direction, respectively.

2.1.2 Conservation of mass

The integral form of mass conservation can be written

$$\frac{\partial}{\partial t}\int_{\Omega}\rho d\Omega + \int_{S}\rho\vec{u}\cdot\vec{u}dS = 0 \tag{2.5}$$

where Ω is the volume of the domain, while S is the surface. Using the divergence theorem on the second term, a reformulation of the equation into differential coordinate-free form is possible,

$$\frac{\partial\rho}{\partial t} + \nabla\cdot(\rho\vec{u}) = 0 \tag{2.6}$$

The assumption of an incompressible fluid yields,

$$\nabla\cdot(\vec{u}) = 0 \tag{2.7}$$

Or written with index notation and in Cartesian Coordinates,

$$\frac{\partial(\rho u_i)}{\partial x_i} = 0 \tag{2.8}$$

By combining (2.3) and (2.7), a second order partial differential equation, better known as the Laplace equation, can be defined

$$\nabla^2\phi = 0 \tag{2.9}$$

2.1.3 Conservation of momentum

The integral form of the momentum conservation equation can be written as in (2.10),

$$\frac{\partial}{\partial t}\int_{\Omega}\rho\phi d\Omega + \int_{S}\rho\vec{u}\vec{u}\cdot\vec{n}dS = \Sigma\vec{f} \tag{2.10}$$

where Σf is the sum of external forces acting on the fluid in the CV, either in terms of surface forces or in terms of body forces. Only Newtonian fluids are considered, meaning that the stress tensor is linearly proportional to the strain rate tensor. In addition, an incompressible and isothermal fluid is assumed. It may be shown that a derivation based on these assumptions as well as application of the Gauß-theorem yields the incompressible Navier-Stokes equation,

$$\rho\frac{D\vec{u}}{Dt} = -\vec{\nabla}p + \rho\vec{g} + \mu\nabla^2\vec{u} \tag{2.11}$$

where the gravity $\vec{g}$, is the only body force acting on the fluid. Equation (2.11) consists of four unknowns in terms of three velocity components in addition to the pressure. It can be rewritten in terms of index notation and Cartesian coordinates

$$\frac{\partial(\rho u_i)}{\partial t} + \frac{\partial(\rho u_i u_j)}{\partial x_j} = +\rho g_i - \frac{\partial p}{\partial x_i} + \frac{\partial \tau_{ij}}{\partial x_j} \tag{2.12}$$

where τ_{ij} represents the viscous stress tensor components.

$$\tau_{ij} = \mu\Big(\frac{\partial u_i}{\partial x_j} + \frac{\partial u_j}{\partial x_i}\Big) \tag{2.13}$$

Euler equation

A distinct approximation to (2.11) applies when the Reynolds number is high and accordingly $\frac{1}{Re} \approx 0$. The viscous term from the Navier-Stokes equation is hence negligible outside the boundary layer and the remaining terms compose the Euler Equation,

$$\rho\frac{D\vec{u}}{Dt} = -\vec{\nabla} + \rho\vec{g} \tag{2.14}$$

Due to the high velocity gradients normal to the wall because of the frictional force from the no-slip condition, the viscous term is not negligible in the boundary layer. Derived boundary layer approximations, as Prandtl (1904), may be used instead. However, in the region of flow separation, the only equation valid to describe the fluid is the Navier-Stokes equation.

2.1.4 Boundary layer theory

Boundary layer theory is one of the main topic within fluid mechanics, and hence also very important in marine hydrodynamics. In the following, the main focus will be on flow around circular cylinders as this is most representative for the present work.

Flow separation

The tendency of the flow to stick to or separate from the wall depends mainly on the pressure gradient. A favourable pressure gradient($\frac{\partial p}{\partial x} < 0$) and increasing flow velocity are associated with thin boundary layers and wall-attached flows. However, as the pressure gradient increases and the velocity decelerates, the boundary layer grows thicker and the flow becomes more likely to separate. If the adverse pressure is strong enough, the shear stress, which is proportional to $\frac{\partial u}{\partial y}|_{y=0}$, becomes zero, defining the separation point on the cylinder. Downstream the separation point, a reversed flow rises due to the vorticity associated with the separation of the fluid from the wall. For a cylinder in ambient steady laminar flow, the separation point is located around $80 - 85°$(from the stagnation point), while in turbulent flows, it takes place around $110°$ (Chang (1961)).

Classification of flow regimes of uniform flow around fixed cylinder

Laminar flows are characterised by smooth streamlines and high order of motion, while turbulent flows are characterised by velocity fluctuations and high disorder of motion. The flow regime depends highly on the ratio between inertia and viscous forces, defined by the Reynolds number:

$$Re = \frac{U_\infty D}{\nu} \tag{2.15}$$

where U_∞ is the uniform free stream velocity, D is the characteristic length of the body, and ν is the kinematic viscosity. At high Reynolds number, the inertia forces dominates the viscous forces. Consequently, the viscous forces will not prevent the fluids random and rapid fluctuations.
Rough estimations of flow regimes, considering an uniform flow past a smooth cylinder, may be based on the global Reynolds number:

- $Re \lesssim 2 \cdot 10^5$
- $2 \cdot 10^5 \lesssim Re \lesssim 5 \cdot 10^5$

- $5 \cdot 10^5 \lesssim Re \lesssim \cdot 10^6$
- $Re \gtrsim 3 \cdot 10^6$

where the flow regimes from top to bottom are called: subcritical flow regime, critical flow regime, superciritcal flow regime and transcritical flow regime. The Reynolds number characterising the flow regimes are of course approximate values. However, these Reynolds numbers are referring to the global flow regime. In regions where the flow might be affected by the body surface, the local flow regime will develop differently. Generally, in the subcritical regime, the boundary layer is always laminar before the separation point, while for the super- and transcritical flow regimes, it will be turbulent before separation. In the critical regime, there will be a delayed separation due to reattachemnt of the flow more downstream of the cylinder. This is clearly visible as a sudden drop in the value of the drag coefficient in the critical range of Reynolds number, illustrated in the plot of the drag coefficient as a function of the Reynolds number for cylinders with different surface roughness k(see Figure 2.1). The critical range and hence the "drop" depends here on the surface roughness of the cylinder.

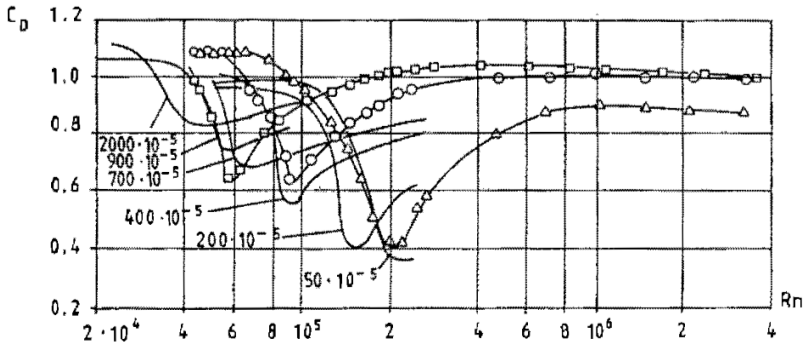

Figure 2.1: Drag coefficient of rough circular cylinders in steady incident flow for different surface roughness values $\frac{k}{D}$(Achenbach (1971)).

2.2 The boundary value problem

The typical problem in marine hydrodynamics is defined by a set of conditions needed to be fulfilled on the considered domain of the fluid. Usually in marine hydrodynamics this domain also involves a marine structure, whose excitation loads and corresponding response are in main focus to analyse. The other boundaries except of the body present, are usually defined as the free surface, the seabed, and the inlet and outlet of the domain. Mathematical conditions in correspondence with the physics of the situation must be introduced in order to obtain a unique solution for the problem. The validity and accuracy of the solution are dependent on the selection of boundary conditions, chosen based on the intuitive understanding of the problem.

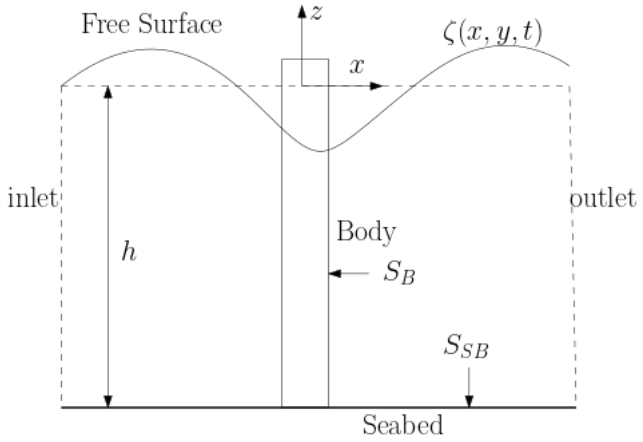

Figure 2.2: The domain defining the problem for the potential ϕ. Two conditions are needed at the free surface, while both ζ and ϕ are unknown.

2.2.1 Boundary conditions

The domain illustrated in Figure 2.2 is considered in the following. By considering potential theory and the conservation of mass, the Laplace equation (2.9) is the governing equation applying over the whole domain of the fluid. The boundary conditions applying on the free surface are the kinematic and dynamics free surface condition. The kinematic free surface condition is the criterion for the fluid particles on the free surface to remain on the free surface, while the dynamic free surface conditions originates from the Bernoulli equation and maintenance of uniform pressure on the free surface. These conditions are formally written

$$\frac{\partial \zeta}{\partial t} = \frac{\partial \phi}{\partial z} - \Delta\phi \cdot \Delta\zeta \quad , \quad z = \zeta(x, y, t) \tag{2.16}$$

$$\frac{\partial \phi}{\partial t} = \Delta\phi \cdot \Delta\phi + g\zeta \quad , \quad z = \zeta(x, y, t) \tag{2.17}$$

where (2.16) refers to the kinematic free surface conditions, and (2.17) to the dynamic ones. The bottom boundary condition on the seabed is formulated as,

$$\vec{u} \cdot \vec{n} = 0 \quad on\ S_{SB} \tag{2.18}$$

where $\vec{n}$ is the normal vector of the seabed. This condition applies as the flow neither is allowed to flow across, nor have any horizontal velocity at the fixed bottom(usually referred to as the no-slip condition in fluid mechanics). Similarly the impermeability conditions on the surface of the body can be written

$$\vec{u} \cdot \vec{n} = 0 \quad on\ S_B \tag{2.19}$$

where S_B is the surface of the submerged body, and $\vec{n}$ is the normal vector on the body. At the inlet and outlet of the domain, the boundary conditions are dependent on the problem description. In a classical problem involving a wave-generating wavemaker, boundary conditions representing the kinematics of the waves must also be stated at the lateral sides of the domain.

2.2.2 Stokes perturbation approach

By assuming that the solution will depend on a small parameter ϵ, being of the same order as the non-dimensional wave steepness $k\zeta$, the velocity potential ϕ and free surface elevation ζ can be expressed as power expansions where the terms are arranged according to the order of ϵ. The linear solution is independent of ϵ, while the second order term will be proportional to ϵ, and so on.

$$\phi = \epsilon\widetilde{\phi_1} + \epsilon^2\widetilde{\phi_2} + \epsilon^3\widetilde{\phi_3} + ... \tag{2.20}$$

$$\zeta = \epsilon\widetilde{\zeta_1} + \epsilon^2\widetilde{\zeta_2} + \epsilon^3\widetilde{\zeta_3} + ... \tag{2.21}$$

Using the Stokes perturbation approach, the non-linear boundary value problem can be rewritten into an infinite number of linear equations, in ascending order of ϵ.

2.2.3 Linearization

Both of the free surface conditions are non-linear. However, by application of the perturbation approach, only keeping terms up to the first order, and Taylor expansion of both conditions around the mean free surface at $z = 0$, linearized versions of the conditions are obtained. The linearized expressions become as follows,

$$\frac{\partial \zeta}{\partial t} = \frac{\partial \phi}{\partial z} \quad , \quad z = 0 \tag{2.22}$$

$$g\zeta + \frac{\partial \phi}{\partial t} = 0 \quad , \quad z = 0 \tag{2.23}$$

Taking the time derivative of (2.23) and inserting for $\frac{\partial \zeta}{\partial t}$ into (2.22), a combined linearized free surface condition is derived,

$$\frac{\partial^2 \phi}{\partial t^2} + g\frac{\partial \phi}{\partial z} = 0 \tag{2.24}$$

The linearization of the physical problem narrows down the scope to only consider the forces in range of the excitation frequency, exciting motion of the structure proportional to the incoming excitation forces. The solutions for the velocity potential and pressure are accordingly carried out to first order of the non dimensional wave slope $k\zeta_a$. Although a linearization is a great simplification of the problem, it can in cases with large volume-structures, such as semi-submersibles and ships, describe the wave induced motion and loads sufficiently. Other kinds of structures, such as a bottom-mounted slender vertical cylinder, requires the involvement of non-linear theory for accurate analyses, due to another wave-structure interaction.

2.2.4 Wave theory

Solving the linear boundary value problem yields the first order dispersion relation and a solution for small-amplitude waves. Thus, linear wave theory, or Airy waves, are insufficient to describe waves with larger amplitudes. Hence, deriving wave theories also applying for waves of higher steepness, have been of interest. Examples of such theories are higher order Stoke waves or cnoidal wave theory. Here, Stokes fifth order waves are focused.

2.2.5 Stokes fifth order waves

In order to also include higher order terms, the power expansion of the potential ϕ and the wave elevation ζ must be completed to a higher order. Stokes presented a solution for waves of finite height by use of trigonometric series. However, deriving the coefficients for higher order waves with this method is rather time consuming and monotonous. Therefore, Skjelbreia and Hendrickson (1960) aimed to provide tabular values of the coefficients of Stoke fifth order wave theory as a function of the parameter h/λ, which derivation in the following is quickly reviewed. To be consistent, the definition of the coordinate system and axis differs here from the original paper, but are defined according to Figure 2.2. In addition, because an oscillatory wave of wavelength λ is considered, the constant denoted λ in Skjelbreia and Hendrickson (1960) is here referred to as Π.

The waves are being assumed to be non-viscous long crested water waves of constant depth. The horizontal velocities may therefore easily be obtained according to potential theory when the velocity potential ϕ is known. The kinematic and dynamic free surface conditions need to be fulfilled at the free surface, while the bottom boundary condition applies at the seabed. The wave profile and potential function can be expressed as functions of a phase angle θ,

$$\theta = \frac{2\pi}{\lambda}(x - c_\omega t) = k(x - \bar{c_\omega} t) \tag{2.25}$$

where c_ω is the wave celerity. Using the relation between the velocities and the potential(((2.4)), combined with the free surface conditions((2.16), (2.17)) and (2.25), the kinematic and dynamic free surface conditions may be rewritten into

$$\frac{\partial w}{\partial x} = \frac{-w}{c_\omega - u} \tag{2.26}$$

$$(c_\omega - u)^2 + w^2 = c_\omega^2 - 2g(K + \zeta) \tag{2.27}$$

where K is a constant. The potential ϕ needs to satisfy the Laplace equation, the free surface boundary conditions, as well as the bottom boundary condition. The solution for the wave profile ζ will appear in the iterative solution process of (2.26) and (2.27). The expressions for both ϕ and ζ are assumed to form trigonometric series. The unknown constants are determined using an iterative procedure by substitution into equation (2.26) and (2.27). The series will here be expressed in the same compact manner as by Fimland (2018).

$$\phi = \frac{c_\omega}{k} \sum_{n=1}^{5} D_n \cosh(nk(h+z)\ \sin(n\theta) \tag{2.28}$$

$$\zeta = \frac{1}{k} \sum_{n=1}^{5} E_n \cosh(n\theta) \tag{2.29}$$

where the wave celerity is expressed accordingly,

$$c_\omega = \frac{\sqrt{C_0^2(1 + \Pi^2 C_1 + \Pi^4 C_2)}}{k} \tag{2.30}$$

The expressions represented by the introduced coefficients D_n and E_n can be found in table 2.1,

n	D_n	E_n
1	$\Pi A_{11} + \Pi^3 A_{13} + \Pi^5 A_{15}$	Π
2	$\Pi^2 A_{22} + \Pi^4 A_{24}$	$\Pi^2 B_{22} + \Pi^2 B_{24}$
3	$\Pi^3 A_{33} + \Pi^5 A_{35}$	$\Pi^3 B_{33} + \Pi^5 B_{35}$
4	$\Pi^4 A_{44}$	$\Pi^4 B_{44}$
5	$\Pi^5 A_{55}$	$\Pi^5 B_{55}$

Table 2.1: Definition of the coefficients D_n and E_n

In addition, the forms of the constant K and wave celerity c_ω are assumed as follows

$$kK = \Pi^2 C_3 + \Pi^4 C_4 \tag{2.31}$$

$$kC_\omega^2 = C_0^2(1 + \Pi^2 C_1 + \Pi^4 C_2) \tag{2.32}$$

The expressions for ϕ, ζ, K and k, are substituted into the rewritten free surface conditions((2.26) and (2.27)). The terms are thereafter grouped by powers of λ and sub-grouped by powers of $\cos(\theta)$. Because the equation must apply for every ϕ, terms of the same power of λ and $\cos(\theta)$ are set equal to each other, yielding an equation set of twenty equations with twenty unknown coefficients; A_{ij}, B_{ij} and C_i. The coefficients are provided in tabular form by Skjelbreia and Hendrickson (1960) as functions of h/λ. However, as Fenton (1985) identified, the sign in front of 2592 in the expression for C_2 should be a minus.

By using the relation between the surface elevation and the wave height H, $H = \zeta|_{\theta=0} - \zeta|_{\theta=\pi}$, (2.29) may be reformulated into

$$\frac{\pi H}{h} = \frac{\lambda}{h}(\Pi + \Pi^3 B_{33} + \Pi^5(B_{35} + B_{55})) \tag{2.33}$$

Additionally, using the expression for C_0 as derived by Skjelbreia and Hendrickson (1960) together with equation 2.27, the following relation is derived

$$\frac{h}{\lambda_0} = \frac{h}{\lambda}\tanh kh(1 + \Pi^2 C_1 + \Pi^4 C_2) \tag{2.34}$$

where $\lambda_0 = \frac{gT^2}{2\pi}$. Because the wave heights and wave length are assumed known characteristics of the wave, and the coefficients only depend on the wave depth to wavelength ratio(h/λ), iterative solving of the nonlinear equations (2.33) and (2.34) provides the values of the wave length λ, and the coefficient Π. The wave number can then easily be found, and accordingly the fifth order expressions for ϕ and ζ are obtained. Furthermore, the velocities u and w are calculated by differentiation of the velocity potential, yielding

$$u = c_\omega \sum_{n=1}^{5} nD_n cosh(nk(h+z))cos(n(\theta)) \tag{2.35}$$

$$w = c_\omega \sum_{n=1}^{5} nD_n sinh(nk(h+z))sin(n(\theta)) \tag{2.36}$$

The acceleration in x-direction may be obtained by differentiating u with respect to time. The velocity gradients are on the other hand found by differentiation of u and w with respect to x and z, respectively,

$$\frac{\partial u}{\partial t} = c_\omega \omega \sum_{n=1}^{5} n^2 D_n cosh(nk(h+z)) sin(n(\theta)) \tag{2.37}$$

$$\frac{\partial u}{\partial x} = -c_\omega k \sum_{n=1}^{5} n^2 D_n cosh(nk(h+z)) sin(n(\theta)) \tag{2.38}$$

$$\frac{\partial w}{\partial z} = c_\omega k \sum_{n=1}^{5} n^2 D_n cosh(nk(h+z)) sin(n(\theta)) \tag{2.39}$$

The Ursell number

The impact of the Ursell number on the validity of Stokes wave theory has been discussed by several authors e.g. Fenton (1990) and Dean and Dalrymple (1991). The Stokes wave theory has limitations for higher waves in shallow water, especially when only expanded to second order, due to a disproportionately large second order term. Higher order Stokes wave theory should therefore only be used within certain limits of the Ursell number, a number defined according to Ursell (1953),

$$Ur = \frac{H\lambda^2}{h^3} \tag{2.40}$$

Hedges (1995) proposed an upper limit for appropriate use of Stokes wave theory, at $Ur = 40$, where cnoidal wave theory is suggested for higher Ursell numbers (Fenton (1990)). This boundary between the application of Stokes and cnoidal wave theory was found satisfactory, as the wave theories provided results within 5% error compared to the more accurate Fourier values (Hedges (1995)). The approximated regions of valid application of different wave theories can be found in Figure 2.3.

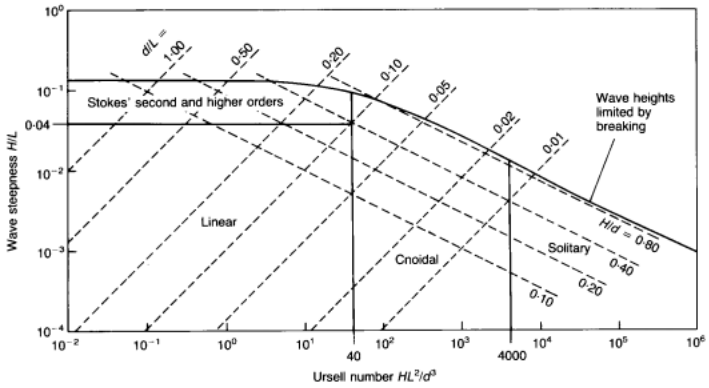

Figure 2.3: Approximate regions for application of analytical wave theories (Hedges (1995)).

2.3 Wave forces on vertical circular cylinders

Potential theory based load-models may in many cases be reliable, but the appropriateness of its application is highly dependent on the problem and wave-structure interaction. Several theories have been derived in order to enable accurate analysis of wave forces on vertical slender cylinder by potential theory, usually including important non-linear forcing terms by introduction of higher order wave kinematics and velocity potentials. Malenica and Molin (1995) are among those who have been focusing on the evaluation of the third harmonic loads on a circular cylinder. However, their and other conventional diffraction theories are based on the assumption that the wave amplitude ζ_a is small compared to the characteristic length of the structure. Faltinsen et al. (1995) allowed incoming waves of higher steepness, with amplitudes of the same order as the radius of the cylinder. With application of potential theory, it is assumed that the inertia loads dominate and the viscous effects are negligible. In the case of a slender circular cylinder, the validity of this assumption is dependent on the considered incoming waves. Longer and steeper waves may lead to local KC-numbers along the vertical cylinder axis indicating viscous effects. The most important load models for the present work are thus presented in a short manner, from the potential theory based FNV-theory to the equation presented by Morison (1950) which also includes a drag-term.

2.3.1 Potential flow

The horizontal forces in surge on a 2D cylinder in an uniform flow can according to potential theory be calculated as

$$F_x = F_I = \rho \frac{\pi D^2}{4} C_M \frac{\partial u}{\partial t} \tag{2.41}$$

where C_M is the inertia coefficient for a circular cylinder. In potential theory, $C_M = 1 + C_A = 2$. Here, C_A is the added mass coefficient for a circular cylinder. The potential value of the added mass for a circular cylinder in surge may very easily be derived by considering a two-dimensional circular cylinder, moving in x-direction with speed $u(t)$ in an infinite fluid where no inflow is considered. The axis system and load conventions are defined according to Figure 2.4. The added mass and damping forces are connected to the dynamic pressure due to motion of the body; they are so-called radiation forces.

$$F_x^{(2D)} = -a_{11}^{(2D)}\ \dot{u} - b_{11}^{(2D)}\ u \tag{2.42}$$

where a_{11} is the added mass in surge, b_{11} is the damping in surge and $F_x^{(2D)}$ is the two dimensional radiation force in surge.

The dynamic pressure can be defined and evaluated at the body surface, where r equals the outer radius a.

$$p = -\rho \frac{\partial \phi}{\partial t} \tag{2.43}$$

$$p|_{r=a} = -\rho \frac{\partial \phi}{\partial t}|_{r=a} \tag{2.44}$$

An infinite segment of the body surface per unit length, may be expressed as,

$$dS = a\ d\theta \tag{2.45}$$

The two-dimensional radiation forces in surge due to the body motion may be found by multiplying the dynamic pressure with the normal vector in surge, n_1, and integrate over dS.

$$F_x^{(2D)} = \int_{\theta=0}^{\theta=2\pi} \rho \frac{\partial \phi}{\partial t}|_{r=a}\ a\ n_1 d\theta \tag{2.46}$$

where normal vector $\vec{n}$ is defined pointing into the water, giving a surge component n_1,

$$n_1 = \cos\theta \tag{2.47}$$

The solution of the velocity potential around a cylinder is given in (2.48), and its time derivative in equation (2.49). These are needed in order to insert for the dynamic pressure into (2.46), yielding (2.50),

$$\phi = u \frac{a^2}{r} \cos\theta \tag{2.48}$$

$$\frac{\partial \phi}{\partial t}|_{r=a} = -\dot{u} a \cos\theta \tag{2.49}$$

$$F_x^{(2D)} = \int_0^{2\pi} -\rho \dot{u} a^2\ \cos^2\theta\ d\theta = -\rho a^2 \pi\ \dot{u} \tag{2.50}$$

Compared with the radiation force in surge (2.42), consisting of one added mass term in phase with acceleration $\dot{u}$, and a damping term in phase with velocity, u, it is clear that the

derived expression from (2.50) must be the added mass term. Accordingly this means that

$$a_{11}^{(2D)} = \rho a^2 \pi = \rho \frac{\pi D^2}{4} \tag{2.51}$$

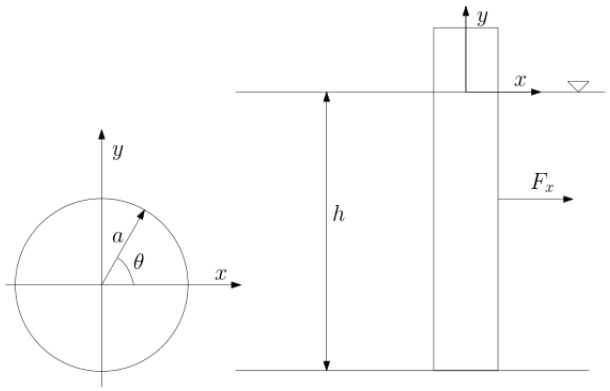

Figure 2.4: Illustration of the defined Cartesian coordinates, the cross section with radius a and angle θ, the load convention and the water depth h.

2.3.2 Morison equation

Commonly, the horizontal force on a strip of a vertical cylinder fixed in the seabed is described trough a division of the total in-line force in two components, where the first term F_I originates from inertia forces, while the second term F_D is a result of the drag forces on the structure.

$$dF = F_I + F_D \tag{2.52}$$

The inertia term is proportional to the acceleration of the fluid, while the drag term is non-linear. This leads to the most common version of Morison equation (2.53), describing the in-line forces onto a vertical strip of a fixed cylinder as follows,

$$dF = \rho \, \frac{\pi D^2}{4} \, C_M \, \dot{u} \, dz + \frac{\rho}{2} C_D D \mid u \mid u \, dz \tag{2.53}$$

where C_M is the inertia coefficient, and C_D is the drag coefficient. In case of potential theory, (2.53) can be rewritten including the added mass from equation (2.51),

$$dF = (\rho \, \frac{\pi D^2}{4} + a_{11}) \, \dot{u} \, dz + \frac{\rho}{2} C_D D \mid u \mid u \, dz \tag{2.54}$$

The Morison equation neglects transverse forces, and is only valid when the long wave

approximation applies, that means when mass or viscous forces are dominating. The long wave approximation requires:

$$\frac{\lambda}{D} > 5 \tag{2.55}$$

where λ is the wavelength and D is the diameter of the cylinder.

Figure 2.5 illustrates the field of application of Morison equation for regular waves on finite water depth. Generally, the Morison equation is not applicable above the wave breaking limit, or when diffraction forces dominate.

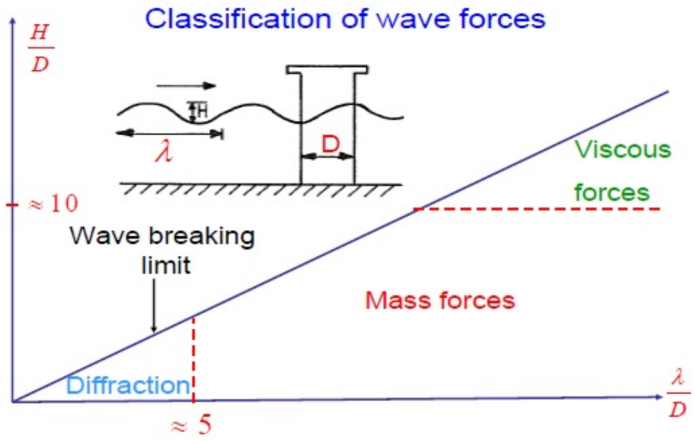

Figure 2.5: Classification of dominating wave forces depending on H, λ and D(Faltinsen (1990)).

Calculation of C_M and C_D

An oscillating flow is described by $u = u_m \cos(\omega t)$, where u_m is the velocity amplitude of the oscillating flow, and ω is the oscillation frequency of the periodic flow. Keulegan and Carpenter (1958) introduced a periodic parameter referred to as the Keulegan-Carpenter(KC)-number,

$$KC = \frac{u_m\, T}{D} \tag{2.56}$$

where T is the oscillation period, and D is the characteristic length of the structure. The Fourier averages of the inertia and drag coefficient can be determined as demonstrated by Keulegan and Carpenter (1958). The force on the cylinder per unit length in general can be written as a function of several parameters,

$$\frac{F}{\rho u_m^2 D} = f(\theta, KC, Re) \tag{2.57}$$

where $\theta = 2\pi t/T$. A Fourier analysis is carried out in order to obtain the values of the values for the coefficients C_M and C_D. As the coefficients vary with the phase θ of the wave cycle, these can be calculated as weighted averages, yielding

$$C_M = \frac{2}{\pi^3}\, KC \int_0^{2\pi} \frac{F \sin\theta}{\rho u_m^2 D} d\theta \tag{2.58}$$

$$C_D = -\frac{3}{4} \int_0^{2\pi} \frac{F \cos\theta}{\rho u_m^2 D} d\theta \tag{2.59}$$

Applying a least square approach to minimize the error between the measured and calculated forces leads to

$$C_{DLS} = -\frac{8}{3\pi} \int_0^{2\pi} \frac{F|\cos\theta|\cos\theta}{\rho u_m^2 D} d\theta \tag{2.60}$$

$$C_{MLS} = C_M \tag{2.61}$$

In this Fourier analysis, the force is assumed periodic and symmetric, i.e. $F(\theta) = -F(\theta + \pi)$. This assumptions is not perfectly accurate, considering that a harmonic oscillating flow around a symmetrically situated cylinder may cause asymmetrical flow and single vortex formations, leading to an asymmetric time series of the force. However, the error is assumed to be small.

Regarding oscillating flows, the importance of the inertia forces compared to drag forces depends highly on KC-number. The ratio between the amplitudes of the inertia and drag terms yields:

$$\frac{F_{I_{max}}}{F_{D_{max}}} = \frac{\frac{\pi^2}{2} C_M D^2 u_0}{\frac{1}{2} C_D D u_0 T} = \frac{\pi^2}{KC} \frac{C_M}{C_D} \tag{2.62}$$

Considering small KC-numbers, $C_M \approx 2$ and $C_D \approx 1$. Accordingly the in-line force on the structure is highly inertia dominated, and the drag contribution may hence be neglected.

2.3.3 The generalized FNV-theory

Faltinsen et al. (1995) derived the FNV theory for infinite water depths and regular incident third order Stokes waves. Regular incident waves of amplitude ζ_a and wave number k is considered incoming to a circular cylinder of radius a. The theory is based upon potential theory and neglects flow separation. Additionally, it is assumed no far field wave generation from the cylinder. In opposite to the conventional perturbation approach, the FNV-theory assumes both the linear wave slope $k\zeta$ and non dimensional cylinder radius ka to be of the same order ϵ. It also includes the higher order effects in the region close to the cylinder associated with the free surface boundary condition. Kristiansen and Faltinsen (2017) generalised the theory to also account for arbitrary incident wave kinematics and finite water depth.

The FNV-theory divides the total potential ϕ into three components; the incident wave potential ϕ_I, the linear diffraction potential ϕ_s and the third order diffraction potential ψ. The latter one satisfies the tree dimensional Laplace equation and approximates free surface conditions to third order. ϕ_s accounts for the impermeability condition on the surface of the cylinder, but not for the disturbances of the free surface. Faltinsen et al. (1995) divides the problem into a linear and a nonlinear analysis. The domain is divided into two sub-domains, where the inner one applies in an order $r/a = \mathcal{O}(1)$ from the cylinder, while the outermost region to an order of $kr = \mathcal{O}(1)$. The nonlinear loads are due to nonlinear effects from the linear solution, but also from the nonlinear potentials forced from the inhomogenous boundary conditions on the free surface. The boundary condition cannot be expanded about the mean free surface level as in a regular perturbation approach, but needs to be imposed on a horizontal plane moving up and down with the incident wave elevation at the cylinder. However, the restriction of the inhomogenoues boundary condition to the inner domain, simplifies the solution of the nonlinear problem.

A solution for the linear diffraction potential, $\phi_D = \phi_I + \phi_s$ must be found. Because the horizontal derivatives have a much higher magnitude than the vertical derivatives, ϕ_D only needs to satisfy the two-dimensional Laplace equation in the horizontal plane. Faltinsen (1999) demonstrated how the scattering potential ϕ_s may be found by slender body theory and matched asymptotic expansion. Starting by Taylor expanding ϕ_D to first order in the wave propagation direction x, around the cylinder axis at $x = 0, y = 0$, yields

$$\phi_D = \phi_I + \phi_{Ix}(x+\phi_{11})\Big|_{x=0,y=0} + \phi_{Ixx}\big(\frac{1}{2}x^2+\phi_{21}\big)\Big|_{x=0,y=0} + f(z,t)+\mathcal{O}(\epsilon^4) \quad (2.63)$$

$$\phi_D = \phi_I + u\,(x+\phi_{11})\Big|_{x=0,y=0} + u_x\,\big(\frac{1}{2}x^2+\phi_{21}\big)\Big|_{x=0,y=0} + f(z,t)+\mathcal{O}(\epsilon^4) \quad (2.64)$$

where $\phi_{11} = \mathcal{O}(\epsilon)$, $\phi_{21} = \mathcal{O}(\epsilon^2)$ and, $f(z,t) = \mathcal{O}(\epsilon^3)$. Faltinsen (1999) showed that the hydrodynamic interaction potential $f(z,t)$ does not contribute to any horizontal force of order lower than $\mathcal{O}(\epsilon^6)$. The scattering potentials ϕ_{11} and ϕ_{21} are found by using the impermeability boundary condition of the surface on the cylinder,

$$\frac{\partial(x+\phi_{11})}{\partial r}\Big|_{r=a} = \frac{\partial(\frac{1}{2}x^2+\phi_{12})}{\partial r}\Big|_{r=a} = 0 \quad (2.65)$$

However, the solution for the linear diffraction potential ϕ_s does not satisfy the inhomogenous free surface boundary conditions, and the third order scattering potential ψ is thus needed in the nonlinear analysis. The vertical derivative of ψ is of the same magnitude as for the horizontal ones, and the potential must accordingly satisfy the 3-D Laplace equation, in addition to the inhomogeous free surface boundary condition. The latter one is expressed as

$$\psi_{tt} + g\psi_z = -2\Delta\phi\cdot\Delta\phi_t - \frac{1}{2}\Delta\phi\cdot\Delta(\Delta\phi)^2 \quad \text{on} \quad z=\zeta \quad (2.66)$$

Because ψ varies strongly in the vertical direction, the formulation of the free surface condition should be based on an expansion around the linear incident free surface elevation and not around the mean surface level $z=0$. ψ_{tt} can be neglected while it is much smaller than the second term on the left hand side of the equation. Consequently the free surface condition becomes

$$g\frac{\partial\psi}{\partial z} = -2uu_t\left(2\frac{\partial\phi_{11}}{\partial x}+(\Delta\phi_{11})^2\right) - \frac{1}{3}u^3\left(2\frac{\partial^2\phi_{11}}{\partial x^2}+2\frac{\partial}{\partial x}(\Delta\phi_{11})^2+\Delta\phi 11\cdot\Delta(\Delta\phi_{11}^2\right) \quad (2.67)$$

being imposed on the linear free surface elevation, $z=\zeta_I$. The force due to the linear diffraction potential ϕ_D, can be found by integrating the pressure along the cylinder wall,

$$F'(z,t) = -\int_0^{2\pi} p\ \cos\theta\ d\theta \tag{2.68}$$

where the normal vector is defined according to equation (2.47). The pressure is evaluated using the Bernoulli equation,

$$\frac{1}{\rho}p = -\frac{\partial\phi_D}{\partial t} - \frac{1}{2}\left(\frac{\partial\phi_D}{\partial r}\right)^2 - \frac{1}{2a^2}\left(\frac{\partial\phi_D}{\partial\theta}\right)^2 - \frac{1}{2}\left(\frac{\partial\phi_D}{\partial z}\right)^2 \tag{2.69}$$

Subsequently, $F'(z,t)$ can be obtained as

$$F'(z,t) = \rho\pi^2 a^2\left(\frac{\partial u}{\partial t} + u\frac{\partial u}{\partial x} + w\frac{\partial u}{\partial z}\right) + a_{11}\left(\frac{\partial u}{\partial t} + w\frac{\partial u}{\partial z}\right) \quad \text{for} \quad -h \le z \le \zeta_I \tag{2.70}$$

Faltinsen et al. (1995) derived the horizontal force F^ψ as a result of the nonlinear scattering potential ψ. The solution is identical in finite water depth.

$$F^\psi = \rho\pi a^2 \frac{4}{g} u^2 \frac{\partial u}{\partial t} \tag{2.71}$$

The distributed hydrodynamic force F' is integrated up to the incident free surface. The FNV theory by Faltinsen et al. (1995), considered three intervals separately; $-\infty \le z \le 0$, $0 \le z \le \zeta_{I1}$ and $\zeta_{I1} \le z \le \zeta$. ζ is defined as $\zeta_{I1} + \zeta_{I2}$, and is the local wave elevation correct to third order. It includes both the effect of the incident waves and the local diffraction of the free surface due to ϕ_D. Kristiansen and Faltinsen (2017) applied the same concept in the generalization of the method to finite water depth. The only difference was the substitution of the infinite water depth to a limit defined by the seabed where $z = -h$. This resulted in the following expressions for the total horizontal force F_x on the cylinder,

$$F_x = \int_{-h}^{\zeta_I} F'(z,t)dz + F^\psi \tag{2.72}$$

$$F_x = \int_{-h}^{0} F'(z,t)dz + \int_0^{\zeta_1} F'(z,t)dz + \int_{\zeta_1}^{\zeta} F'(z,t)dz + F^\psi \tag{2.73}$$

2.3.4 Studies of forces on cylinders in oscillating flows

Separation of flow around bluff bodies is associated with intricate physics in fluid mechanics, and different studies have been performed in order to get deeper insight into the problem. Both harmonic flows and wave forces on cylinders have been investigated through different experimental approaches. The experimental and numerical work found most relevant for the present work are in the following briefly presented and discussed. Certain experiments will later be used in order to validate the numerical model.

Harmonic flows around two-dimensional cylinders

Several authors have worked with great effort to achieve further insight of the transverse and in-line forces on a cylinder in an oscillating flow. Sarpkaya investigated the inertia and drag coefficient's dependency on Re and KC, and performed studies of the boundary layers and the separation points in oscillating flow. The experiments were carried out in terms of several research tests in an U-shaped oscillating flow tunnel. The determination of the mass and force coefficients on the cylinder was found by application of Fourier analysis. Sarpkaya (1976a) and Sarpkaya (1976b) investigated closely the in-line and transverse forces on the cylinder for several different values of the Reynolds and Keulegan-Carpenter number and varying surface roughness. A dependency of the drag and inertia coefficients on an introduced frequency parameter $\beta(\beta = \frac{Re}{KC})$ was discovered. Figure 2.6 show the obtained results of C_M and C_D for varying KC, and the dependency on Re or β. As seen, the minimum value of the drag coefficient decreases as β increases. Increasing β for a given KC yields higher Re, and consequently other properties of the flow(carefully discussed in Sarpkaya (1986)).

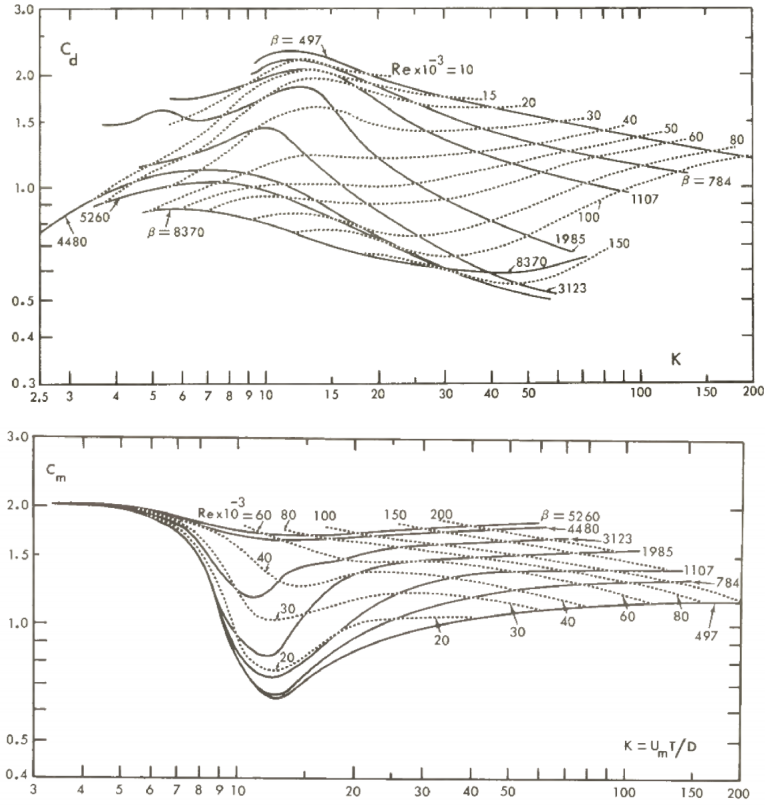

Figure 2.6: Experimental results obtained by Sarpkaya (1976b) for the drag and the mass coefficient as function of the KC-number for different Reynolds numbers and β. Note that the dependence of the coefficients on the parameter β diminishes for higher values of β, implying that the coefficients become more independent of Re.

Sarpkaya (1986) studied the force coefficients C_M and C_D for different values of β in relation with estimates of the critical and separating KC-numbers(KC_{cr} and KC_s). The values of KC_{cr} and KC_s were approximated visually. As an outcome, the development of C_D was categorized into four groups based on KC:

- $KC < KC_{cr}$, the flow is attached, laminar and stable, and the theory presented by Wang (1968) applies.
- The boundary layer turns unstable and turbulent. KC lays between KC_{cr} and KC_{min}. KC_{min} denotes the value of KC corresponding to the minimum value of C_D.
- Effects of flow separation and vortex shedding leads to an increasing drag coefficient. KC is inside the interval $KC_{min} < KC < KC^*$. KC^* represents the limit of the KC-number which after C_D eventual flattens out or even decreasing.

C_M is initially assigned with a value close to potential theory($C_M \simeq 2$), However, it eventually decreases as it is influenced by the occasion of flow separation.

Garrison et al. (1977) also performed several experiments, using the kinematic equivalency between an harmonic oscillating flow around a fixed cylinder, and an harmonic oscillating cylinder in a still fluid. The only difference is that in the latter case, the far field pressure p_∞ leads to the fluid acceleration $\frac{\partial u}{\partial t}$ and so an unit contribution to the added mass coefficient. The advantages and disadvantages of the respective experimental setups have been carefully discussed in several papers, e.g. in Garrison (1980) and Sarpkaya and Isaacson (1981). Figure 4.9 shows the experimental results by Garrison et al. (1977) of the drag and inertia coefficients for a fixed displacement ratio $2a/d = 5$, with varying Reynolds number. The displacement ratio $2a/d = KC/\pi$ is here used rather than KC.

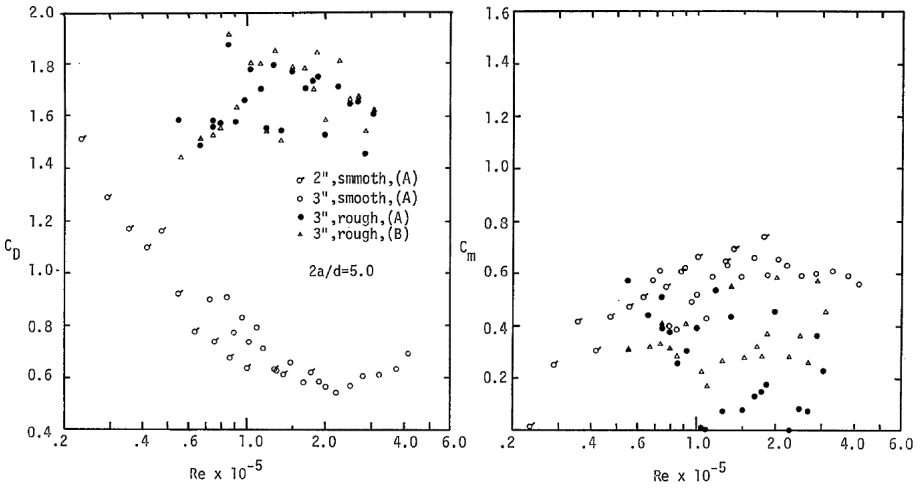

Figure 2.7: Experimental results of C_A and C_D for smooth and rough cylinders as obtained by Garrison et al. (1977). $KC = 5\pi$, Reynolds number varied along the horizontal axis.

Garrison (1980) explained the development of C_D in relation with the drag coefficients associated with steady uniform flow past a cylinder. The drop of C_D occurs for lower Reynolds number because of the earlier transition from laminar to turbulent boundary layer. As the KC-number increases, post-critical values of C_D will increase similarly as for steady flow. However, considering the wake-flow interaction, the incoming flow on the cylinder encounters the wake due to the preceding flow-cycle. This leads to an increased relative velocity and consequently a higher drag contribution on the cylinder compared with the asymptotic drag value in steady flow. As the KC further increases, the wake-flow interaction decreases, and the drag coefficient is reduced towards the steady state value of C_D for steady flows. The development of C_M is on the other side being influenced oppositely of this wake-effect. It decreases when the effect is significant, while increases again for higher KC.

Wave forces on vertical cylinders

Bearman et al. (1985) carried out tests, measuring the in-line and transverse forces on a small element of a vertical cylinder in waves, for $KC < 20$, and Reynolds numbers up $5 \cdot 10^5$. This yielded values of β between 2×10^4 and 5.49×10^4. The results of the force coefficients were to a large extent in compliance with the results obtained from tests of cylinders in planar oscillating flow as by Sarpkaya (1976a), Sarpkaya (1976b) and Garrison et al. (1977). However, they did not find any clear dependence of the coefficients

on the value of β. Garrison (1980) proposed that the most probable reason for the decrease of C_D for increasing Re was due to the wake effect rather than being dependent on Re. The significant difference in complexity between wave-induced fluid motion and pure harmonic flows, makes the practical transferability between the problems interesting. Garrison (1990) found reasonable agreement between the drag coefficient from his experiment and corresponding results from large-scale wave-tank tests (Hudspeth and Nath (1985)).

Kristiansen and Faltinsen (2017) investigated the ringing phenomenon through systematic experiments in the medium sized wave tank at NTNU Trondheim. The compliance between load estimations from inviscid FNV-theory, and experimental measurements, was studied and discussed. The horizontal in-line force was bandpass filtered into the three first load harmonics, which, as functions of the wave steepness and period, were compared to associated estimations by the FNV-theory. The FNV-theory is based on potential theory and hence excludes viscous effects such as flow separation and vortex shedding. The results showed good agreement for conditions of small wave steepness. However, discrepancies were found for higher wave steepness. Kristiansen and Faltinsen (2017) showed that the local KC-number along the cylinder axis indicated appearance of vortex shedding when discrepancies between the FNV-theory and the experiments were present. It was confirmed that an addition of a drag term, representing viscous forces according to Morison equation, and adjusting C_M and C_D after the local KC-number at the cylinder, did not explain the discrepancies. This indicated that an observed free surface effect during the testing of the steepest waves could contribute to the discrepancies. A local run-up was localized at the rear of the cylinder and was believed to be a major contributor to higher harmonic load components on the cylinder. This was supported by a 2-D CFD simulation, where a solution in a representative horizontal plane around the cylinder was coupled with the vertical component of the Navier-Stokes equation, estimating the free surface elevation around the cylinder.

Paulsen (2014) performed numerical studies in order to model the forces from steep regular waves onto the cylinder. The computational strategy was to treat the inner domain near wall boundaries as the seabed and the cylinder according to potential theory, i.e imposing slip conditions on the boundaries. The approach was justified by the assumption of insignificant vortex shedding effects due to small values of the KC-number and accordingly inertia dominated force regime. The assumption of potential flow at the boundary surfaces was sparing a lot of computational effort, allowing the omission of the computa-

tionally very requiring modelling of the boundary layer. However, it violates the findings from Kristiansen and Faltinsen (2017), where flow separation was believed to be of the high importance for the discrepancies in the third harmonics load, and forming of the local upwelling of the free surface. Nevertheless, the results showed good agreement with experiments by Grue and Huseby (2002).

2.4 Numerical modelling of turbulent flows and boundary layers

Several approaches exist for numerical modelling of turbulent flows and boundary layers. The most computational efficient in case of turbulent flows, is the Reynolds-Averaged Navier-Stokes(RANS) approach. RANS averages the Navier-Stokes equations over time. However, applying this method also addresses the need for introduction of turbulence models. Large Eddy Simulation(LES) is another approach, which is more computational demanding. It aims to solve the largest scales of motions, but only approximates the smaller ones. Direct numerical simulation is a third alternative, solving the Navier-Stokes equations for all scales of motions. However, in case of turbulent flows, this method requires excessively high computational effort. Thus, it is often reserved for solving of laminar flows. In the following, a deeper introduction of the RANS-approach is provided.

2.4.1 Reynolds-Averaged Navier-Stokes equations

Considering a steady state flow, each variable can be written as the sum of the time averaged mean value and the fluctuations around it. For an unsteady flow, time averaging is invalid and ensemble averaging must be used instead. Applying this concept to the Navier-Stokes equations yields the Reynolds-averaged Navier-Stokes equations. Dividing an arbitrary variable ϕ into a time averaged, $\bar{\phi}$, and a fluctuating component, ϕ', gives

$$\phi(x_i, t) = \bar{\phi}(x_i, t) + \phi'(x_i, t) \tag{2.74}$$

Equation 2.74 is known as Reynolds decomposition. Because the mean value of the fluctuating part, due to its property of being a Reynolds operator, must be zero, it follows that averaging linear terms in any of the conservation equations gives the identical term for the averaged variable. The quadratic nonlinear terms from the Navier-Stokes equation will on the other hand produce two terms, the product of the two averages in addition to a covariance term,

$$\overline{u_i\phi} = \overline{(\bar{u_i} + u_i')(\bar{\phi} + \phi')} = \bar{u_i}\bar{\phi} + \overline{u_i'\phi'} \tag{2.75}$$

The covariance between two variables is only equal to zero when the two variables are uncorrelated, which rarely is the case for turbulent flows. Consequently, for incompressible flows without body forces, the averaged continuity and momentum equation can be

written in tensor notation and for Cartesian coordinates as,

$$\frac{\partial \rho \bar{u_i}}{\partial x_i} = 0 \tag{2.76}$$

$$\frac{\partial(\rho \bar{u_i})}{\partial t} + \frac{\partial}{\partial x_j}(\rho \bar{u_i}\bar{u_j} + \rho\overline{u_i' u_j'}) = -\frac{\partial \bar{p}}{\partial x_i} + \frac{\partial \bar{\tau_{ij}}}{\partial x_j} \tag{2.77}$$

where the term $\rho\overline{u_i' u_j'}$ is called the Reynolds stresses. In addition, terms called turbulent scalar fluxes will be present in the conservation equation for the mean of a scalar quantity ϕ. Moving the Reynolds stresses over to the right hand side of (2.77), dividing all terms by the density ρ, and writing the mean stress tensor components $\bar{\tau_{ij}}$ according to (2.13), yields

$$\frac{\partial(\bar{u_i})}{\partial t} + \frac{\partial}{\partial x_j}(\bar{u_i}\bar{u_j}) = -\frac{1}{\rho}\frac{\partial \bar{p}}{\partial x_i} + \frac{\partial}{\partial x_j}[\nu\Big(\frac{\partial \bar{u_i}}{\partial x_j} + \frac{\partial \bar{u_j}}{\partial x_i}\Big) - \overline{u_i' u_j'}] \tag{2.78}$$

The introduction of the the Reynolds stresses and turbulent scalar fluxes into the conservation equations means that the equations are not closed anymore. In other words there are more unknowns then applicable equations available. Closure of the equations requires approximations, and introducing a turbulence model is a common way to approach the problem.

2.4.2 Turbulence models

The Boussinesq assumption states that the Reynolds stresses can be interpreted as eddy-viscosity, ν_t. The eddy viscosity is not a material constant, but dependent on the location in the flow. Introducing ν_t, the Equation (2.78) can be written,

$$\frac{\partial(\bar{u_i})}{\partial t} + \frac{\partial}{\partial x_j}(\bar{u_i}\bar{u_j}) = -\frac{1}{\rho}\frac{\partial \bar{p}}{\partial x_i} + \frac{\partial}{\partial x_j}[(\nu + \nu_t)\Big(\frac{\partial \bar{u_i}}{\partial x_j} + \frac{\partial \bar{u_j}}{\partial x_i}\Big)] \tag{2.79}$$

In order to predict the eddy viscosity ν_t, several different models can be used. Two of the most common ones are the k-ϵ model and the k-ω model. The models have different advantages and disadvantages, but generally speaking, k-ϵ models the free stream best, while the k-ω is better in terms of predicting flows close to walls. Both of these two models can be combined into another model called k-ω Shear-Stress Transport (SST) as described by Menter (1994), which aims to overcome the problem associated with the k-ω model related to its sensitiveness for inlet free stream turbulence properties, and emphasizes the importance of the shear stress transport for severe adverse pressure gradient flows. How-

ever, more recently, reformulations of the $k-\omega$ SST model have been introduced by several authors (Spalart et al. (1997), Shur et al. (2008), Spalart et al. (2006), Fröhlich and von Terzi (2008)), aiming to combine the computationally very demanding large eddy simulation(LES) with the RANS approach in order to make a hybrid RANS/LES model for simulations of turbulent flows. Detached eddy simulations(DES) is an example of this approach, switching between the RANS and LES model depending on the local grid spacing and turbulent length scale. The idea is to resolve the turbulent boundary layer by the RANS approach, avoiding the heavy computational costs associated with LES-modelling in this location. The modelling of the secondary eddies drifting away from the boundary layer is on the other hand done with LES. However, Grid Induced Separation(GIS) may occur when DES modelling is used carelessly, as announced by Spalart et al. (2003). This effect is an artificial separation, not originating from the fluid physics but rather an undesirable switch from RANS to LES inside the boundary layer of wall bounded flows. A solution was to shield the RANS modelled boundary layer from the DES formulation, as introduced by Spalart et al. (2006). This reformulation was named Delayed Detached Eddy Simulation(DDES). Later, an Improved Delayed Detached Eddy Simulation(IDDES) was formulated by Shur et al. (2008) . IDDES allows to switch between the DDES mode into a Wall Modelled LES(WMLES), meaning that only the innermost part of the boundary is solved by RANS, while LES is used for the remaining part. Proposals in order to improve the DDES and IDDES models were presented and tested by Gritskevich et al. (2012).

2.4.3 The Courant number

The role of the Courant number and its importance for the instability of the problem, as described by Courant et al. (1928), can be demonstrated by considering a simple upwind differentiating scheme(UDS),

$$\phi_i^{n+1} = \phi_i^n + \left[-u\frac{\phi_i^n - \phi_{i-1}^n}{\Delta x} + \frac{\Gamma}{\rho}\frac{\phi_{i+1}^n + \phi_{i-1}^n - 2\phi_i^n}{(\Delta x)^2}\Delta t \right] \tag{2.80}$$

where Γ is the diffusivity for the quantity ϕ and ϕ_i^n represents the value of the quantity ϕ in cell index i at time step n. Introducing two new variables d and the Courant number c, into (2.80), it can be written according to (2.81)

$$\phi_i^{n+1} = \big(1 - 2d - c\big)\phi^n + d\phi_{i+1}^n + (d+c)\phi_{i-1}^n \tag{2.81}$$

where d and c is defined as

$$d = \frac{\Gamma \Delta t}{\rho(\Delta x)^2} \quad \text{and} \quad c = \frac{u \Delta t}{\Delta x} \tag{2.82}$$

Ensuring that all coefficients on the right hand side yield positive values, introduces the following criterion to the time step Δt ,

$$\Delta t < \frac{\Delta x}{u} \quad \text{or} \quad c < 1 \tag{2.83}$$

A physical interpretation of the criterion, is the requirement for the fluid particles not to be moving longer than one grid scale Δx during the time Δt.

2.4.4 Near-wall treatment

At high Reynolds number, the viscous sublayer becomes so thin that it appears problematic to resolve it properly. To save computational effort, a wall function may be used to model the viscous sublayer. The wall functions models the near wall region, and connects it with the fully developed turbulence region. The set of boundary conditions for the turbulence and momentum transport equations are defined by "$law\ of\ the\ wall$" which applies in the logarithmic region of the boundary layer(see Figure 2.8 and equation (2.85)). The value of the non-dimensional wall distance y^+ is defined according to

$$y^+ = \frac{u_\tau y}{\nu} \tag{2.84}$$

where u_τ is the friction velocity, and y is the distance to the wall. When wall functions are being used, the y^+ value of the first cell should fall into the logarithmic region, corresponding to a y^+ value above 30. Figure 2.8 illustrates this concept. u^+ and the logarithmic law are defined by the following relations:

$$u^+ = \frac{u}{u_\tau} \quad , \quad u^+ = \frac{1}{k}\, ln(y^+) + C \tag{2.85}$$

Where u is the mean velocity parallel to the wall and C and k are constants.

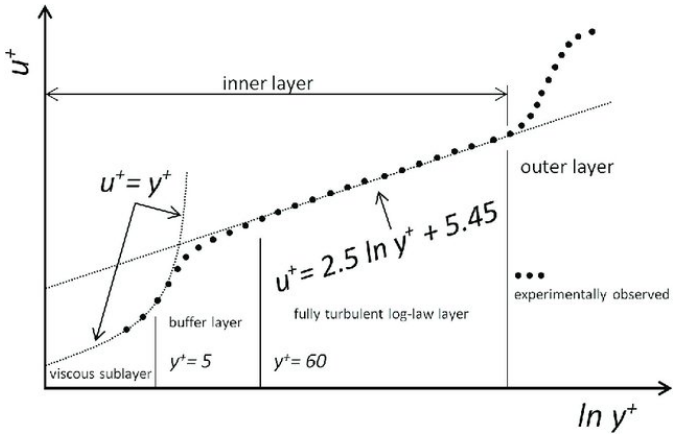

Figure 2.8: The relation between u^+ and y^+, in the different sub-layers of the boundary layer (ANSYS (2009)).

2.4.5 Software and hardware

ANSYS Fluent

ANSYS FLUENT, hereby referred to as $Fluent$, was the preferred software in this project. Fluent is a commercial computational fluid dynamic software package. Computational fluid dynamics provides analysis which also considers viscous effects in the fluid, in contradiction to potential flow theory. The process of a CFD simulation usually consists of several phases. First of all, a mathematical model reflecting the idealised problem must be made. Examples of these choices can be whether the scenario is steady state or transient, and if the flow is laminar or turbulent. In relation to these assumptions, a suitable solver and turbulence model have to be chosen.

A CFD analysis solves the Navier-Stokes equations numerically, and associated discritization methods of the mathematical equations must be determined. In addition a discritization of the computational domain must be performed, according to the finite volume method which the CFD-software is based upon. Furthermore, the equations are being solved iteratively, until a finite number of time-steps, or, in case of a steady state problem, until a converged solution is reached. Afterwards, the solution needs to be validated, often through comparison with experimental results.

High performance computing

Because of the high requirements to computational resources associated with CFD, the simulations are often performed on a so called cluster. The cluster consists of several nodes working together, where each node represents computational power. In this work the Idun-cluster at NTNU was employed, allowing rapid performance of simulations and testing. Because of the high amount of simulations performed in total during the work, the HPC computing became a powerful tool in order to complete all the necessary simulations.

Chapter 3

Experiment

A 1:48 scaled model experiment was performed in order to investigate the Ringing loads in practice, reusing major parts of the set-up from Bachynski et al. (2017), carried out for Statoil related to the development of the Dudgeon wind farm. The experiment was conducted in the small towing tank at NTNU in Trondheim. A similar experiment was also accomplished by Kristiansen and Faltinsen (2017). The main focus in the experiment related to the present work was neither the loads nor the response measurement, but visual documentation of the interaction between vortex shedding from the cylinder and the free surface. The vortex shedding induced changes in the pressure field behind the cylinder is believed to be the cause of an induced vertical flow at the rear of the cylinder, forming a local upwelling of the free surface. In addition, because of the limited extra amount of effort, the wave loads from a window of the regular wave series in main focus were measured and compared to what obtained by Kristiansen and Faltinsen (2017), and to the numerical analysis in the present work.

The scale problematic with respect to the Reynolds number are well known within model experiments. Decreasing the characteristic length and velocity also decreases the Reynolds number, which means that the flow regimes not will be identical in the full and model scale cases. The boundary layer will consequently become turbulent for a lot smaller value of KC in full scale than model scale, potentially delaying the flow separation in full scale. As the drag contribution for a bluff body mainly depends on the pressure distribution around, and not the skin friction on the cylinder, this could have impact on the horizontal force on the cylinder.

3.1 Experimental setup

The set-up consisted of a monopile that was mounted onto the tank bottom, in order to achieve negligible response vibrations of the model. The wet natural period was $0.041\mathrm{s}$, corresponding to a wet natural frequency of $24.39\mathrm{Hz}$. The wave loads were measured in terms of the horizontal in-line force and the mud-line moment by force transducers. A wavemaker in the rear of the tank generated regular wave series of varying steepness and period, incoming from right to left (Figure 3.1). Regular waves were generated in series of 60 wave periods, with 180 seconds pause between each series. Six wave gaugers were used, placed according to Figure 3.1. The model dimensions and wave periods were scaled by Froude scaling, meaning that the diameter of the monopile in full scale, $D = 6.9\mathrm{m}$, was equal to $0.144\mathrm{m}$ in model scale. The water depth in the model experiment was $56.3\mathrm{cm}$, corresponding to $h = 27\mathrm{m}$ in full scale. The beach was placed $57\mathrm{cm}$ above the tank bottom. The water temperature was measured between $15 - 17^{\circ}\mathrm{C}$ during the experiments. The force measurements series showed consistently independence of date and time of the measurements, and the force transducers were thus considered to be quite robust against small changes in water temperature.

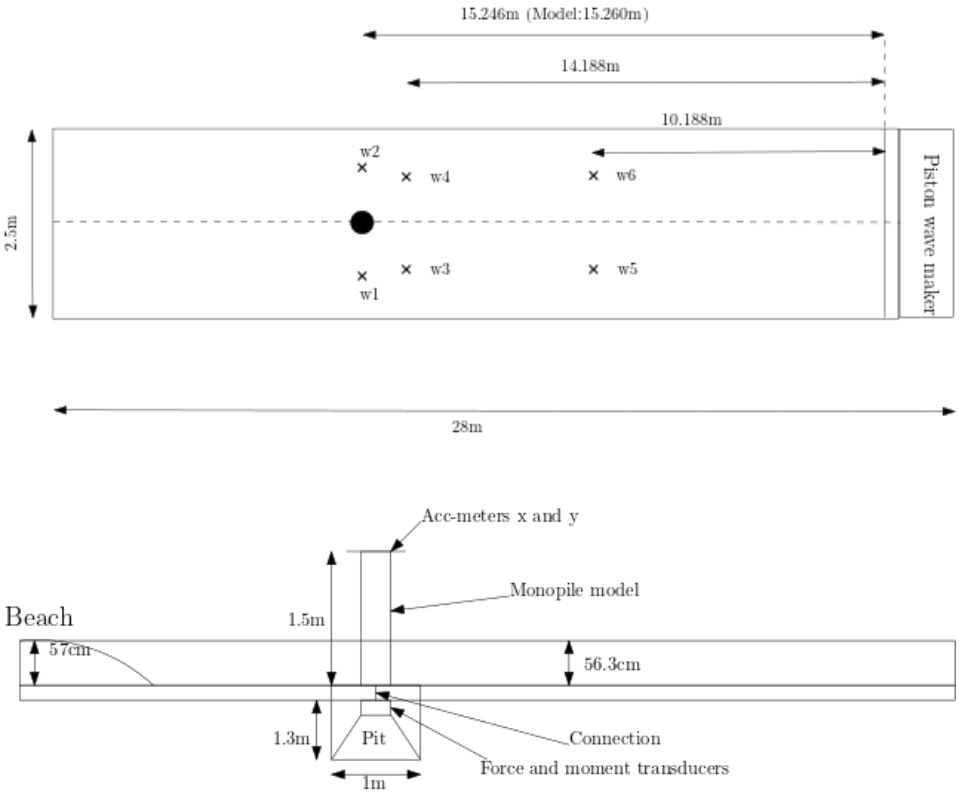

Figure 3.1: Bird eye and side view of the experimental setup that was used in the model experiment. The focus was on flow visualization, thus an underwater camera was recording upwards along the rear of the cylinder.

A small underwater camera was placed on the tank bottom at the rear side of the cylinder, recording upwards in order to try capturing the sought flow effects. Potassium permanganate was the chemical substance used in purpose to visualize the flow. The substance was sprayed from a thin pipette sunk into the water close to the localizations where the vortex shedding was assumed to take place. In addition, above-water recordings were taken, in order to visualize the local run-up of the free surface.

3.2 Test program

Three regular wave series of model scale periods: 1.44s, 1.73s and 1.02s were tested with varying wave steepness, H_1/λ: $1/40$, $1/30$, $1/28$, $1/26$, $1/24$, $1/22$, $1/20$. Here, the linear wave height H_1 is used in the definition of the wave steepness. The wave periods correspond to 10s, 12s and 14s in full scale, i.e. wave series where third and fourth harmonics cause resonant response of the monopile. In table 3.1, characterizing dimensionless parameters related to each wave series of steepness $1/20$ and $1/30$ are presented. Both the related Reynolds number and KC-numbers are calculated using the first order velocity amplitude u_{m1}, and hence denoted KC_1 and Re_1. u_{m1} is found using first order dispersion relation($\omega^2 = g\ k\ \tanh(kh)$), and evaluated at $z = 0$. The Ursell numbers are calculated using the linear wave height H_1.

		$H_1/\lambda = 1/20$			$H_1/\lambda = 1/30$		
T (s)	ka	Ur	KC_1	$Re_1/10^4$	Ur	KC_1	$Re_1/10^4$
1.443	0.163	6.03	3.55	5.10	4.02	2.36	3.40
1.732	0.127	12.63	5.12	6.12	8.42	3.41	4.08
2.021	0.105	22.44	6.96	7.14	14.96	4.64	4.76

Table 3.1: Information of wave kinematics and flow conditions for the three tested wave periods given in model scale, for steepness $H_1/\lambda = 1/20$ and $H_1/\lambda = 1/30$.The values of the Ursell number indicates that applying Stokes fifth order wave theory is valid for all wave conditions.

3.3 Comments on the experiment

Some comments should be made to the experiment, around its importance in the present work and the plausibility of the experimental results. As remarked previously, the intention of the experiment was to focus on the developing flow patterns at the rear of the cylinder, and the interaction between vortex shedding and the free surface. Not nearly enough time was spent with systematic wave series testing to obtain throughout reliable results of the force measurements. Thus, the experimental results from Kristiansen and Faltinsen (2017) will be emphasized in Section 5.1. However, a small analysis was also dedicated to the experiment from the present work, in order to establish the validity of the related results. Figure 3.2 shows the first, second and third harmonic amplitudes of ζ, calculated according to Stokes fifth order wave theory as presented by Skjelbreia and Hendrickson (1960), together with the corresponding values from the waves generated by the wave maker in the experiment. The amplitudes of the harmonics from the experiment were obtained through band-pass filtering of the measured time series of the free surface elevation at wave gauge 2. The measurements show in general better compliance with the theory for lower wave steepness and periods. Two of the most prominent disagreements between experiments and theory are found for $H_1/\lambda = 1/20$ at $T = 1.732$s and $T = 2.021$s for the amplitudes of the third harmonic. Another remarkable large discrepancy is observed in the plot of ζ_{a2}, at $H_1/\lambda = 1/20$ and $T = 2.021$s. The mismatches between amplitudes of the experimental wave harmonics and Stokes fifth order wave theory imply for certain waves limited plausibility of the measured force series. However, Figure 3.2 demonstrates that for several other wave series, there are higher agreement between theory and experiments.

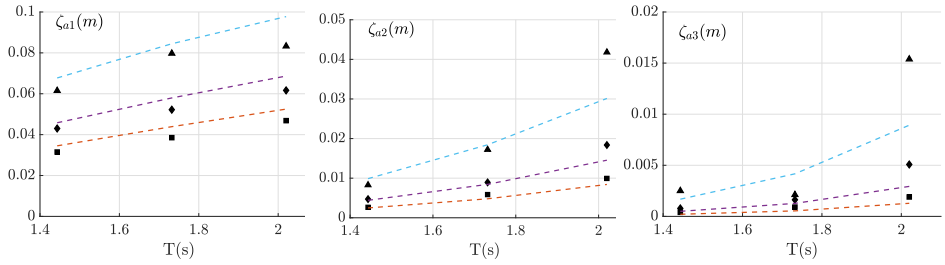

Figure 3.2: Amplitudes of the three first harmonics; ζ_{a1}, ζ_{a2} and ζ_{a3}, according to Stokes fifth order waves(dashed lines), compared to corresponding amplitudes of extracted wave harmonics from the experiment(markers). ■, $H_1/\lambda = 1/40$; ◆, $H_1/\lambda = 1/30$; ▼, $H_1/\lambda = 1/20$. Wave periods are given in model scale.

3.4 Visual observations

The main objective from the experiments was to visualize the formation of the flow-patterns at the rear of the cylinder. Earlier experiments (e.g. Kristiansen and Faltinsen (2017)) have confirmed the formation of a local run-up behind the cylinder, which also was observed here. In this experiment, obtaining visual documentation of the vortex shedding and the subsequent pressure-initiated flow run-up at the cylinder rear was attempted by colouring the flow. An underwater camera was placed at the tank bottom rear of the cylinder, recording upwards along the model. The effort was, however, rather in vain, as the potassium permanganate dissolved very quickly in the water. The substance was only colouring the water, and not revealing the effects that were looked for. Syrup was tried being mixed into the potassium permanganate in order to make the substance more viscous, but this approach was neither successful. The legality of changing the viscosity of the fluid is also questionable, while it probably would affect the flow patterns. The substance was being sprayed out at the awaited location of flow separation on the cylinder. A very thin pipette was used for this purpose, sunken down into the water at approximately 20cm below the free surface. The wrong choice of equipment or inappropriate location of releasing the substance may be other explanations why the experiment was unsuccessful. The presence of the pipette close to the boundary layer is very likely to disturb the flow in one of its most critical locations, and should be avoided. A better approach could have been to spray the substance through an extremely small hole in the cylinder, made at a location where visualization of the flow was desirable. The feasibility of this approach is, however, unknown. Nevertheless, the above-water recordings were showing the discussed local run-up of the free surface at the rear of the cylinder. An illustration can be found in Figure 3.3.

Figure 3.3: The formation of the local rear run-up, visualized in terms of a snapshot from video recorded during experiments. Wave conditions model scale; $T = 2.02s$ and $H_1/\lambda = 1/20$. Incident waves incoming from right towards left.

Chapter 4

Numerical Model

In order to carry out a two dimensional CFD analysis in Fluent, a numerical model was obtained. The computational model of the cylinder cross section was designated with the same dimensions as the monopile model in the experiment, i.e 1:48 of full scale. A total computational domain was split into several subdomains, permitting employment of a block structured grid. This simplified the investigation of the necessary amount of elements both in radial and tangential directions to the cylinder. Mesh convergence studies were performed in this purpose, varying the number of elements closer to the cylinder surface, as well as the number of elements along the cylinder surface N_c. The influence of the variation on the force coefficients C_M and C_D was investigated. A stability study and an assurance of domain-size independence were also carried out. Simulations of harmonic oscillating flows of KC-numbers in range 1-16 around the cylinder were performed in each study. The flow was periodic with $T = 1.732s$, corresponding to the second to largest wave period from the model experiment. Results of the inertia and drag coefficient were afterwards interpreted and compared between the different parameter refinements. Reducing the computational costs while at the same time achieve the necessary numerical accuracy was the main focus.

4.1 Set up and validation of the two dimensional model

4.1.1 Grid structure

The geometrical domain and its subdivided domains, are illustrated together with the block-structured grid in Figure 4.1. A block structured grid has several advantages compared to an unstructured grid. First and foremost, the connectivity between neighbouring elements leads to a more expedient and simplified solving procedure. The user also achieves improved control of how many elements that are used when the grid is generated. However, it may be challenging to generate the grid without also provoking undesirable regions of high cell concentration. Other problems related to block structured grids are often associated with advanced geometries, where the unstructured grid usually becomes a better choice. However, because of the rather simple geometry in the present case, a block structured grid was considered to be the most beneficial choice.

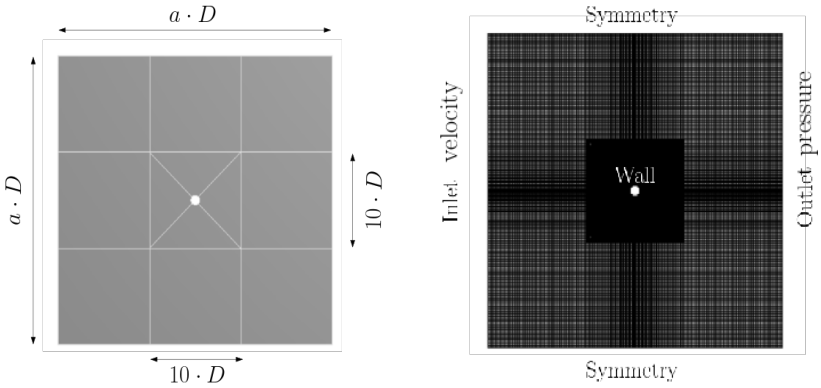

Figure 4.1: Left: The division of the computational domain into several subdomains with description of the geometrical lengths where D represents the diameter of the cylinder, and $10 \leq a \leq 30$. Right: Visualization of the mesh with specified boundary conditions.

4.1.2 Boundary conditions

The boundaries and associated boundary conditions were defined according to Figure 4.1. Because the simulations were performed in 2-D, symmetry conditions were imposed on both the front and back of the domain. Because an infinite fluid was considered, the same condition was applied on both the top and bottom boundaries. The cylinder was treated as a fixed wall, with the associated no-slip condition on the cylinder surface.

At the inlet boundary, the incoming velocity was defined using a table file, which set the

velocity values at the inlet for each time-step. The values of the velocity amplitude u_{mi} corresponded to KC-number i. The incoming velocity at each time step were calculated according to an harmonic oscillating flow; $u_i = u_{mi}sin(\omega t)$. The pressure values at the outlet were calculated from the Navier-Stokes equation in x-direction. Assuming uniform flow, the remaining terms become

$$\frac{\partial u}{\partial t} = -\rho \frac{\partial p}{\partial x} \tag{4.1}$$

Assuming that $p|_{x=-L/2} = -p|_{x=L/2}$, the integration of (4.1) along the length of computational domain yields

$$\int_{-L/2}^{L/2} \frac{\partial p}{\partial x} dx = -\rho \int_{-L/2}^{L/2} \frac{\partial u}{\partial t} dx \tag{4.2}$$

$$p|_{x=L/2} = -\frac{1}{2}\rho L \frac{\partial u}{\partial t} \tag{4.3}$$

This means that the pressure is $\pi/2$ out of phase with the velocity, but in phase with the horizontal force on the cylinder. The linear pressure distribution along the domain is illustrated in Figure 4.2 .

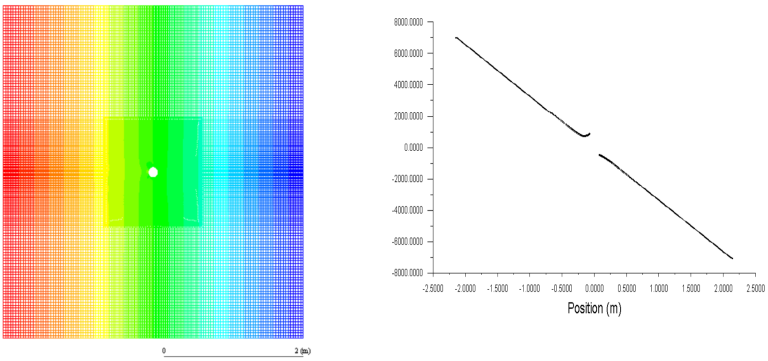

Figure 4.2: Left: Contour representation of linear pressure distribution. Right: Line plot representation of linear pressure distribution, plotted along the in-line direction in the middle of the domain.

4.1.3 Turbulence model

The modelling of the boundary layer in oscillating flow was found intricate for several reasons. As already discussed, the transition from laminar to turbulent flow happens a lot earlier than for steady state flows, bringing uncertainty around the value of the critical Reynolds number. However, investigations made by Sarpkaya (1986), where oscillating flows around a cylinder at low Re were studied, suggested that for $\beta = 11240$ ($\beta \approx 11930$ in present case), the critical numbers of transition corresponded to $Re_{cr} = 6400$, or $KC_{cr} = 0.57$. If so, the transition from laminar to turbulent flow in the boundary layer happens before the most vital KC-numbers concerning the wave conditions in the present study. All the waves would thus be generating flows around the cylinder in the critical or post-critical flow regime, which justifies the application of a turbulence model. However, as the values of the critical Reynolds number are rather uncertain, and the differences between applying a laminar or turbulent model to the boundary layer were of interest to investigate, both approaches were tried out and compared afterwards.

Pang et al. (2016) performed comparisons of the different two-equation RANS models ability to capture the right angle of separation and estimate the drag coefficient on a 2-D cylinder in uniform steady high Re flow. The $k-\omega$ SST model provided the best results, most in agreement with experimental values. It was also showed that including a curvature correction in the model, which is possible in Fluent, improved the results more. Hence, the $k-\omega$ SST model, with curvature correction, was considered to be the most efficient turbulence model for the present work. It should be remarked, that the grade of success using a turbulence model is highly dependent on the mesh resolution, number of time-steps, and flow-properties. Higher KC are associated with higher velocities, and according to the Courant number, the numerical model becomes more vulnerable to instability. In addition, the requirements to the mesh are also depending on KC. The value of y^+ should preferable be kept below 1, and at least well inside the viscous sublayer ($y^+ < 5$). This requires smaller width of the cylinder-adjacent cells for higher KC. Thus, the computational costs associated with accurately modelling of the flow increase quite significantly with higher KC. A trade off between computational costs and accuracy, ensuring the necessary reliability of the model for the most important KC-numbers, was necessary.

The $k-\omega$ SST was, as mentioned, applied as the turbulence model. However, in order

to check whether the choice of turbulent or laminar model affected the results or not, applications of the IDDES model and the laminar model were also tried out.

4.1.4 Numerical scheme

The PISO algorithm was chosen as the preferred solver algorithm as it is highly recommended for transient cases. One feature of the PISO algorithm is its ability to provoke instability, even for higher values of time step. Both the neighbour and skewness corrections were set equal to one. The spatial discretization gradient used was the standard choice by Fluent; Least Squares Cell-Based Gradient Evaluation. The pressure interpolation scheme was set to Second Order, while the interpolation schemes for the momentum, turbulent kinetic energy and specific dissipation rate were Second Order Upwind. The Second Order Implicit formulation was used as the transient formulation.

4.2 Convergence studies

Convergence studies were carried out, in order to verify the independence of the computational model with respect to grid refinement as well as time-step and domain size. The convergence tests were performed by simulating cases for KC in range $1 - 16$, although the maximum KC-numbers relevant for simulating waves around the cylindrical pile were assumed to be no higher than 10. As can bee seen from the studies, the model only shows consistency for $KC \leq 9$. For larger values of KC, high amount of apparently random scatter is observed, implying that the model have clear limitations in these flow regimes. The reliability of the model for varying KC-numbers will henceforth through the section be discussed.

4.2.1 Grid studies

The influence on the results of the number of elements in the radial direction to the cylinder was investigated closer (see Figure 4.3). N_r is in the following denoting the number of elements from a point at the cylinder surface radially out to the square of sides $10D$ enclosing the cylinder. The element size gradually decreases as one moves closer to the cylinder surface, where the thickness of the innermost cell is 100 times smaller than the outermost, at the square enclosing the cylinder. In the plot of the drag coefficient, the coarsest refinement of the boundary layer seems to be leading to higher values of the drag coefficient compared with the higher grades of refinements. The results deviates largely from the other refinement grades at $KC = 9$, both for the inertia and drag coefficient. In contrast, $Nr = 150$, $Nr = 200$ and $Nr = 250$ show very similar results for $KC \leq 9$. However, the number of elements inside the boundary layer are recommended to be at least 10. In case the boundary layer is laminar, the thickness of it can be calculated according to

$$\delta^{99} = 4.6 \cdot \sqrt{\frac{2\nu}{\omega}} \tag{4.4}$$

where δ^{99} is the laminar boundary layer thickness, defined by the distance from the cylinder to where the local velocity is 99% of the free stream velocity. As $Nr = 200$ was yielding 11 cells inside the boundary layer, it was decided to be sufficiently in order to resolve the boundary layer properly. However, another aspect is, as explained by ANSYS (2009), that the wall-adjacent cells should be placed outside the buffer layer when a turbulence model is applied. That means $5 < y^+ < 30$ should be avoided. Ideally, $y^+ \approx 1 - 2$.

The simulations showed that y^+ exceeded five for $KC \approx 4$. Thus, a more refined mesh should be made to ensure sufficiently small y^+ for higher KC when a turbulence model is applied.

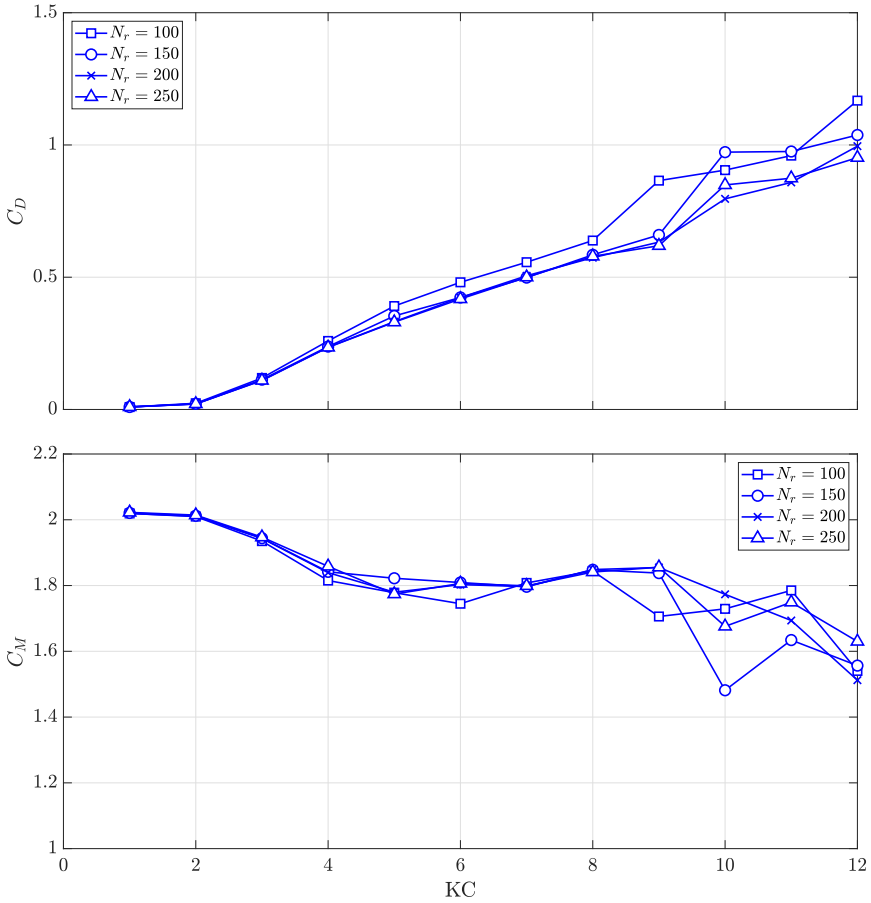

Figure 4.3: The drag coefficient, C_D, and the inertia coefficient, C_M, as functions of the KC-number for varying number of elements along the cylinder surface. Simulations performed with 4000 time-steps per flow period, $N_\theta = 240$ and $a = 30D$.

Figure 4.4, shows the dependence study of the number of elements along the cylinder surface, denoted N_c, of the mass and drag coefficient. The drag coefficient shows consistent results, independent of the refinement grade, up to $KC = 9$. Thereafter, more scattering are observed. Also the plot of the inertia coefficient illustrate very small dependency of N_c for $KC \leq 9$. However, the coarsest mesh seems to lead to a delayed drop of the inertia coefficient. Thus, with respect to computational costs, $NC = 240$ was chosen to be used

further.

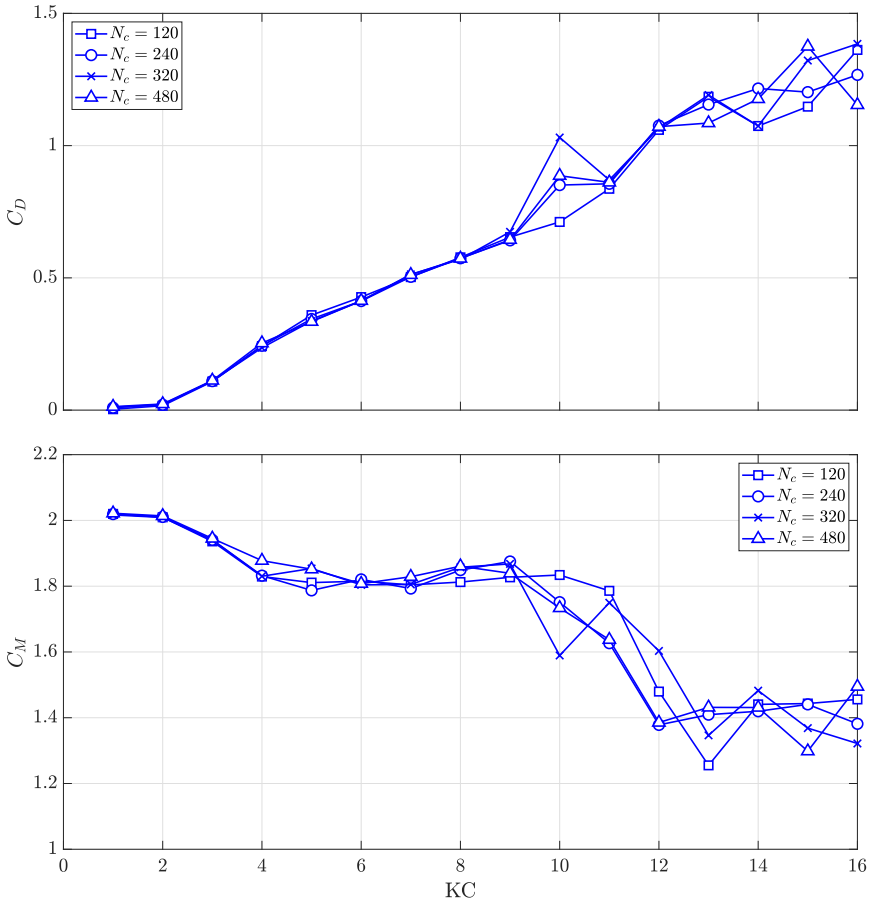

Figure 4.4: The drag coefficient, C_D, and the inertia coefficient , C_M, as functions of the KC-number for varying number of elements along the cylinder surface. Simulations performed with 4000 time-steps per flow period, and a domain size of $a = 30D$. $Nr = 200$

4.2.2 Time step study

The time step sensitivity study is presented in terms of Figure 4.5, where the coefficients are plotted as functions of KC for varying number of time-steps, Nt. The results show consistency up to $KC = 9$. However, to keep the Courant number below 1 for $KC = 9$, 5000 time-steps per oscillation was necessary. Thus, $Nt = 5000$ was chosen to be used in future simulations.

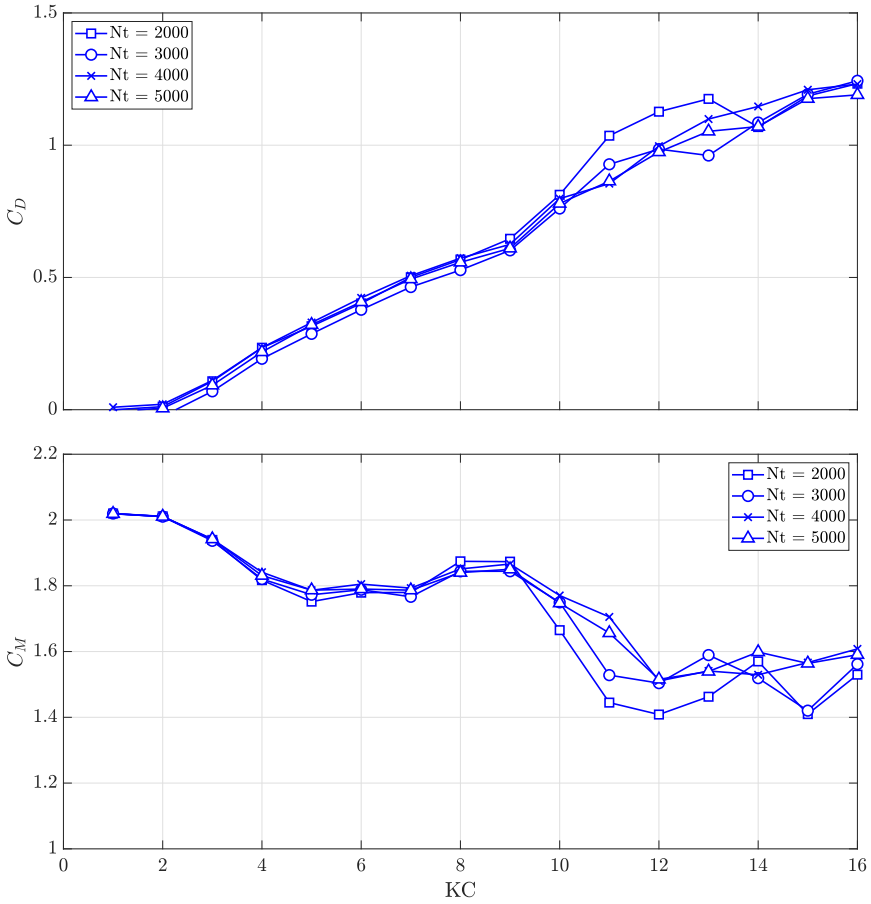

Figure 4.5: The drag coefficient, C_D, and the inertia coefficient , C_M, as functions of the KC-number for varying number of time steps per flow-period. Simulations performed with $N_\theta = 240$, $N_r = 200$ and $a = 30D$.

4.2.3 Domain size study

The effect of the domain size on the results was also tested through several repeated simulations where the domain size was varied, see Figure 4.6. For $KC \leq 9$, applying a domain size of $a = 20D$ was largely consistent with using $a = 35D$. Thus, $a = 20D$ was set as the domain size in the future simulations. The domain size together with the chosen values of N_c and N_r provided a total number of quadrilateral elements equal to 56500.

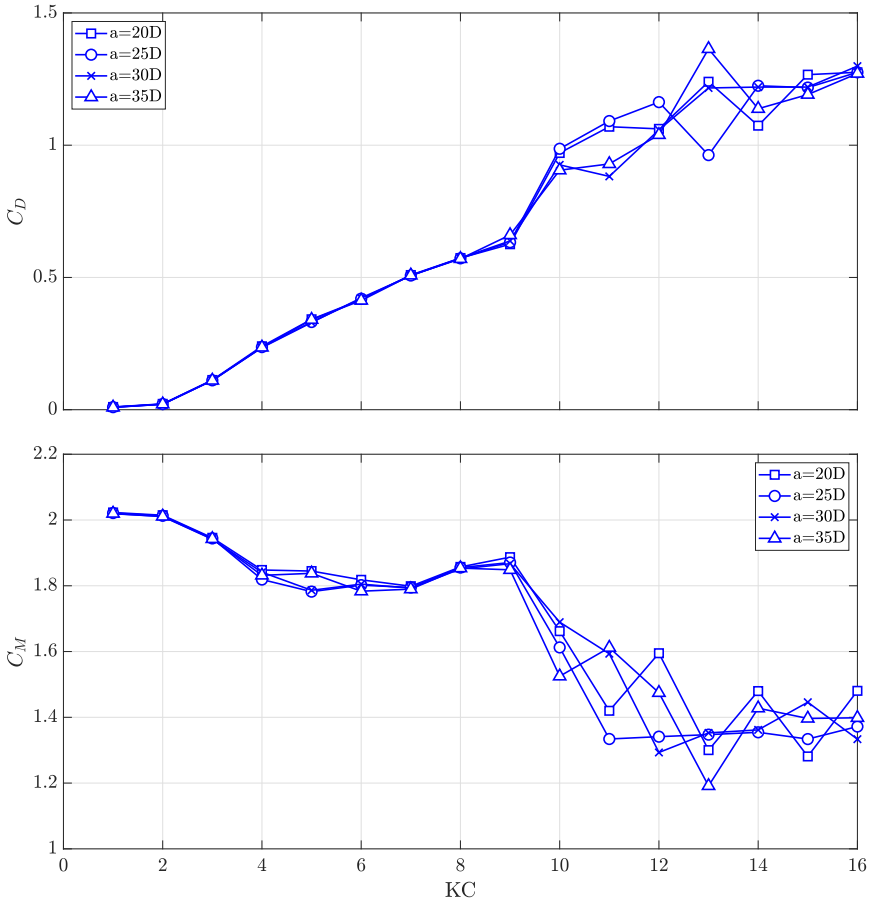

Figure 4.6: C_D and C_M as functions of the KC-number for different domain sizes defined by the variable a. Simulations performed with $N_\theta = 240$, $N_r = 200$ and 4000 time-steps per flow period.

4.3 Validation of the numerical model

Several approaches to model the boundary layer were applied when validating the numerical model. In addition to the $k-\omega$ SST model, the IDDES formulation for turbulence modelling was tested. Although the findings from Sarpkaya (1986) indicated that the boundary layer transitions from laminar to turbulent for very low Reynolds number for oscillating flows, we do not know whether or when the boundary layer transitions in the present case. Thus, also treating the boundary layer without any turbulence model was tried out. This corresponds to choosing the *laminar model* in Fluent, which solves the Navier-Stokes equations directly, similar to DNS. The numerical results were validated against experimental results of C_M and C_D as functions of KC and Re. Sarpkaya (1987) and Garrison et al. (1977) have, as reviewed earlier, carried out experiments of 2-D cylinders in sinusoidal oscillating flows. In addition, comparisons to experimental values from Bearman et al. (1985) are also included. It should be noted that the latter experiment is performed with a vertical cylinder in waves, and thus not fully comparable to results of sinusoidal flow. However, the agreement between the experimental and numerical results was examined and commented.

Although the grid obtained in the convergence studies showed independence of refinement for C_M and C_D, it was not found fine enough to model the vortex shedding from the cylinder sufficiently. In addition, when applying a turbulence model, the y^+ values was found to be outside the viscous sublayer for $KC \gtrsim 4$. Thus, a refinement of the mesh was performed, making it more suitable for higher KC and velocities. The width of the wall-adjacent cells in the boundary layer was decreased in order to obtain acceptable values of y^+. This also provoked an increased number of cells inside the boundary layer. Additionally, N_c was increased to 320 elements to better capture the separation point on the cylinder. This yielded a total number of 90500 elements in the grid. The coarser and refined mesh will henceforth be referred to as Mesh 1 and Mesh 2, respectively. Mesh 1 was applied for the $K-\omega$ SST model up to $KC = 5$, thereafter Mesh 2 was used. Because there was too short amount of time to carry out new convergence studies, Mesh 2 was used when applying the laminar model or IDDES turbulence model. Figure 4.7 shows the vorticity fields using the two respective meshes with the $k-\omega$ turbulence model for $KC = 6$.

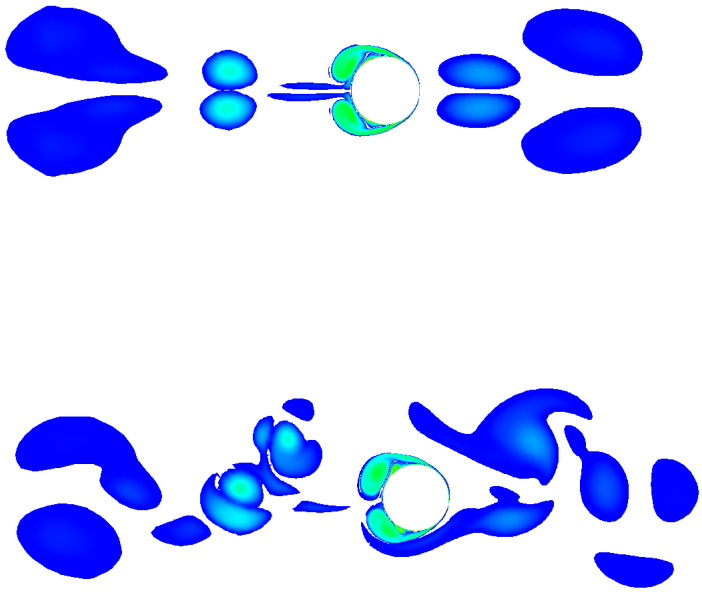

Figure 4.7: The vorticity field around the cylinder using the two respective meshes are illustrated, for $KC = 6$. The $k-\omega$ SST turbulence model is applied. The symmetry of the vortices using Mesh 1 indicates that it is too coarse for the CFD-software to calculate the vortices accurately.

4.3.1 C_M and C_D as functions of KC

The models were compared to experiments by Sarpkaya (1987) and Bearman et al. (1985). Here, the title *"as functions of KC"* is a bit misleading, as the Reynolds number indeed will adjust with changing KC. Thus, one should remember the frequency parameter β, characterizing the KC-curve. The experimental values by Sarpkaya (1987) was obtained at $\beta = 11525$, while for the experiments by Bearman et al. (1985), β is between 2×10^4 and 5.49×10^4. The viscosity of the numerical simulations was adjusted such that β complied with the experiments by Sarpkaya (1987). The results provided with $K - \omega$ SST, IDDES, and the laminar model are plotted with the experimental values in Figure 4.8. Note that Mesh 1 is used for $KC \leq 5$ for the $k - \omega$ SST model, while Mesh 2 is applied for higher KC and for the other models.

The incapability of all models to estimate the drag coefficient for $KC < 4$ are remarkable. Skin friction drag is expected to give rise to the drag coefficient for very low KC. However, for some reason, the models seem to neglect this contribution to the drag coefficient. Instead, the drag coefficient starts to increase as expected after the occurrence of flow separation, implying that the drag is fully due to pressure drag. However, the skin friction drag is in general of minor importance compared to the pressure drag for a cylinder. For $KC \lesssim 6$, the force is highly inertia dominated, and thus mainly dependent on the value of C_M. The value of the inertia coefficient is, as anticipated, in accordance with potential theory for low KC, subsequently decreasing as the flow separates from the cylinder.

Modelling the boundary layer with a turbulence model yields higher values of C_D, according to Figure 4.8. Comparing with the experiments, the three models seem to provide reliable estimations of the in-line force up to $KC = 9$. For higher KC, the development of the coefficients are unexpected. Nevertheless, the range of KC where the models are well-working should be sufficient to compute reliable loads from the planar flows generated by the waves considered most important in the present work. When the boundary layer transitions from laminar to turbulent is unclear, but earlier studies suggest that the critical regime of Reynolds number is significantly lower than for a cylinder in steady flow. Thus, the $k - \omega$ SST turbulence model was applied, as it is less computational demanding than IDDES. However, the critical flow regime is extremely difficult to model accurate, using CFD. Precise representation of the flow separation and the subsequent reattachment of the flow normally requires more advanced and computational demanding numerical models than what is obtained in the present case.

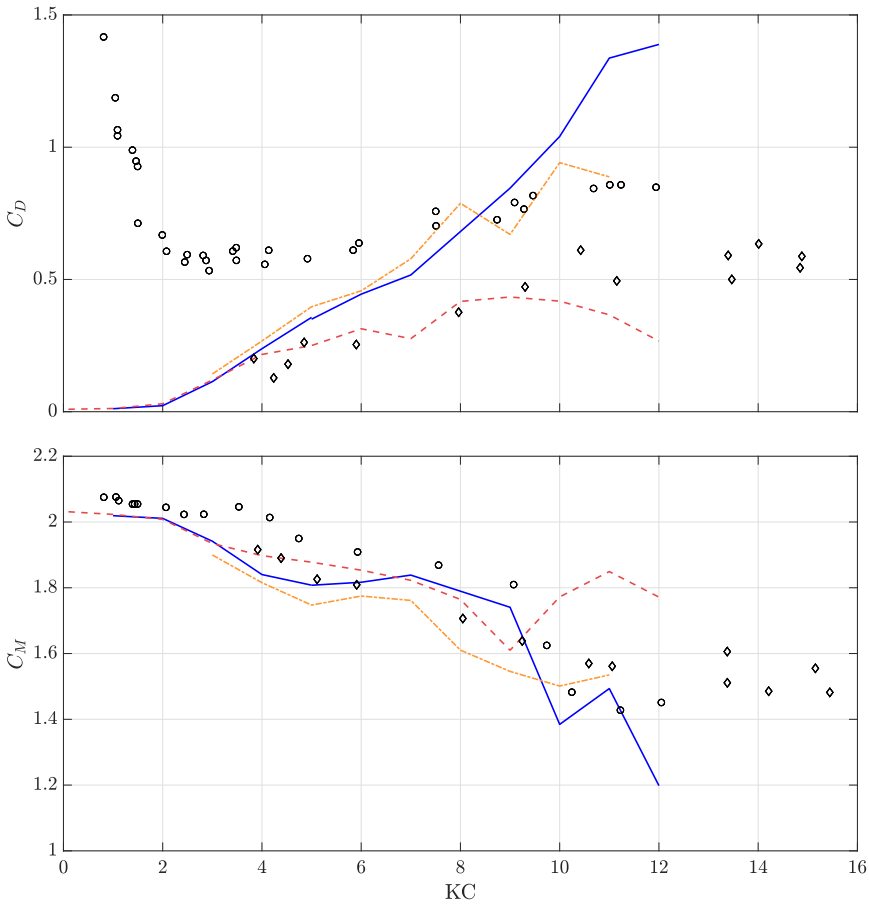

Figure 4.8: Development of C_D and C_M coefficients as functions of KC, compared to experiments by Sarpkaya (1987) and Bearman et al. (1985). $\beta = 11525$ in the numerical simulations and in the experiments performed by Sarpkaya (1987) .β between 2×10^4 and 5.49×10^4 in the experiments by Bearman et al. (1985). Note that the latter experiment considered waves, and not mono-harmonic flow. ∘, Sarpkaya (1987)(mono-harmonic oscillating flow); ◇, Bearman et al. (1985)(waves); ——— , $k-\omega$ SST model; - - - - - , Laminar model; -·-·-·- , IDDES model.

4.3.2 Reynolds number dependency of C_A and C_D

The numerical model was tested with variations of Re, at fixed KC, and compared with the experimental values by Garrison et al. (1977). The $k-\omega$ SST turbulence model was used. In Figure 4.9 are the numerical results of the added mass coefficient, C_A, and the drag coefficient, C_D, plotted for KC corresponding to π, 2π and 3π. For $KC = \pi$, the added mass coefficient is in strong agreement with the experimental results. The drag coefficient is, despite somewhat smaller values, neither far off the experiments. However, C_D seems less dependent on the Reynolds number than what demonstrated in the experiments. The experimental values of the drag coefficient has a steeper drop between $Re = 0.5 \times 10^5$ and $Re = 1 \times 10^5$ than what is the case in the numerical simulations. Considering the inertia dominance of the in-line force for $KC < 2\pi$, the strong agreement between the numerical and experimental values of the inertia coefficient justifies the application of the numerical model in this regime.

For $KC = 3\pi$, larger deviations occur between the experiments and the numerical results. This is especially visible for Re in range of 1×10^5 and 1.5×10^5. Both the force coefficients differ here significantly from the experimental measurements by Garrison et al. (1977). The flow regimes correspond to KC between 9 and 10 in Figure 4.8. Here, in contrast, neither of the force coefficients are far off the experiments by Sarpkaya (1987). However, the force coefficients are observed to have unexpected development for higher KC. Thus, the values of the force coefficients for $KC \gtrapprox 9$ are considered to contain a high degree of uncertainty. Nevertheless, the validation of the model has justified fair agreement of the numerical model with experiments for $KC \lessapprox 9$. This is considered to be within the range of the most important KC numbers in the present study.

More time was spent trying to obtain a numerical model appropriate for higher KC. Especially the number of time-steps was considered necessary to increase, while the Courant number was implying instability. However, this introduced a problem in terms of increased computational costs. The simulation time of eight oscillations using one node of the Idun-cluster, was originally $5-6$ hours for $KC = 9$. The simulation time exceeded 20 hours when the number of time-steps per oscillation was increased to 8000. Application of the IDDES turbulence model increased the costs even more. The institute of Marine Technology has no share in IDUN cluster, and the use of it was therefore limited for the present work. Thus, the obtained numerical model, considered sufficiently reliable for $KC \lessapprox 9$, was carried on with further.

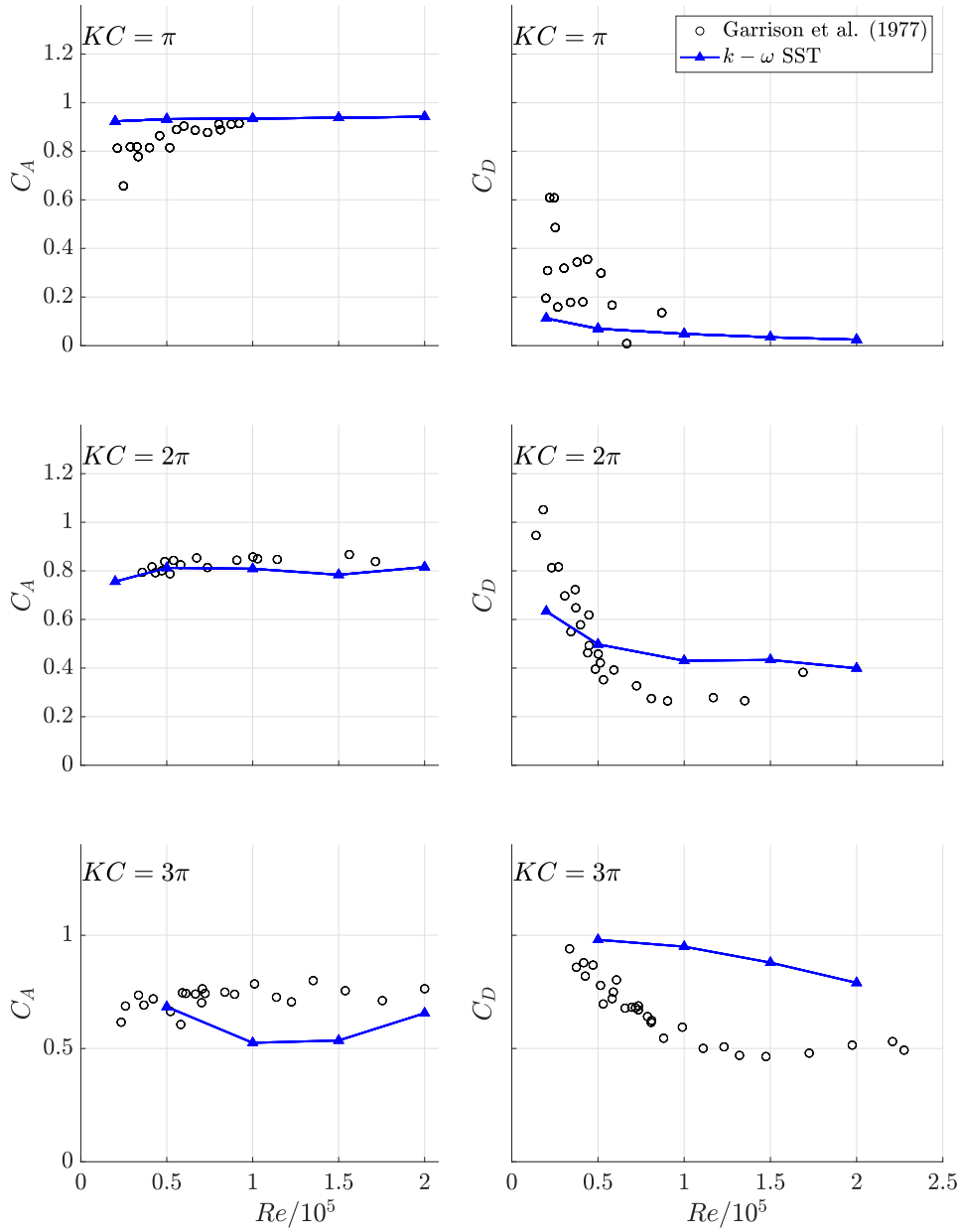

Figure 4.9: Results of C_A and C_D from the numerical model, using the $k - \omega$ SST turbulence model, compared to the experimental values obtained by Garrison et al. (1977). Mesh 1 applied for $KC = \pi$, Mesh 2 for the others.

4.4 CFD-FNV model

To include viscous effects in the FNV load-estimation, a viscous term integrating sectional 2-D CFD forces on the cylinder were replacing the force term proportional to $\frac{\partial u}{\partial t}$ in the FNV-theory. In order to obtain the correct CFD-force at the respective cut of the cylinder, u and p at the vertical position of each cylinder cut were needed to be calculated in time from Stokes fifth order wave theory. The discretizaton of the cylinder, and how the boundary conditions were calculated accordingly, are hence dedicated a briefly review. The water depth considered corresponded to the conditions from the model experiment, i.e. $h/a = 7.83$.

4.4.1 Discretization of the cylinder

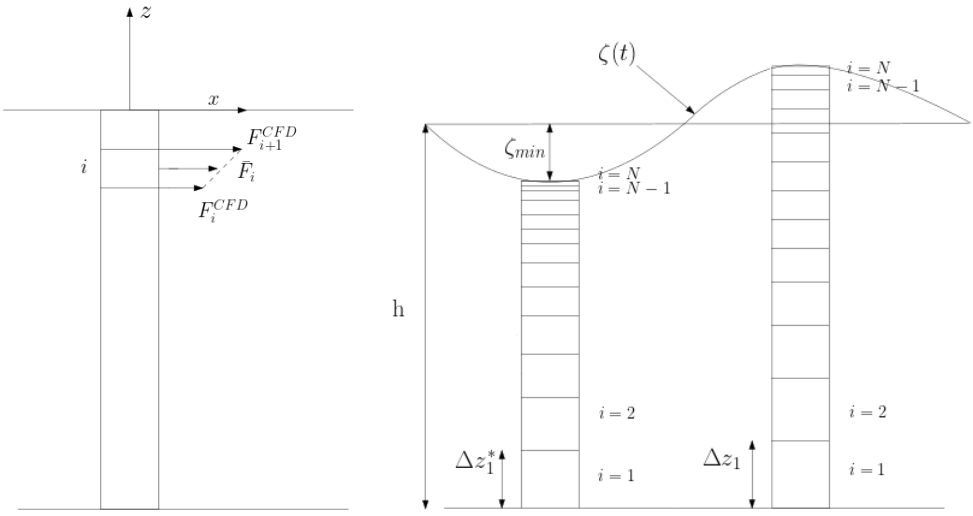

Figure 4.10: Left: The horizontal force, $\bar{F}_i$, at strip i, is calculated by interpolation between CFD force-outputs at upper and lower cuts of the strip, F_i^{CFD} and F_{i+1}^{CFD}. Boundary conditions u and p evaluated according to Stokes fifth order wave theory at the horizontal cuts. Right: The strips are contracting and expanding according to $\zeta(t)$. Note that in the following, $cuts$ will refer to the lines dividing the cylinder, while $strips$ are referring to the divided elements with thicknesses Δz_i. N is denoting the number of strips. The water depth $h = 0.5625$cm is considered.

In order to integrate the horizontal force from the CFD simulations along the submerged part of the monopile, the cylinder was divided into several strips(see Figure 4.10). As seen, the strips thickness is gradually decreasing as one move upwards up to the fifth order incident free surface, justified by the more rapidly changing flow kinematics in z-direction

here. An exponential approach was used in order to calculate the initial thickness of strip i, Δz_i^*, according to (4.5)

$$\Delta z_i^* = \alpha \cdot \left(e^{-\beta \frac{i+1}{N+1}} - e^{-\beta \frac{i}{N+1}} \right) \tag{4.5}$$

where N is the total number of strips, β is the stretching coefficient, typically set to a value around 0.8, while α is the factor such that the sum of all of the strip equals the submerged part of the cylinder, i.e.

$$\alpha = \frac{h - \zeta_{min}}{\sum_{i=1}^{N} \left(e^{-\beta \frac{i+1}{N+1}} - e^{-\beta \frac{i}{N+1}} \right)} \tag{4.6}$$

the minimum length of the submerged cylinder is set to h - ζ_{min}. An approach of stretching the strip according to the fifth order incident free surface were chosen, known as a Lagrangian approach. The approach leads to continuously incident flow at each cylinder cut during the simulation. Another possibility would have been the Eulerian approach, which considers fixed strips and thus discontinuous forces on the cuts that are located above the minimum free surface elevation. However, applying the Lagrangian method, (4.5) and (4.6) were used to calculate the initial strip thickness. The thickness of the strips were afterwards stretched dependent on the incident free surface $\zeta(t)$

$$\Delta z_i(t) = \Delta z_i^* \, \frac{\zeta(t)}{h - \zeta_{min}} \tag{4.7}$$

where $\Delta z_i(t)$ is the stretched strip thickness of strip i. When using stretched (moving) mesh, this must be accounted for in the equations of motions of the fluid, i.e. the Navier Stokes motions. In a fully three-dimensional simulation, a modification of the material derivative term (advection term) in the Navier-Stokes equations is necessary. Since the mesh only is stretched vertically, a modification would be necessary only in the vertical direction. However, since we are not performing three-dimensional computations, but rather assume strip-theory and solve the problem by a series of two-dimensional cuts along the cylinder, the only consequence of the stretched mesh is that Δz is a function of time, and Δz is used in the integration of the horizontal force on the cylinder. If a slender-body theory was attempted, on the other hand, the material derivative would have been necessary to modify, as discussed.

4.4.2 Implementation of Stokes fifth order waves

In order to simulate wave-generated flow around 2-D sections of the cylinder, planar flows according to Stokes fifth order theory were needed to be implemented. A script calculating the wave profile ζ, potential ϕ, velocity u as well as derivatives of u according to Skjelbreia and Hendrickson (1960), was provided by supervisor Trygve Kristiansen. The script was modified, in order to account for the Lagrangian discretization scheme. The vertical coordinates of the cuts were evaluated at each time-step, in order to evaluate the correct boundary conditions as input to the CFD-simulations, and the time varying strip thickness, Δz. The numerical approach of calculating the quantities was done similar to Kristiansen and Faltinsen (2017), differentiating between the two intervals $-h \leq z \leq 0$ and $0 \leq z \leq \mid \zeta_I \mid$. Here, ζ_I is the fifth order incident wave profile. In the latter interval, the quantities are evaluated by Taylor expansion up to fifth order according to

$$f(z) = (f_1 + f_2 + f_3 + f_4 + f_5) + z\frac{\partial(f_1 + f_2 + f_3 + f_4)}{\partial z} + \frac{z^2}{2}\frac{\partial^2(f_1 + f_2 + f_3)}{\partial z^2} + \frac{z^3}{6}\frac{\partial^3(f_1 + f_2)}{\partial z^3} + \frac{z^4}{24}\frac{\partial^4}{\partial z^4}f_1 \tag{4.8}$$

where f_i and its derivatives are evaluated at $z = 0$.

The number of cuts along the cylinder equals N+1, corresponding to the number of simulations required for each wave condition. 19 strips were in the discretization of the cylinder. The horizontal normal force at the midpoint of strip i, $\bar{F}_i$, was calculated by interpolation between the force outputs from the simulations at the cuts (F_i^{CFD} and F_{i+1}^{CFD} in Figure 4.10). Thereafter, $\bar{F}_i$ was multiplied with the strip thickness at the corresponding time-step, in order to obtain a 3-D force. The time series of the forces corresponding to each strip of the cylinder could be summed together, yielding a time series of the total horizontal force from Fluent, F^{CFD}.

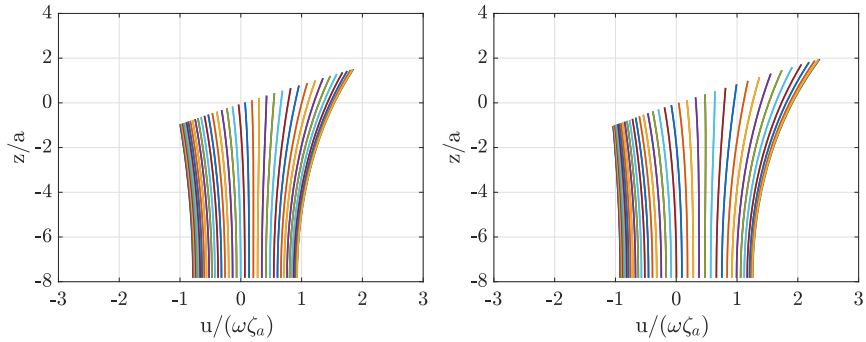

Figure 4.11: Left: The horizontal velocity u calculated according to fifth order stokes theory for $ka = 0.127$. Right: $ka = 0.105$. In both plots, $H/\lambda = 1/20$, N = 19 and time intervals of T/80 is used.

The three model scale periods corresponding to full scale periods of $T = 10s$, $T = 12s$ and $T = 14s$, were considered when estimating the wave loads on the cylinder with the combined CFD-FNV model. Each wave period was simulated with wave steepness of $1/40$, $1/30$, $1/25$ and $1/20$. The different wave conditions are certainly generating different flow regimes on the cylinder, also depending on the location on the vertical axis of the cylinder. This will be further discussed as the local flow regimes along the vertical axis of the cylinder are investigated closer.

Flow regimes of the cylinder cuts

The flow regime experienced by a horizontal strip of the cylinder is highly dependent on the location on the vertical axis. According to Figure 4.11, the flow velocities are increasing significantly closer to the free surface. For $ka = 0.105$ in Figure 4.11, as pointed out by Kristiansen and Faltinsen (2017), the velocity at the sea-bottom due to a wave crest is of higher magnitude than the velocity at the free surface due to a passing wave through. This highlights the increased significance of viscous effects, such as flow separation, in the wave propagation direction. The fact that the strips are moving vertically synchronously with the fifth order free surface also means that the flow regimes experienced by the strip will change in time. The maximum value of KC for each section during one wave-period, calculated according to Stokes fifth order theory, are presented for all of the numerically considered wave conditions in Figure 4.12. Because the velocity amplitude according to fifth order Stokes theory is used when calculating KC, the notation KC_5 is here applied. As seen, the maximum values of KC_5 during longer and steeper waves, indicate that significant flow separation is present. However, for the most severe wave conditions, flow

separation can also be expected at the lower sections of the cylinder. Based on the observations from Figure 4.12, the numerical simulations were performed with two different meshes when the $k-\omega$ SST turbulence model was applied. For $KC \gtrapprox 4.5$, where Mesh 1 was found inappropriate due to y^+ values outside the viscous sublayer, the refined Mesh 2 is applied instead. Thus, we achieve sufficiently low values of y^+ for the cuts located at the upper parts of the cylinder, where the velocities are higher and a turbulent boundary layer is expected. In addition, using a coarser mesh for the lower parts of the cylinder saves computational costs.

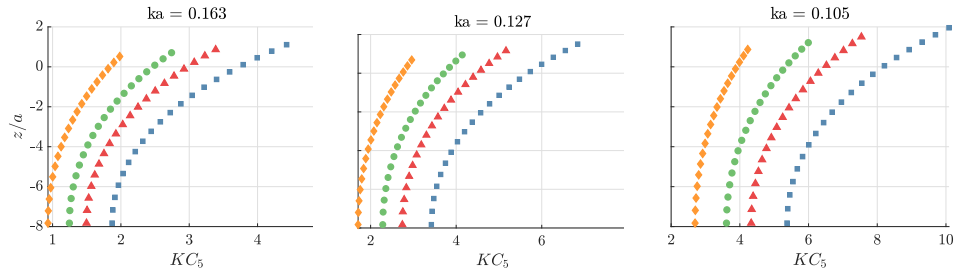

Figure 4.12: The maximum value of KC_5 during one wave period for each section of the cylinder(horizontal axis), plotted against corresponding vertical position of the sections(vertical axis). In total 20 cuts are applied, including the top and bottom, along the cylinder-axis according to the stretched mesh discretization of the cylinder. Note the significant increase in KC_5 for higher wave periods and steepness. ◆, $H_1/\lambda = 1/40$; ●, $H_1/\lambda = 1/30$; ▲, $H_1/\lambda = 1/25$; ■, $H_1/\lambda = 1/20$.

4.4.3 The load terms

The motivation behind introducing 2-D CFD to solve this problem, was to obtain a force-estimation model also accounting for viscous effects, which stands in contradiction to classical FNV-theory. Thus, the terms in the fifth order FNV-model also accounted for by the numerically computed in-line force on the cylinder was replaced. The terms of (2.70) are rewritten and named to clearly illustrate the definition and substitution of terms.

$$F_1 = (\rho\pi a^2 + a_{11})\frac{\partial u}{\partial t} \tag{4.9}$$

$$F_2 = \rho\pi a^2 u\frac{\partial u}{\partial x} \tag{4.10}$$

$$F_3 = (\rho\pi a^2 + a_{11})w\frac{\partial u}{\partial z} \tag{4.11}$$

F_1 is substituted with the 2-D CFD-force, meaning that the 3-D horizontal in-line force on

the cylinder as computed by the CFD-FNV model can be expressed accordingly

$$F_x = F^{CFD} + \int_{-h}^{\zeta_I} (F_2 + F_3) + F^{\psi} \tag{4.12}$$

The second force term is evaluated by numerical integration, using the velocities and gradients according to Stokes fifth order theory, which for $0 \leq z \leq |\zeta_I|$ is Taylor expanded to fifth order according to (4.8).

Chapter 5

Results

The results obtained from the numerical analysis was compared to the experiments from the present work, as well as to the earlier experiments performed by Kristiansen and Faltinsen (2017). Especially the third harmonic load amplitudes were investigated and commented on closely, while the former work by Kristiansen and Faltinsen (2017) showed over-estimation of these compared with experiments, when applying fifth order FNV-theory generalized to finite water depth. The importance of reliable estimations of the third harmonics, considering the resonance frequency of OWT monopiles, is once more remarked. Hence, the ability of the combined load model, consisting of 2-D CFD and theory, to estimate first and higher harmonic in-line loads from waves onto the vertical cylinder is dedicated a comprehensive discussion.

5.1 Comparison between CFD-FNV, inviscid FNV and experiments

The three first harmonics of the load estimated by the CFD-FNV model for $ka = 0.127$ and $H_1/\lambda = 1/20$ are shown in Figure 5.1. Additionally, the corresponding time series measurements of the load harmonics from the experiment are presented. Kristiansen and Faltinsen (2017) confirmed discrepancies in the third harmonic loads between the fifth order FNV-theory and experiments under identical wave condition. As shown, the discrepancies in the third harmonic loads are indubitable clear in Figure 5.1. The combined CFD-FNV model is, similar to the FNV-theory, over-estimating the amplitudes of the third

harmonic load. In addition, a phase shift can be observed between the third harmonics. In contrast, the first and second harmonic load estimations from the CFD-FNV model comply better with the experimental measurements. This was also found to be the case by Kristiansen and Faltinsen (2017), when applying pure fifth order FNV-theory to estimate the harmonic loads from longer and steeper waves. Thus, a first glance implies similar tendencies in the results of the present work. However, it is necessary to consider more wave conditions before making any conclusions to the general trends of the load-estimations using the combined CFD-FNV model.

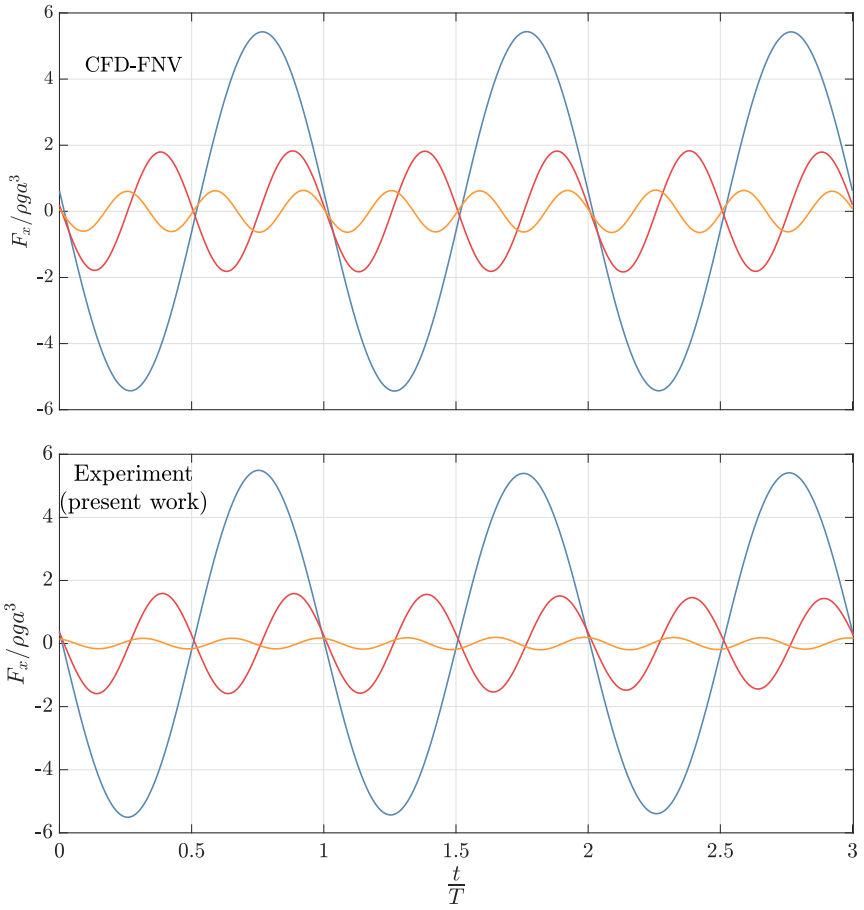

Figure 5.1: The three first load harmonics as calculated by the CFD-FNV model, and the measured time-series from the experiment, respectively. Note that the first order harmonics comply the most, while there are visible discrepancies between the third harmonics, both in terms of phase and magnitude.

The CFD-FNV model's load predictions for varying wave period and steepness are plotted together with inviscid fifth order FNV-theory, the experimental results from Kristiansen and Faltinsen (2017), and the experimental measurements from the present work in Figure 5.2. Firstly, some remarks are made to the results from the latter experiment, as the force measurements from these tests not was validated through any form of uncertainty or quality check. The first and third harmonic amplitudes are nevertheless, for the most, in fair agreement with what obtained by Kristiansen and Faltinsen (2017). This is in contrast to the second harmonic loads for $ka = 0.163$ and $ka = 0.105$, where clear deviations appear between the experimental results. The deviations in the second harmonics loads are probably because parasitic waves not were accounted for in the present experiment. Kristiansen and Faltinsen (2017) added a 2ω signal to the wavemaker, in order to diminish the effects of the parasitic waves. In addition, parasitic waves have been shown to influence the third and first harmonic loads. Another possible explanation for general deviations in the results between the experiments can be beach reflection effects.

The motivation behind introducing the force-term computed by Fluent into the FNV-theory was to account for viscous effects, such as flow separation. Similar to the FNV-theory, the combined CFD-FNV load model are estimating the third harmonic loads in thread with the experiments up to a wave steepness of approximately $1/40$. Thereafter, the third harmonics are over-estimated by both load-models. The combined CFD-FNV model is to an even greater extent over-predicting the third harmonic loads compared with the inviscid FNV-theory, although the difference is small. Regarding the lower load harmonics, the results from both load-models are in fair agreement with the experiments by Kristiansen and Faltinsen (2017). The results in Figure 5.2 reveal that substituting the F_1 forcing term from the inviscid FNV-theory, with the viscous-effects accounting forcing term as computed by Fluent, did not bring better compliance between the load-estimation model and experimental results.

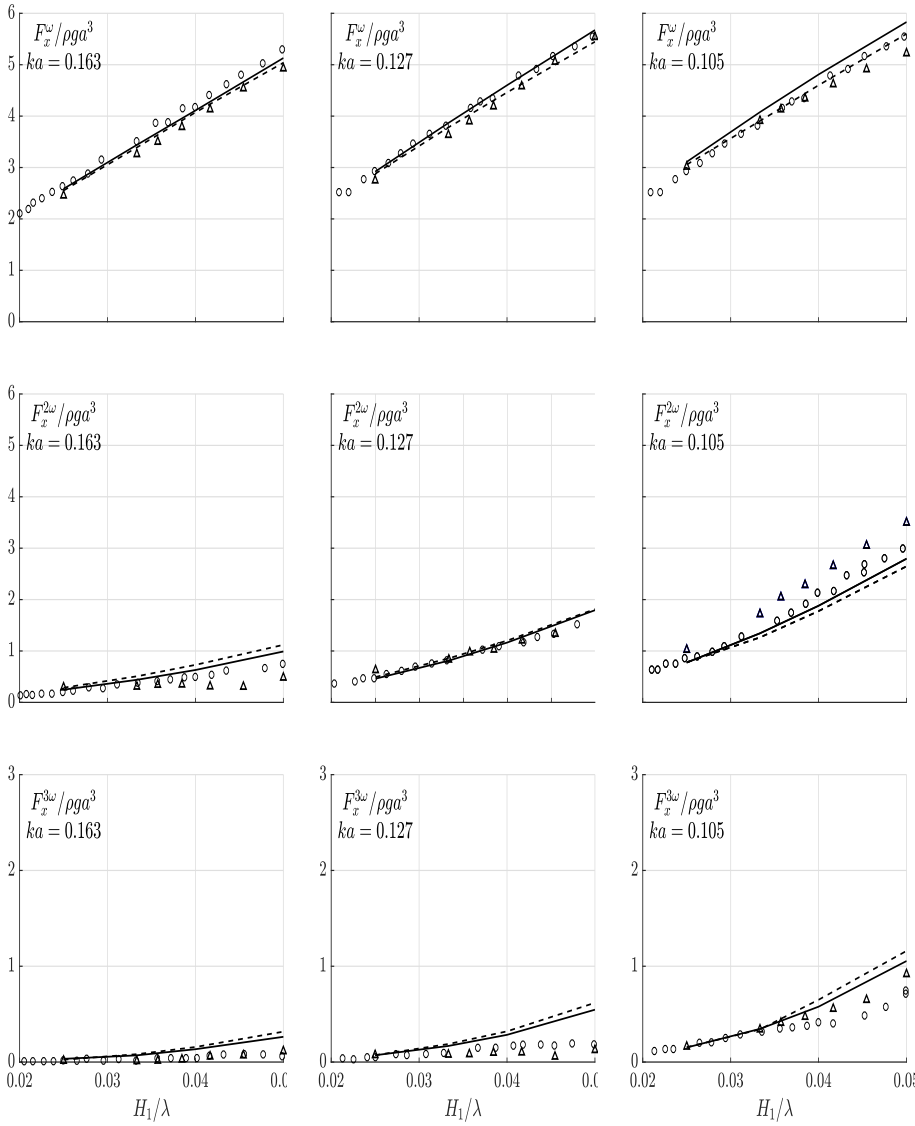

Figure 5.2: Non-dimensional amplitudes of the three first load harmonics versus non dimensional wave-number ka. ○, Experiments Kristiansen and Faltinsen (2017); △, Experiments present work; ———— , FNV; - - - - - , CFD-FNV.

The differences in load-estimation by the CFD-FNV load-model and the inviscid FNV-theory, comes due to the substitution of the first forcing term in the inviscid FNV-theory, F_1, with the viscous Fluent-force. Thus, it makes sense to compare the two forcing terms with each other. In Figure 5.3, the three first harmonics of F^{CFD} are plotted versus the corresponding harmonic of F_1. One of the wave conditions where discrepancies between the forcing terms appeared is considered; $ka = 0.127$ and $H_1/\lambda = 1/20$. The dashed lines represent the force term F_1, proportional to $\frac{\partial u}{\partial t}$, while the solid lines correspond to the harmonic loads as computed by Fluent. Figure 5.3 shows that the amplitudes of the first harmonic are almost of the same magnitude in both the viscid and inviscid forcing term. However, a phase shift between the first harmonic loads, due to the viscous forces included in the CFD force-term, can be observed. The second harmonics are in contrast identical, being in the exact same phase and of the same magnitude for both F_1 and F^{CFD}. The third harmonic amplitudes are, as seen in Figure 5.3, not decreased by substituting the F_1 force term from the inviscid FNV-theory with the viscous force from Fluent. Instead they increase somewhat in magnitude. There is no significant phase shift between the two third harmonics.

The combined CFD-FNV model, also including planar viscous effects, did not explain the discrepancies between the theory and experimental results of the third harmonic amplitudes. The validation of the numerical model showed on the other hand, for KC-numbers in range of what considered most vital for the present study, fair agreement between the force coefficients on the cylinder computed by Fluent in sinusoidal flow, and corresponding experimental values obtained by Garrison et al. (1977) and Sarpkaya (1987). The results indicate, thus, that the two dimensional viscous effects not are the cause behind the discrepancies in the third harmonics between inviscid fifth order FNV-theory and experiments. However, the modelling of the boundary layer in case of critical flow regimes is, as already mentioned, extremely difficult. The application of other viscous model were also tested, in order to see whether this could affect the results.

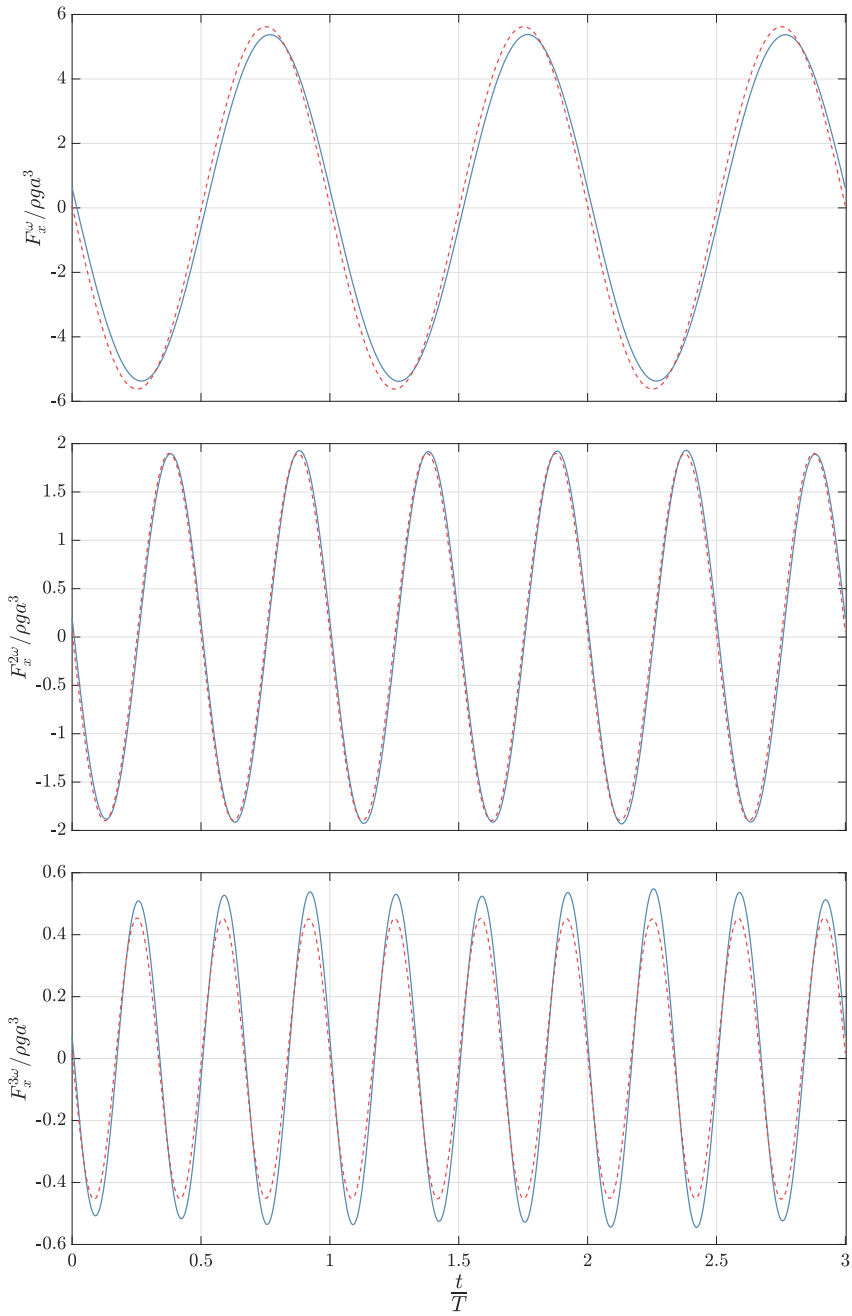

Figure 5.3: Comparison between the three first load harmonics of the inviscid force-term F_1, and the force compute by the CFD-software. - - - - - , F_1; ——— , F^{CFD}. Wave condition: $ka = 0.127$ and $H_1/\lambda = 1/20$.

5.2 Effect of viscous model

Both the laminar model and the IDDES turbulence model was applied to see if this would affect the results. There was limited time to perform new analysis, and thus two selected wave conditions where discrepancies in the third harmonic load had been confirmed were considered. The wave conditions corresponded to the non-dimensional wave number $ka = 0.127$, with steepness $1/20$ and $1/25$.

In Figure 5.4, are the results of the amplitudes for the three first load harmonics, using the $k-\omega$ SST turbulence model, plotted for wave steepness $1/40$ and $1/25$. All three wave periods, with the non-dimensional wave numbers 0.163, 0.127 and 0.105 are included. In addition, results from using the laminar and IDDES model, with wave steepness $1/25$ and $ka = 0.127$, are showed. The results from the latter wave condition demonstrate, for all three load harmonics, that the choice of viscous model does not influence the magnitude of the amplitude to any considerable extent. Using the IDDES model, provides results of somewhat smaller amplitudes for all three harmonics, compared to the $k-\omega$ SST and the laminar model. This may be due to numerical dissipation. The mesh was not optimized for the application of the IDDES model, and LES is in general very sensitive to the grid scales. However, the results for the other wave conditions using the $k-\omega$ SST model, confirms the trend observed in Figure 5.2. The CFD-FNV model is, similar to the inviscid FNV-theory, complying with experiments for steepness $1/40$. For steepness $1/25$, on the other hand, discrepancies in the third harmonic amplitudes are present for all of the considered wave periods.

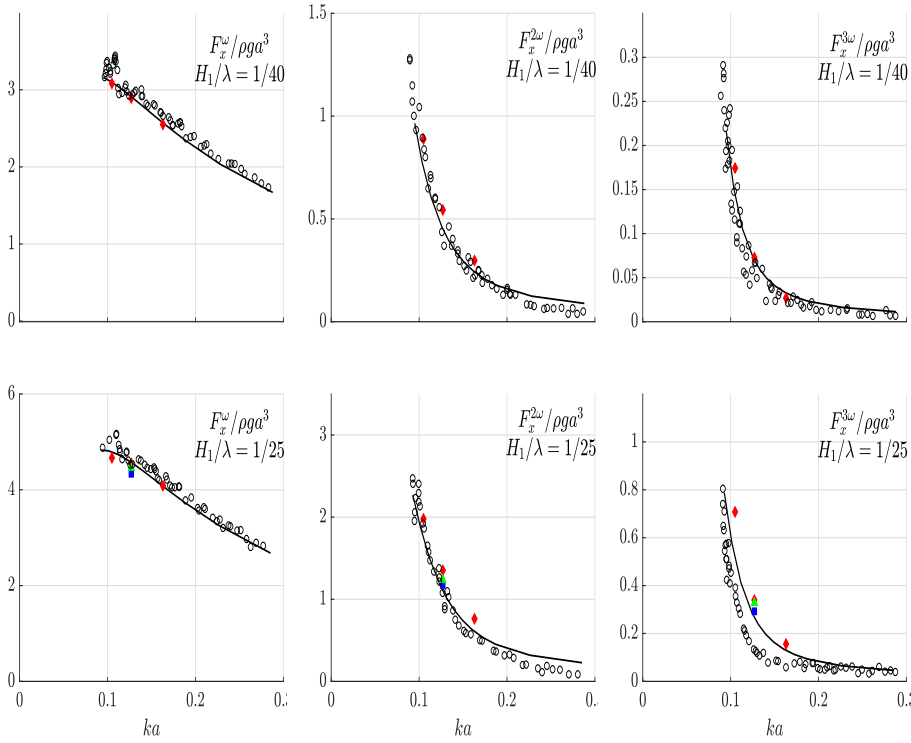

Figure 5.4: Non-dimensional amplitudes of the three first load harmonics versus non dimensional wave-number ka. ○, Experiments Kristiansen and Faltinsen (2017); ◆, CFD-FNV($k-\omega$ SST); ■, CFD-FNV(IDDES); ▲, CFD-FNV(laminar); ———— , FNV.

5.2.1 Vorticity field

Subsequent to the numerical simulations, the vorticity field around the cylinder was visualized. In Figure 5.5 are the vortices at the upper cut of the cylinder plotted at three time instants: $t = 0$, $t = T/4$, and $t = T/2$, for the $k - \omega$ SST model (top), the IDDES model (middle) and the laminar model (bottom). The consequences of a full RANS approach are clearly visible in the first case, observing that a lot of the vorticity is dampened out due to the time-averaged flow field. The IDDES is, in contrast to $k - \omega$ SST, also using LES to model the eddies outside the boundary layer. This leads to a more descriptive vorticity field, as seen in Figure 5.5. The laminar model is not applying the RANS approach at all, visible in terms of less damped vorticity fields around the cylinder.

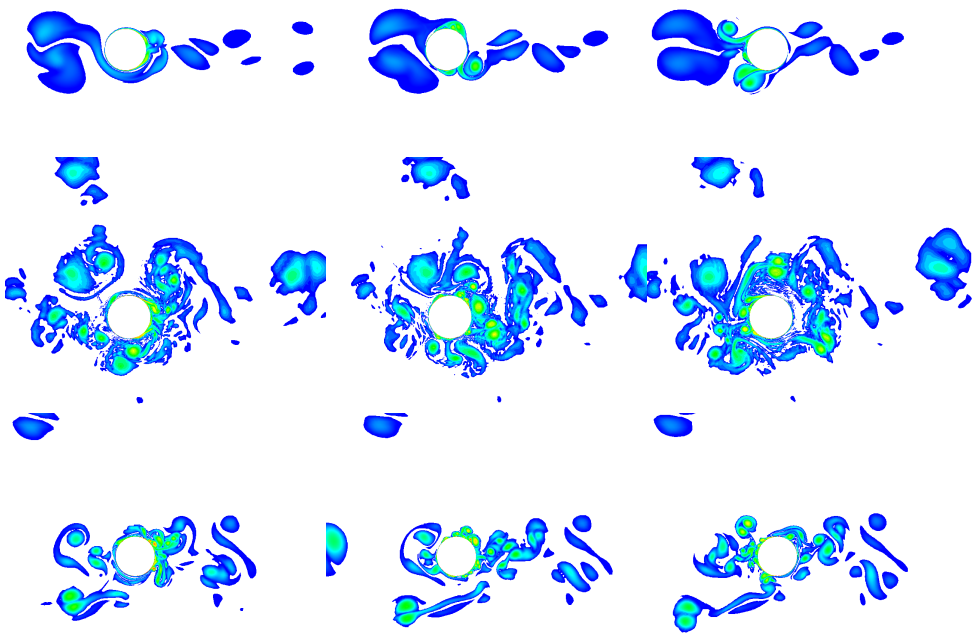

Figure 5.5: Visualization of the vorticity field around the cylinder at three time instants using the $k-\omega$ SST model(top), the IDDES model(middle), and the laminar model(bottom). The cut at the top of the submerged cylinder is considered. The respective time instants are taken within the seventh oscillation of in total eight oscillations.

5.2.2 Pressure distribution on the cylinder

It was also of interest to investigate how the pressure distribution on the cylinder was influenced by the choice of viscous model. Thus, the pressure along the curve length of the cylinder was plotted for all three models, at five selected time-instants, in Figure 5.6. The plots corresponds to cut 10 of the cylinder, with wave conditions of $ka = 0.127$ and $H_1/\lambda = 1/20$. The vorticity fields and pressure profiles for several more cylinder cuts and wave conditions can be found in Appendix A and B. Similar investigations performed by Kristiansen and Faltinsen (2017), showed a local pressure peak arising with time at the rear of the cylinder, subsequently spreading out. The peak build-up was associated with the formation of the local rear run-up. The same trends are observable in the presented pressure distribution in Figure 5.6. The $k-\omega$ SST model provides in general smoother pressure curves, and more visible formations of the peak, as it damps out many many of the disturbances due to the turbulence modelling.

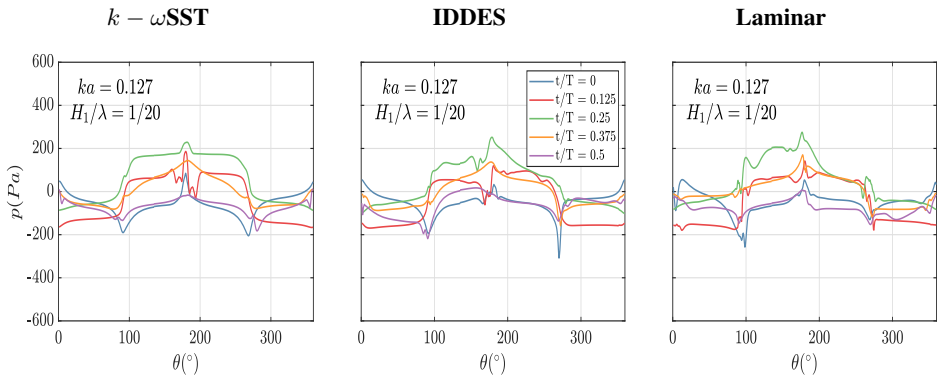

Figure 5.6: Pressure distribution on cylinder at five different time-instans, applying the $k-\omega$SST, IDDES, and laminar model. The top cut of the cylinder is considered, under wave conditions $ka = 0.127$ and wave steepness $H_1/\lambda = 1/20$. The respective time instants are taken within the seventh oscillation of in total eight oscillations.

5.2.3 Comparison of load harmonics

The integrated horizontal force was bandpass-filtered into the three first load harmonics, and compared between using the $k-\omega$ SST, IDDES, and the laminar model (see Figure 5.7). Considered wave condition was again $ka = 0.127$ and wave steepness $H_1/\lambda = 1/20$. As seen, the different approaches in modelling the boundary layer and vortex shedding, with the corresponding pressure distribution on the cylinder, does not make any considerable impact on the total horizontal force. All of the harmonics are, to a very large extent, complying both in terms of phase and amplitudes. There is only small differences to observe, e.g. the amplitudes of the load harmonics computed by the IDDES model are somewhat smaller than the corresponding amplitudes of the $k-\omega$ SST and laminar model. This may be, as earlier discussed, due to numerical dissipation when using the IDDES model, because of the non-optimal grid. However, the results indicate that neither treatment of the boundary layer as turbulent or laminar with the present 2-D numerical model, influence the total horizontal load on the cylinder under the considered wave conditions.

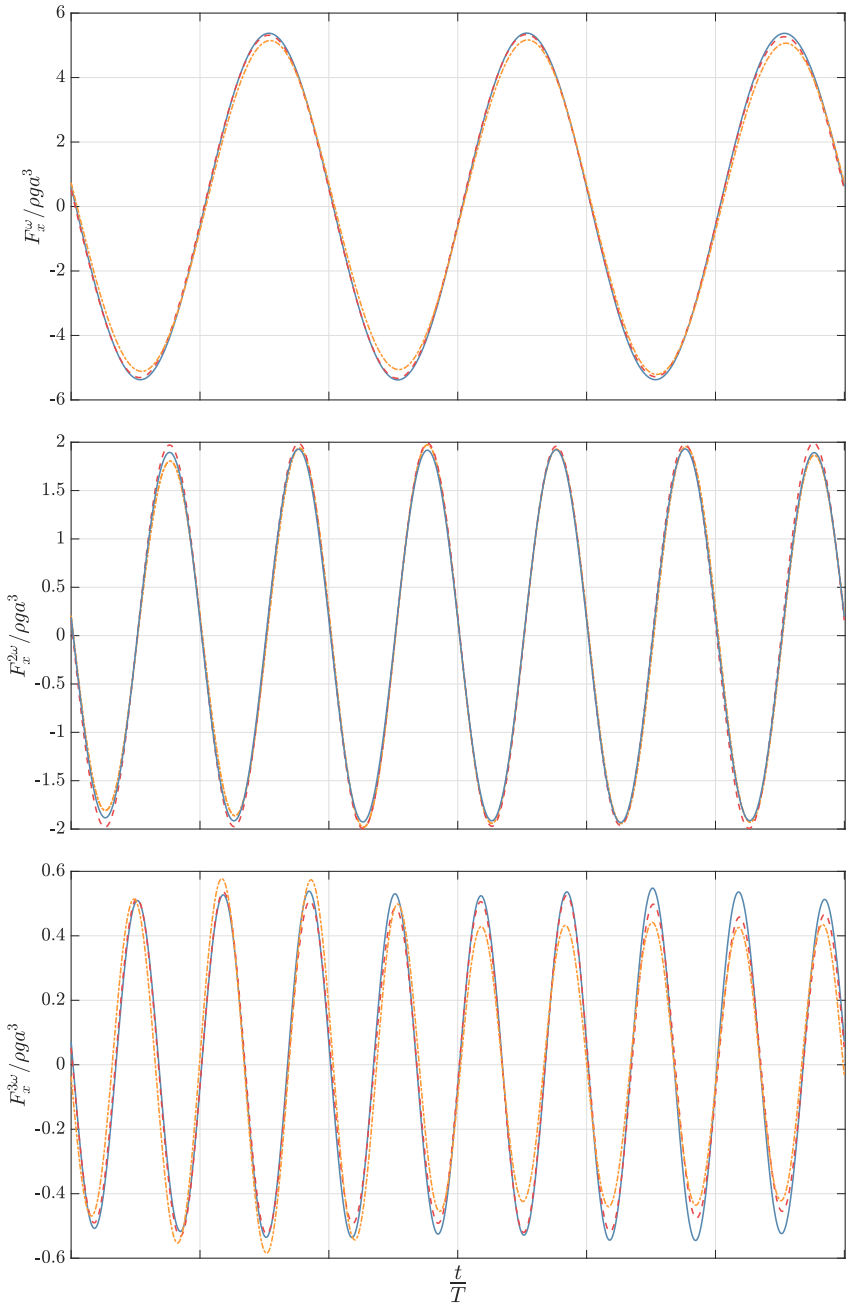

Figure 5.7: Comparison between the three first load harmonics of the force as evaluated by the combined CFD-FNV model, using: ——— , $k-\omega$ SST. -·-·- , IDDES; - - - - - , Laminar.

Chapter 6

Conclusion and further work

Strip theory based CFD-analyses have been performed for several wave conditions on a bottom mounted circular cylinder in order to evaluate the horizontal in-line force, also accounting for viscous effects. The terms from the inviscid FNV-theory, not included in the CFD-force, were added, composing a combined CFD-FNV load model. The 2-D numerical model obtained in Fluent was validated against experiments by Garrison et al. (1977), Bearman et al. (1985) and Sarpkaya (1987). The numerical results of C_M and C_D for varying KC and Re showed, for a sufficient range of KC, good agreement with the experiments. The limitations of the numerical model for higher KC were discussed in terms of the Courant number. The $k-\omega$ SST turbulence model was applied for the main analysis, which results were compared to experimental measurements obtained by Kristiansen and Faltinsen (2017) and from the present work. Special focus was on the ability of the combined load model to estimate the third harmonic loads of incoming, longer and steeper waves on the monopile, while these had been confirmed by Kristiansen and Faltinsen (2017) to be over-estimated by inviscid fifth order FNV theory generalized to finite water depth. The results showed that the third harmonic loads as estimated by the combined load model did not comply better with the experimental measurements. In fact, the third harmonic amplitudes were somewhat more over-estimated than when applying invscid FNV-theory. Hence, the introduction of a viscous force term could not explain the discrepancies. However, the combined load showed good agreement with both the experimental values and the inviscid FNV-theory, up to a wave steepness of approximately $1/40$.

Several approaches were tried out when modelling the boundary layer, in order to check if

this affected the results. A hybrid RANS/LES turbulence model was, as well as a laminar model, applied. The load harmonics were nearly not affected by the boundary layer treatment, although the vorticity field around the cylinder evidently depended on which of the three viscous models that were used. This could indicate that the neglection of 2-D flow separation not is the main cause for the discrepancies in the third harmonics between the FNV-theory and the experiments. However, to model the flow behaviour of an oscillating flow around a cylinder is considered as highly advanced. The critical Reynolds number is unknown, and the flow reattachment associated with critical flow regimes are considered as very complex to model numerically. Thus, such limitations in the numerical model could have affected the results.

Modelling or visualizing 3-D effects caused by flow separation, such as a local upwelling of the free surface at the rear of the cylinder, should be of main interest for further research. This phenomenon has been confirmed during several experiments(Kristiansen and Faltinsen (2017), Grue and Huseby (2002) and present work), and is believed to arise due to a high pressure zone at the rear of the cylinder because of vortex shedding. The high pressure zone was confirmed, plotting the pressure distribution on the cylinder during the numerical analysis. The rise of the free surface also affect the flow back, forming a two-way interaction. The attempt to colour a possible flow run-up rear of the cylinder during the experiment was not successful. Other approaches, such as PIV, could be a possibility in order to visualize the upwelling. However, PIV is associated with problems related to free surface because of reflections. Other effects, like 3-D wake and vertical varying incident flow, have neither been accounted for. Application of slender body theory, instead of strip theory, will include the latter effect.

Bibliography

Achenbach, E., 1971. Influence of surface roughness on the cross-flow around a circular cylinder. Journal of Fluid Mechanics, v46, part2.

ANSYS, 2009. ANSYS FLUENT 12.0 User's Guide. ANSYS, Inc.

Bachynski, E. E., Kristiansen, T., Thys, M., 2017. Experimental and numerical investigations of monopile ringing in irregular finite-depth water waves. Applied Ocean Research 68, 154 – 170.
URL http://www.sciencedirect.com/science/article/pii/S0141118716305284

Bearman, P., Chaplin, J., Graham, J., Kostense, J., Klopman, G., July 1985. The loading on a cylinder in post-critical flow beneath periodic and random waves.
URL https://eprints.soton.ac.uk/75417/

Cengel, Y. A., Cimbala, J. M., 2014. Fluid Mechanics. McGraw-Hill Education.

Chang, P. K., 1961. Separation of flow. Journal of the Franklin Institute 272 (6), 433 – 448.

Courant, R., Friedrichs, K., Lewy, H., 04 1928. On partial difference equations of mathematical physics(english translation). Math. Ann. 100, 32–74.

Dean, R., Dalrymple, R., 1991. Water Wave Mechanics for Engineers and Scientists. World Scientific Publishing.

Faltinsen, . M., Newman, J., Vinje, T., 1995. Nonlinear wave loads on a slender vertical cylinder. J. Fluid Mech.vol. 289, pp. 179-198.

Faltinsen, O. M., 1990. Sea Loads on ship and offshore structures. Cambridge University Press.

Faltinsen, O. M., Feb 1999. Ringing loads on a slender vertical cylinder of general cross-section. Journal of Engineering Mathematics 35 (1), 199–217.
URL https://doi.org/10.1023/A:1004362827262

Fenton, J., 1990. Nonlinear wave theories. The Sea 9.

Fenton, J. D., 1985. A fifth‐order stokes theory for steady waves. Journal of Waterway, Port, Coastal, and Ocean Engineering 111 (2), 216–234.

Ferziger, J., Peric, M., 2002. Computational Methods for Fluid Dynamics. 3rd Ed. Springer.

Fimland, D., 2018. Nonlinear wave loads on a vertical cylinder. Master thesis NTNU.

Fröhlich, J., von Terzi, D., 07 2008. Hybrid les/rans methods for the simulation of turbulent flows. Progress in Aerospace Sciences 44, 349–377.

Garrison, C., 03 1990. Drag and inertia forces on circular cylinders in harmonic flow. Journal of Waterway Port Coastal and Ocean Engineering-asce - J WATERW PORT COAST OC-ASCE 116.

Garrison, C., B. Field, J., D. May, M., 05 1977. Drag and inertia forces on a cylinder in periodic flow. J Waterw Port Coastal Ocean Div Proc ASCE 103, 193–204.

Garrison, C. J., 1980. A review of drag and inertia forces on circular cylinders. In: Offshore Technology Conference.

Gritskevich, M., Garbaruk, A., Schtze, J., Menter, F., 04 2012. Development of ddes and iddes formulations for the k- shear stress transport model. Flow, Turbulence and Combustion 88.

Grue, J., Huseby, M., 2002. Higher-harmonic wave forces and ringing of vertical cylinders. Applied Ocean Research 24 (4), 203 – 214.

Hedges, T., 01 1995. Regions of validity of analytical wave theories. Proceedings of The Ice - Water Maritime and Energy 112, 111–114.

Honji, H., 1981. Streaked flow around an oscillating circular cylinder. Journal of Fluid Mechanics 107, 509520.

Hudspeth, R. T., Nath, J. H., 1985. High reynolds number wave force investigation in a wave flume. Report No. CR85.004, Naval Civ. Engrg. Lab., 116.

Keulegan, G., Carpenter, L., 1958. Forces on cylinders and plates in an oscillating fluid. Journal of Research of the National Bureau of Standards 60.

Kristiansen, T., Faltinsen, O., 2017. Higher harmonic wave loads on vertical cylinder in finite water depth. Cambridge University Press 833, 773–805.

Malenica, ., Molin, B., 1995. Third-harmonic wave diffraction by a vertical cylinder. Journal of Fluid Mechanics 302, 203229.

Menter, F., 1994. Two-equation eddy-viscosity turbulence models for engineering applications. AIAA Journal 32 (8), 1598–1605.

Morison, J. R., J. J. W. . S. S. A., 1950. The force exerted by surface waves on piles. In: Society of Petroleum Engineers.

Pang, A., Skote, M., Lim, S., 2016. Modeling high re flow around a 2d cylindrical bluff body using the k- (sst) turbulence model. Progress in Computational Fluid Dynamics 16 (1), 1–34.

Paulsen, B. T., 2014. Forcing of a bottom-mounted circular cylinder by steep regualar water waves at finite water depth. Cambridge University Press 755, 1–34.

Pettersen, B., 2007. Marin Teknikk 3 - Hydrodynamikk. Department of Marin Technology, NTNU.

Prandtl, L., 1904. Uber flussigkeitsbewegungen bei sehr kleiner reibung. In: Verhandlungen des III. Internationalen Mathematiker Kongresses. Vol. 88. Heidelberg, Germany, p. pp. 484491.

Remy, T., Mbistrova, A., 2018. Key trends and statistics 2017. Offshore wind in Europe.

Rodenbusch, G., Gutierrez, C., 1983. Forces on cylinders in two-dimensional flows.

Sarpkaya, T., 1976a. Vortex shedding and resistance in harmonic flow about smooth and rough circular. In: proceesding of the Conference on The Behaviour of Offshore Structures. Trondheim, Norway, p. pp. 220235.

Sarpkaya, T., 1976b. Vortex shedding and resistance in harmonic flow about smooth and rough circular at high reynolds numbers. Naval Postgraduate School Tech. Report No. NPS-59SL76021.

Sarpkaya, T., 1986. Force on a circular cylinder in viscous oscillatory flow at low keule-gancarpenter numbers. Journal of Fluid Mechanics 165, 6171.

Sarpkaya, T., 11 1987. Oscillating flow about smooth and rough cylinders. Journal of Offshore Mechanics and Arctic Engineering 109, 307.

Sarpkaya, T., 2006. Structures of separation on a circular cylinder in periodic flow. Journal of Fluid Mechanics 567, 281297.

Sarpkaya, T., Isaacson, M., 1981. Mechanics of Wave Forces on Offshore Structures. Van Nostrand Reinhold Company.

Shur, M. L., Spalart, P. R., , Strelets, M. K., Travin, A. K., 2008. A hybrid rans-les approach with delayed-des and wall-modelled les capabilities. International Journal of Heat and Fluid Flow, 20, 181–195.

Skjelbreia, L., Hendrickson, J., 1960. Fifth order gravity wave theory. Coastal Engineering Proceedings 1 (7), 10.
URL https://icce-ojs-tamu.tdl.org/icce/index.php/icce/article/view/2169

Spalart, P., Deck, S., Shur, M., Squires, K., Strelets, M., Travin, A., 7 2006. A new version of detached-eddy simulation, resistant to ambiguous grid densities. Theoretical and Computational Fluid Dynamics 20 (3), 181–195.

Spalart, P. R., Jou, W.-H., Strelets, M., Allmaras, S. R., 1997. Comments on the feasibility of les for wings, and on a hybrid rans/les approach. In: International conference; 1st, Advances in DNS/LES: Direct numerical simulation and large eddy simulation. Ruston, LA.

Spalart, P. R., Jou, W.-H., Strelets, M., Allmaras, S. R., 2003. Ten years of industrial experience with the sst turbulence model. In: 4th:; Internal Symposium, Turbulence, heat and mass transfer; 2003; Antalya, Turkey. New York, Wallingford.

Sumer, B. M., Fredse, J., 2006. Hydrodynamics Around Cylindrical Structures, revised Edition. WORLD SCIENTIFIC.
URL https://www.worldscientific.com/doi/abs/10.1142/6248

Ursell, F., 1953. The long-wave paradox in the theory of gravity waves. Mathematical Proceedings of the Cambridge Philosophical Society 49 (4), 685694.

Ursell, F., 1963. The decay of the free motion of a flaoting body. Journal of Fluid Mechanics 2, 305–319.

Wang, C.-Y., 1968. On high-frequency oscillatory viscous flows. Journal of Fluid Mechanics 32 (1), 5568.

White, F. M., 2006. Viscous Fluid Flow. McGraw-Hill Education.

Appendix

Appendix A: Visualization of vorticity

$k-\omega$SST

$ka = 0.127 \;\; H_1/\lambda = 1/20$

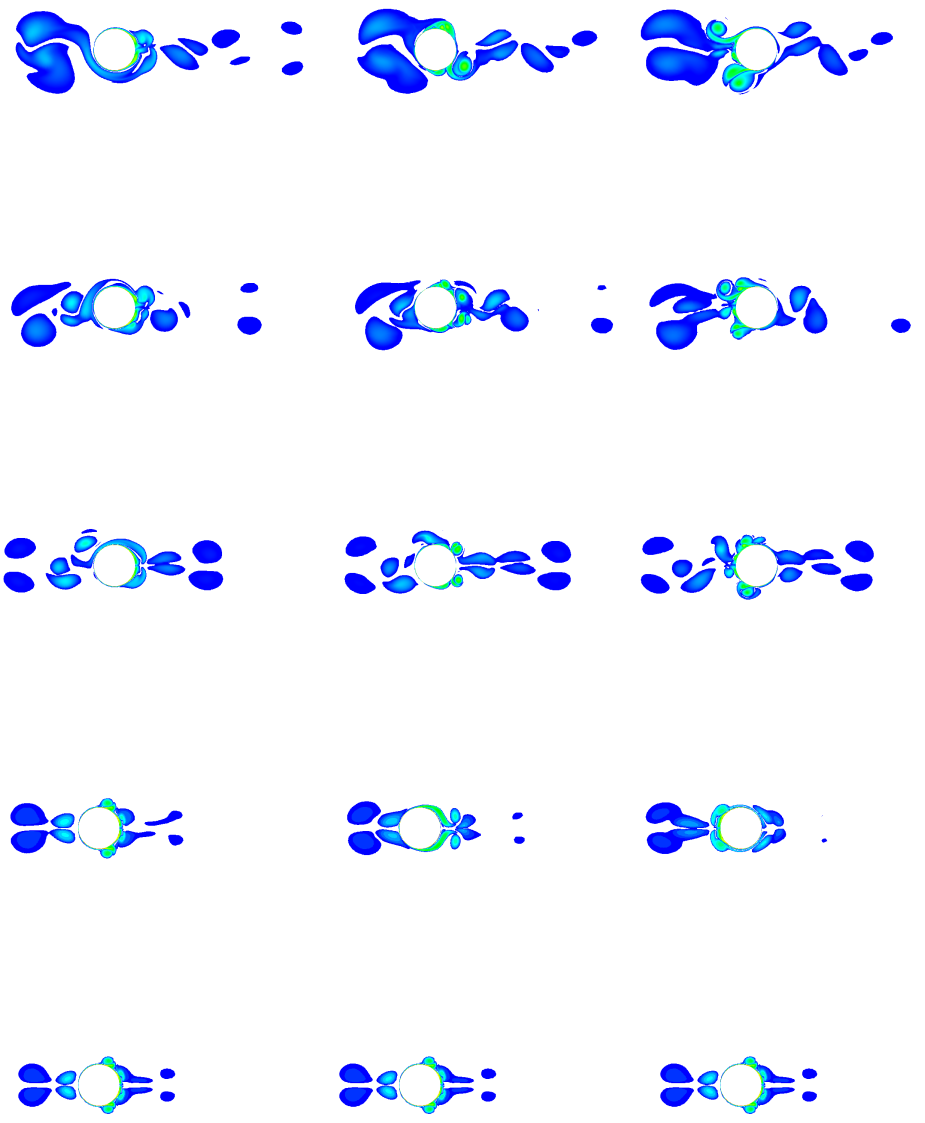

t=0 **t=T/4** **t=T/2**

The vorticity field around the cylinder for $ka = 0.127$, $H_1/\lambda = 1/20$, at three time-instants: $t = 0$, $t = T/4$ and $t = T/2$. The plots are obtained during the seventh oscillation(eight in total). Cut numbering from bottom to top: 1, 5, 10, 15, 20, of in total 20 cuts. $k-\omega$SST model used.

$ka = 0.127 \;\; H_1/\lambda = 1/25$

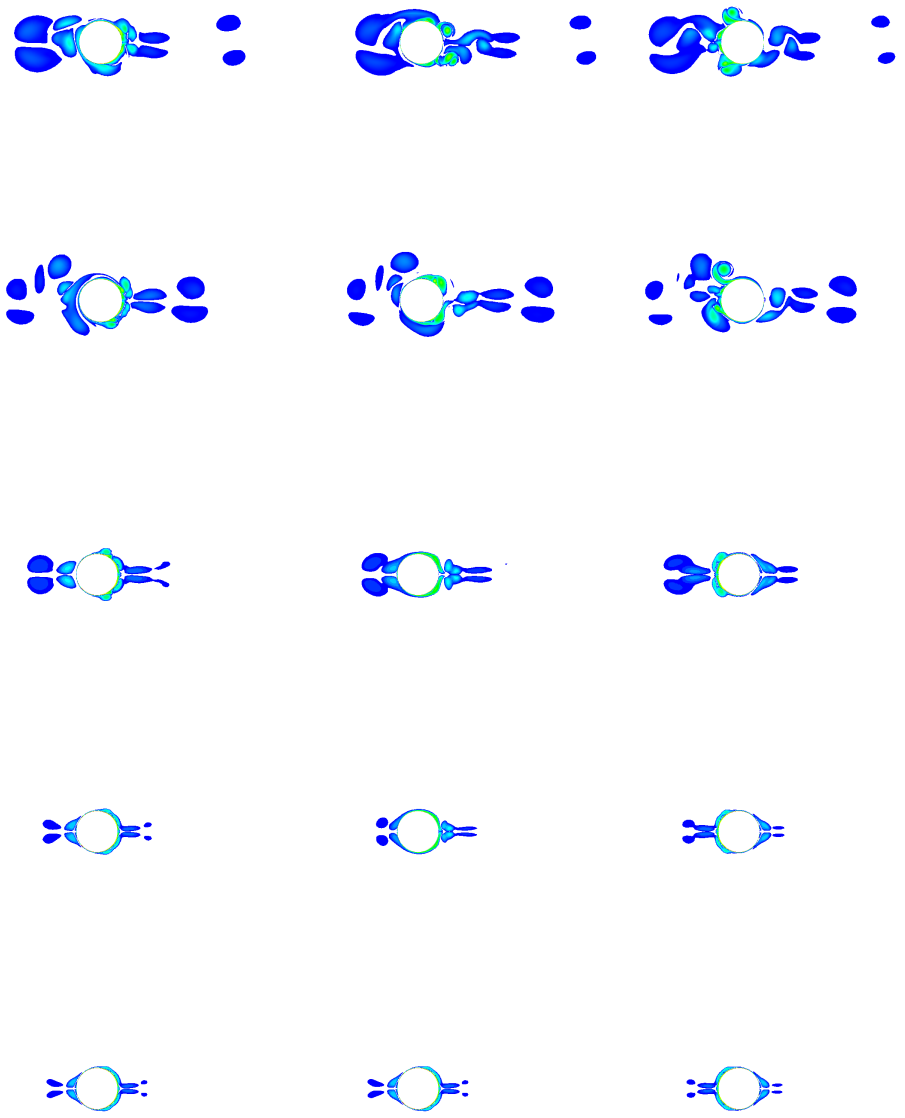

t=0 **t=T/4** **t=T/2**

The vorticity field around the cylinder for $ka = 0.127$, $H_1/\lambda = 1/25$, at three time-instants: $t = 0$, $t = T/4$ and $t = T/2$. The plots are obtained during the seventh oscillation(eight in total). Cut numbering from bottom to top: 1, 5, 10, 15, 20, of in total 20 cuts. $k - \omega$SST model used.

$ka = 0.127 \;\; H_1/\lambda = 1/30$

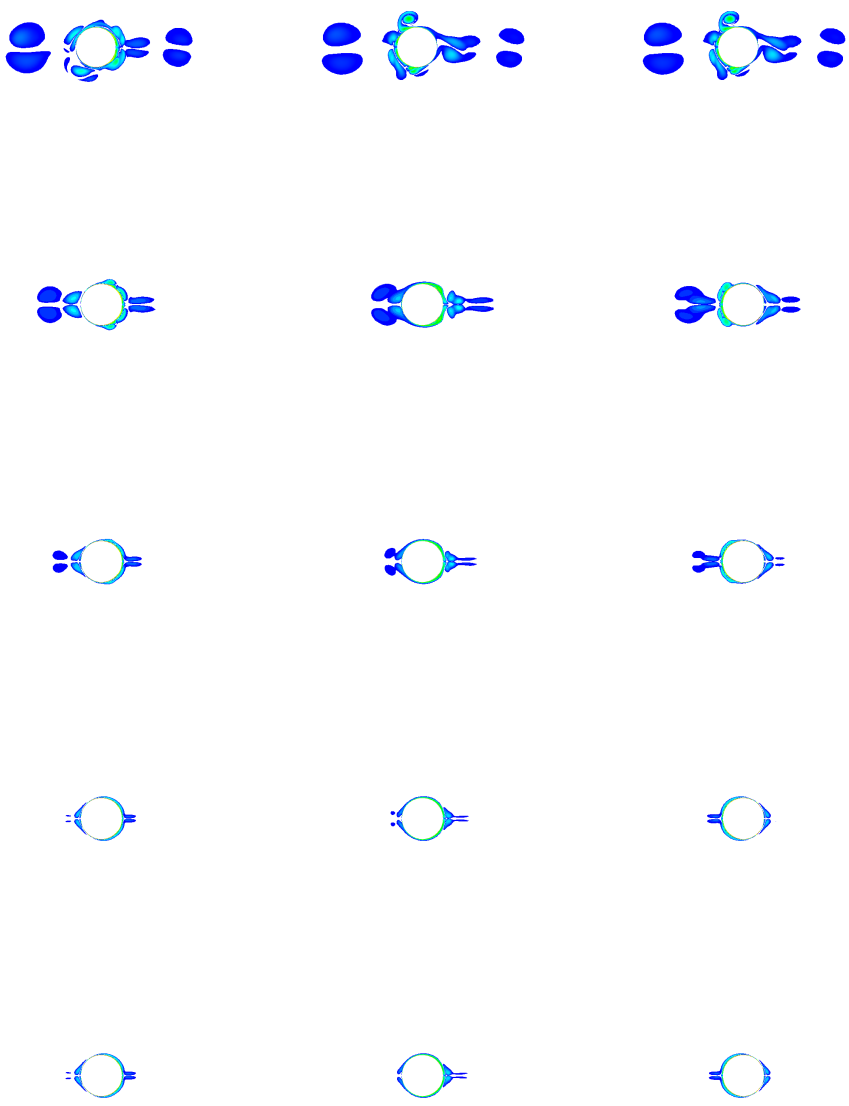

t=0 **t=T/4** **t=T/2**

The vorticity field around the cylinder for $ka = 0.127$, $H_1/\lambda = 1/30$, at three time-instants: $t = 0$, $t = T/4$ and $t = T/2$. The plots are obtained during the seventh oscillation(eight in total). Cut numbering from bottom to top: 1, 5, 10, 15, 20, of in total 20 cuts. $k - \omega$SST model used.

$ka = 0.127 \;\; H_1/\lambda = 1/40$

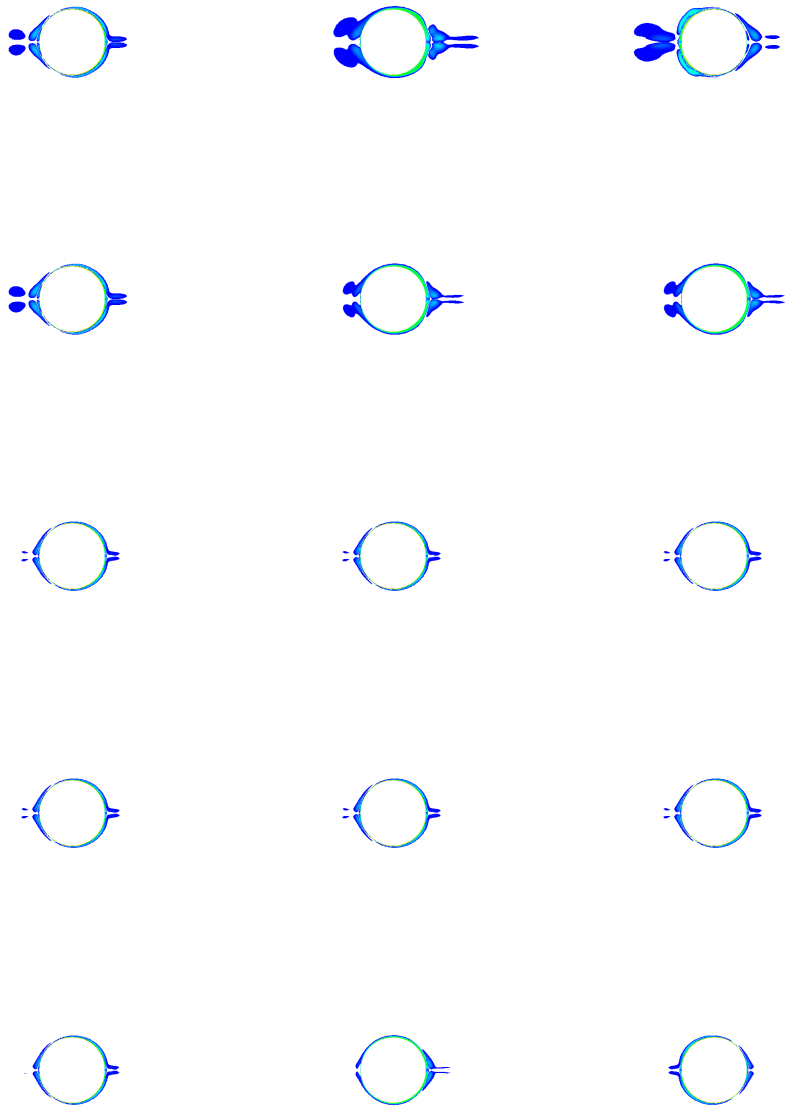

t=0 **t=T/4** **t=T/2**

The vorticity field around the cylinder for $ka = 0.127$, $H_1/\lambda = 1/40$, at three time-instants: $t = 0$, $t = T/4$ and $t = T/2$. The plots are obtained during the seventh oscillation(eight in total). Cut numbering from bottom to top: 1, 5, 10, 15, 20, of in total 20 cuts. $k - \omega$SST model used.

$ka = 0.105 \;\; H_1/\lambda = 1/20$

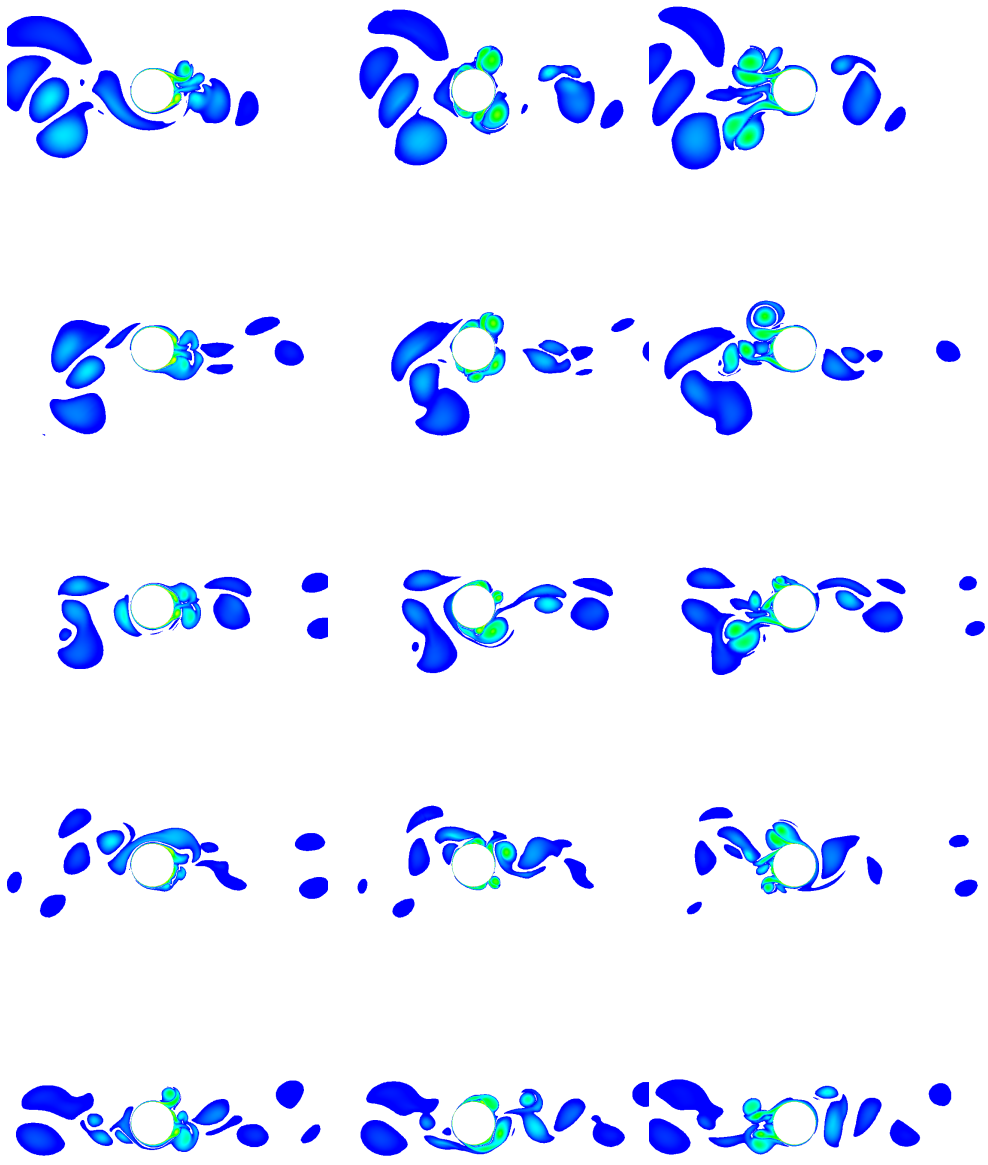

t=0 **t=T/4** **t=T/2**

The vorticity field around the cylinder for $ka = 0.105$, $H_1/\lambda = 1/20$, at three time-instants: $t = 0$, $t = T/4$ and $t = T/2$. The plots are obtained during the seventh oscillation(eight in total). Cut numbering from bottom to top: 1, 5, 10, 15, 20, of in total 20 cuts. $k - \omega$SST model used.

IDDES

$ka = 0.127 \;\; H_1/\lambda = 1/20$

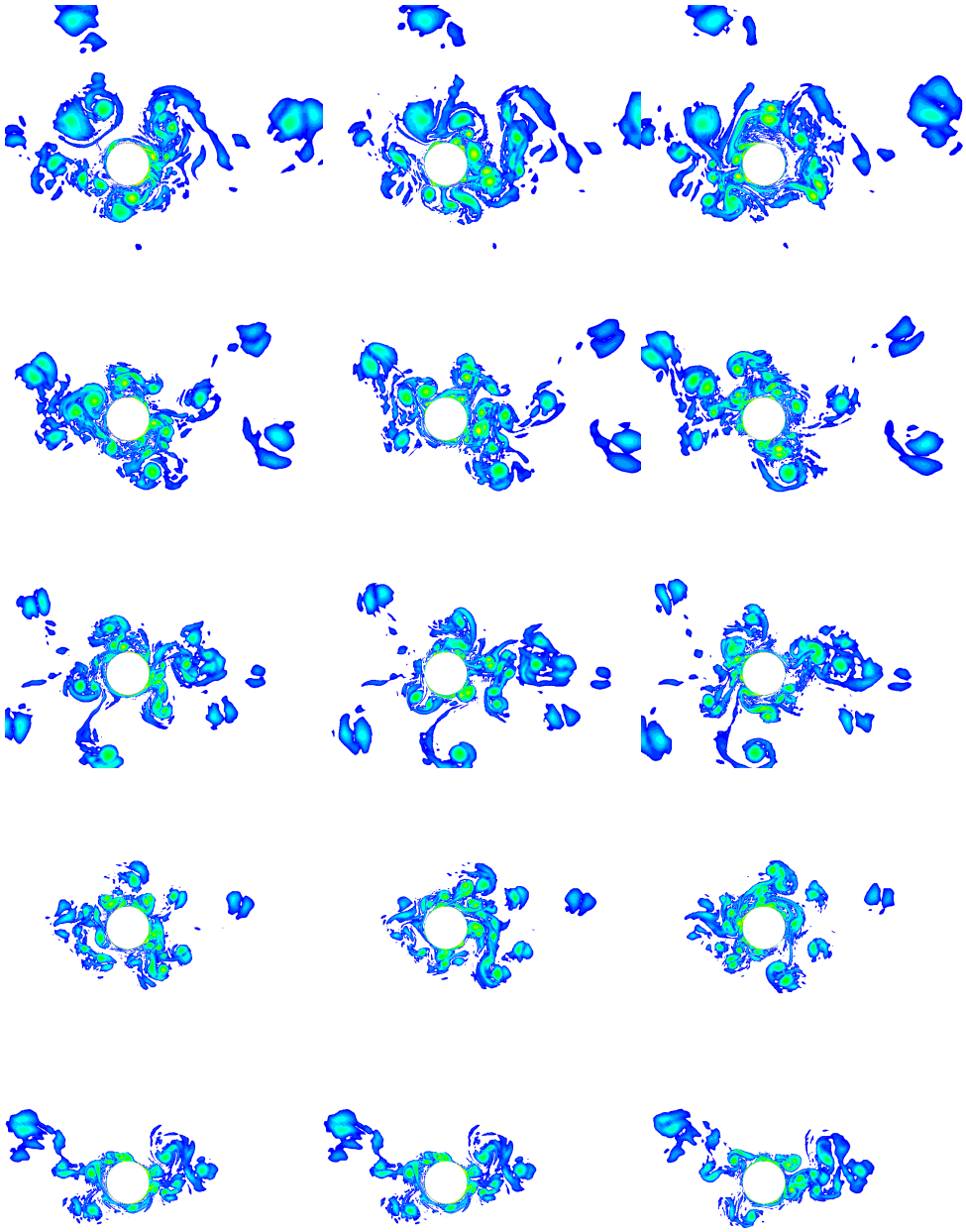

t=0 **t=T/4** **t=T/2**

The vorticity field around the cylinder for $ka = 0.127$, $H_1/\lambda = 1/20$, at three time-instants: $t = 0$, $t = T/4$ and $t = T/2$. The plots are obtained during the seventh oscillation(eight in total). Cut numbering from bottom to top: 1, 5, 10, 15, 20, of in total 20 cuts. IDDES model used.

$ka = 0.127 \;\; H_1/\lambda = 1/25$

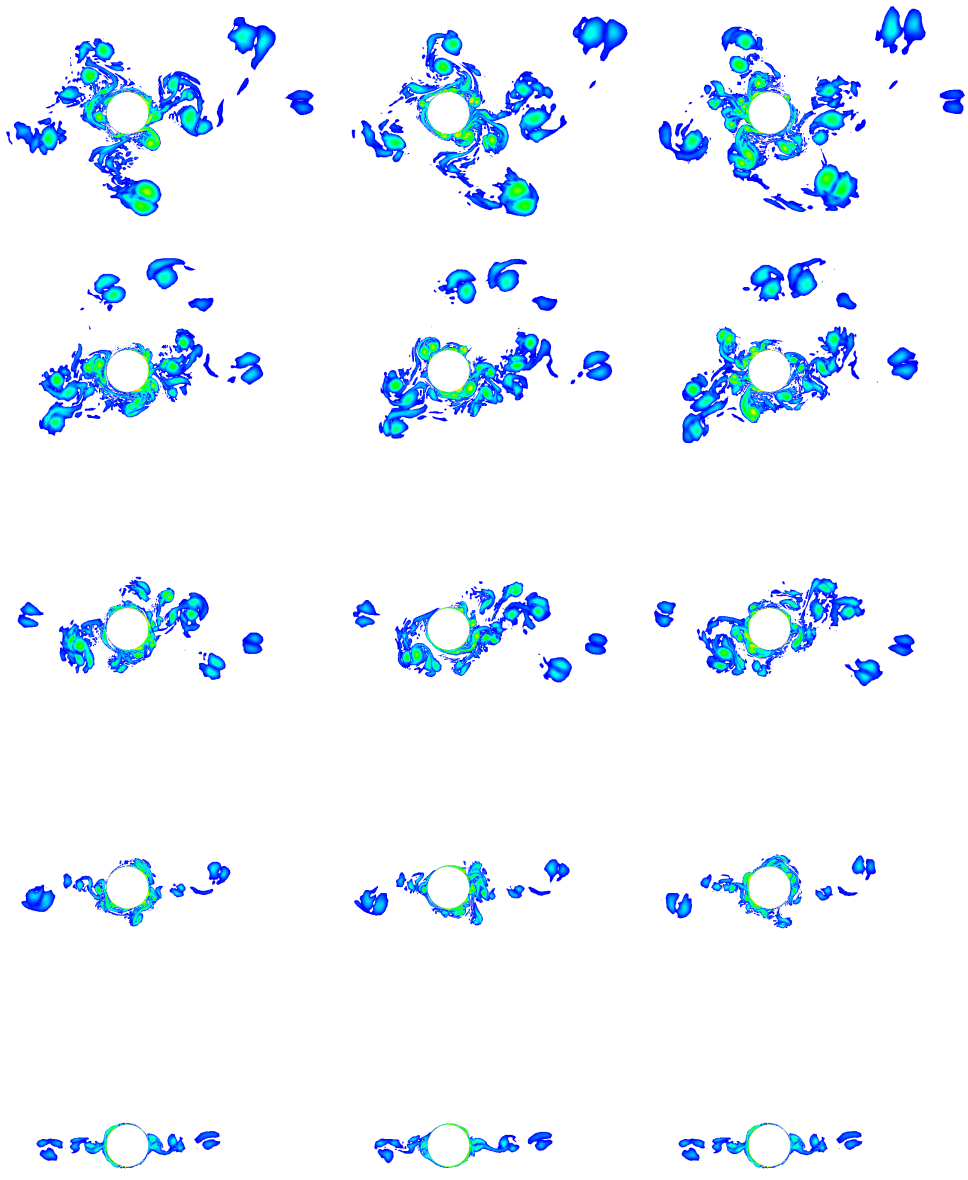

t=0 **t=T/4** **t=T/2**

The vorticity field around the cylinder for $ka = 0.127$, $H_1/\lambda = 1/25$, at three time-instants: $t = 0$, $t = T/4$ and $t = T/2$. The plots are obtained during the seventh oscillation(eight in total). Cut numbering from bottom to top: 1, 5, 10, 15, 20, of in total 20 cuts. IDDES model used.

Laminar

$ka = 0.127 \;\; H_1/\lambda = 1/20$

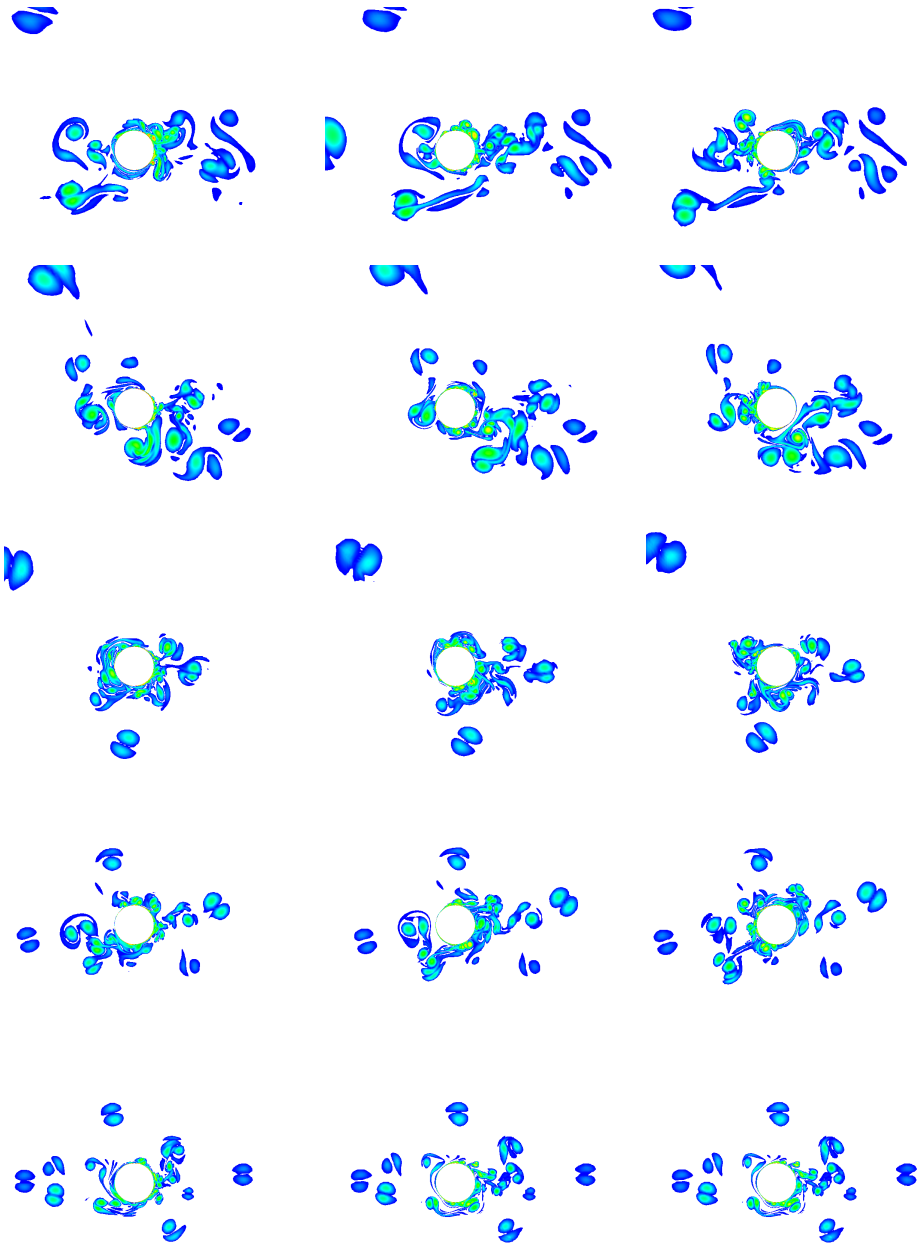

t=0 **t=T/4** **t=T/2**

The vorticity field around the cylinder for $ka = 0.127$, $H_1/\lambda = 1/20$, at three time-instants: $t = 0$, $t = T/4$ and $t = T/2$. The plots are obtained during the seventh oscilliation. Cut numbering from bottom to top: 1, 5, 10, 15, 20, of in total 20 cuts. Laminar model used.

Appendix B:Pressure distribution on cylinder

$k-\omega$ SST

$ka = 0.127$

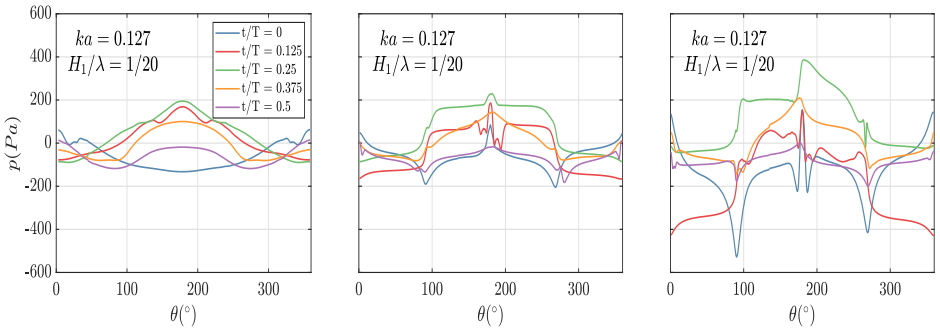

Cut 1 **Cut 10** **Cut 20**

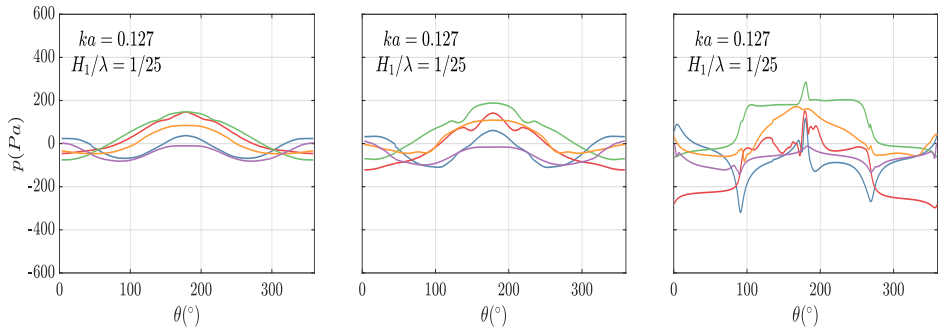

Cut 1 **Cut 10** **Cut 20**

Pressure distribution on cylinder at five time-instants shown for cut 1, 10 and 20 of in total 20 cuts. θ is defined as zero at the stagnation point of the cylinder. The seventh of in total eight oscillations is used.$k-\omega$SST model used.

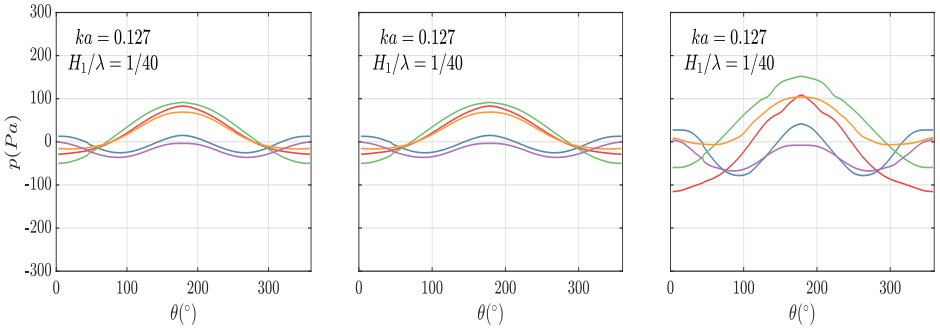

$ka = 0.105$

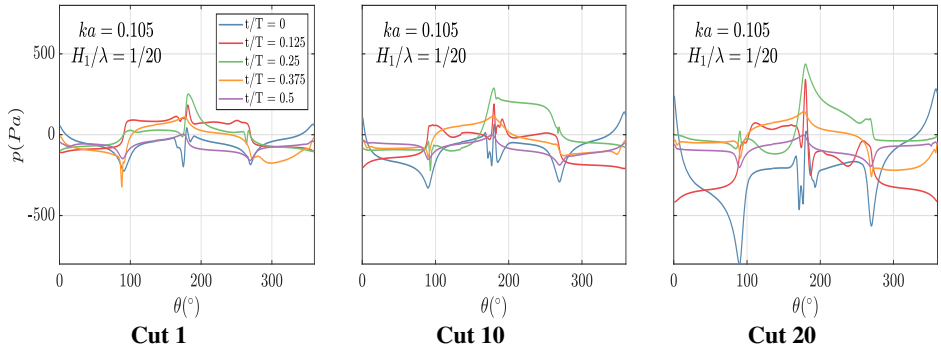

Pressure distribution on cylinder at five time-instants shown for cut 1, 10 and 20 of in total 20 cuts. θ is defined as zero at the stagnation point of the cylinder.The seventh of in total eight oscillations is used.$k-\omega$SST model used.

IDDES

$ka = 0.127$

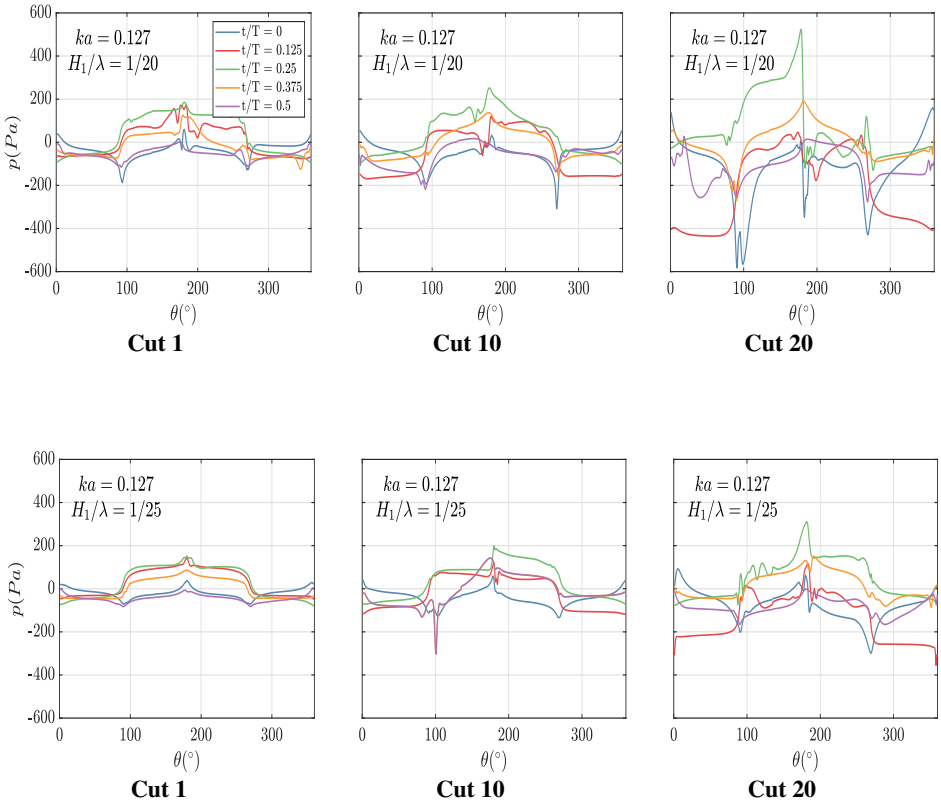

Pressure distribution on cylinder at five time-instants shown for cut 1, 10 and 20 of in total 20 cuts. θ is defined as zero at the stagnation point of the cylinder. IDDES model used.

Laminar

$ka = 0.127$

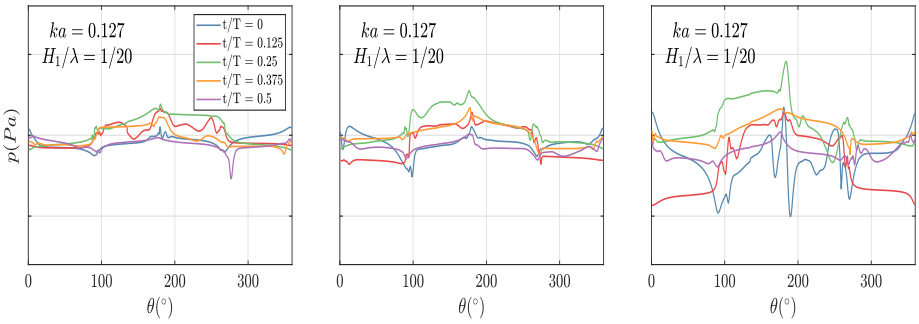

Cut 1 **Cut 10** **Cut 20**

Torstein Sæter

Ringing Loads on Offshore Wind Turbine Monopiles

NTNU
Norwegian University of
Science and Technology